POLITECNICO DI MILANO

Master of Science in Mechanical Engineering

MOTION BLUR COMPENSATION TO IMPROVE THE ACCURACY OF DIGITAL IMAGE CORRELATION MEASUREMENTS

Relatore: Prof. Emanuele Zappa

Tesi di laurea di:

Simone Turrisi

Matr. 853822

Anno accademico 2016/2017

“Let your joy be in your journey, not in some distant goal”

Tim Cook

Contents

Ringraziamenti

La tesi che andrete a leggere rappresenta il risultato di un lungo lavoro, iniziato in data 24 marzo 2017. È stato un periodo molto intenso, durante il quale non sono mai mancate nuove sfide e difficoltà, ma anche grosse soddisfazioni. Al tempo stesso è stato un momento di forte accrescimento sia dal punto di vista professionale che personale, e che per questo difficilmente dimenticherò.

Giunto alla conclusione di questo lavoro, un primo ringraziamento va sicuramente al professor Emanuele Zappa, per l'aiuto sempre puntuale ed attento che ha saputo darmi, per la competenza con cui ha saputo indirizzarmi nelle occasioni di dubbio e per la passione verso il mondo della ricerca che ha saputo trasmettermi.

Ringrazio anche Alberto e Nicola, per aver collaborato con me durante tutta l'attività sperimentale, e il gruppo di ricerca di Misure e Tecniche Sperimentali del Politecnico di Milano, per l'efficiente supporto logistico e personale.

Un ringraziamento di cuore va a tutta la mia famiglia, a cui dedico questo lavoro, per il continuo impegno mostrato nel crescermi e nel formarmi, e per essere stata sempre al mio fianco, non facendomi mai mancare sia il sostegno morale che quello economico.

Un grosso grazie anche ai miei amici Gio, Mare, Rava, Dona, Bolo, Azza, Batti, Cina, Geki e Cire, che, attraverso parole, gesti, messaggi e risate hanno sempre trovato l'occasione per sostenermi ed incoraggiarmi.

Un ultimo ringraziamento va infine a me stesso, per aver raggiunto il traguardo in cui ho fortemente creduto con dedizione e sacrificio. Esso rappresenta un punto di arrivo, ma al tempo stesso l'inizio di una nuova avventura, che sarò pronto ad affrontare con lo stesso impegno e con la stessa determinazione.

.

Abstract

Vision-based measurements represent a wide variety of contactless methods able to extract data from an image-recorded scene using digital cameras. During the last decade, the development of more performing devices at diminishing costs makes the vision systems an attractive and valuable solution in many areas of science and engineering. The reasons of this success are to be found in the easiness of the setup, in the possibility of providing contactless monitoring and of reconstructing full-field displacements and strains.

Digital Image Correlation (DIC) is one of the most diffused optical techniques to track motions and deformations when vision-based measurements are employed. Although the majority of uses and studies involving DIC were focused on static conditions, the technological improvements of the recent years have enabled the extension of the DIC method also to the dynamic field. In such a context, motion blur represents a relevant problem, since it is an important source of uncertainty for DIC measurements. To solve this issue, referenced deconvolution method has been proposed and tested. The documented attempts, although successful, showed little robustness.

Continuing on this topic, the thesis proposes an innovative approach to mitigate the effect of motion blur on 2D Digital Image Correlation. The research work is introduced by the state of the art of DIC technique, giving particular emphasis on setup characteristics and algorithm implementation. Then, the impact of motion blur on DIC measurements and motion effect simulation techniques are investigated relying on the available literature information. In the following section, a review of the main types of image deconvolution methods is proposed, useful either to estimate or to remove the motion effect from a given image. Furthermore, the theory of cepstral analysis is presented as a valid option for image deconvolution processes.

Once the necessary theoretical background has been introduced, the further step is to try to compensate the undesired blur effect on DIC measurements. Firstly, a theoretical model for motion blur estimation based on cepstral analysis is proposed and validated. Secondly, the problem of image restoration is tackled, where two image deconvolution methods are presented: one based on cepstrum deconvolution and the other based on Wiener filter. The latter is suggested in presence of noise. Eventually, each mentioned technique is tested with synthetic DIC experiments, involving numerically generated images, in order to demonstrate

whether the compensation algorithms are able to improve the accuracy of DIC measurements in presence of motion blur.
The last part of the study, instead, aims to experimentally validate the previously presented techniques with a realistic dynamic application. Therefore, a harmonic test is conducted, imposing the sinusoidal motion law on a cantilever beam able to produce different blurring conditions on the images grabbed by the camera. Both the motion blur estimation and removal processes are applied and finally the DIC performance, in terms of uncertainty reduction after blur compensation, are analysed.

Key words: **vision systems; vibration measurements; Digital Image Correlation (DIC); dynamics; motion blur; uncertainty; cepstral analysis; image deblurring; image deconvolution; Wiener filter.**

Sommario

La tecnologia basata sui sistemi di visione include un'ampia gamma di dispositivi in grado di fornire misurazioni partendo dall'analisi di immagini acquisite da una telecamera digitale. Il miglioramento prestazionale delle telecamere, unito ad un abbassamento del costo delle stesse, ha stimolato la diffusione dei sistemi di visione nell'ultimo decennio, facendone una soluzione vantaggiosa sia in applicazioni di tipo scientifico che ingegneristico. Tale tipo di tecnologia può offrire diversi vantaggi in campo sperimentale, tra cui la semplicità nella preparazione del setup, la possibilità di effettuare un monitoraggio senza contatto e di ricostruire mappe di spostamento e di deformazione.

Gran parte degli attuali sistemi di visione ricorre alla tecnica denominata Digital Image Correlation (DIC) per processare immagini ed ottenere stime su spostamenti e deformazioni. Sebbene la quasi totalità degli utilizzi dell'algoritmo DIC sia finalizzata ad applicazioni di tipo statico, il continuo miglioramento tecnologico degli ultimi anni ha reso possibile l'estensione anche in campo dinamico, per esempio nell'analisi di misure di corpi vibranti. In un simile contesto, il moto relativo tra telecamera e misurando durante tempo di esposizione diventa rilevante, poiché contribuisce alla generazione dell'effetto mosso. Quest'ultimo è in grado di produrre una degradazione delle informazioni metrologiche contenute nell'immagine, aumentando di conseguenza l'incertezza di misura ottenuta tramite metodo DIC. Per risolvere tale problema, sono state sviluppate alcune tecniche di deconvoluzione che permettono di rimuovere l'effetto mosso durante la fase di image-processing.

Il principale obiettivo della tesi è quello di continuare lungo questa direzione, proponendo un approccio innovativo che possa contenere l'aumento dell'incertezza di misura causato dall'effetto mosso. La prima parte del lavoro di ricerca si occupa della descrizione della tecnica Digital Image Correlation, dedicando particolare attenzione alla preparazione del setup di misura e all'implementazione dell'algoritmo. Successivamente viene introdotto un modello analitico capace di descrivere la natura fisica dell'effetto mosso, seguito dal relativo impatto sulle misurazioni di tipo DIC, facendo riferimento ad informazioni provenienti dalla letteratura. Nella sezione seguente vengono descritte, invece, le principali tipologie di deconvoluzione per immagini, adottabili sia per la stima che per la rimozione di processi di degradazione, quali l'effetto mosso. Tra queste, l'analisi cepstrale rappresenta un'ottima opportunità.

Una volta introdotti i necessari accorgimenti teorici, il passo successivo prevede l'implementazione di una procedura che possa effettivamente migliorare le performance delle misurazioni ottenute tramite DIC in presenza di effetto mosso. Per prima cosa, viene proposto un algoritmo in grado di stimare l'entità dell'effetto mosso partendo da un'analisi di tipo cepstrale. Dopo di che si passa a considerare il processo di restauro vero e proprio dell'immagine degradata da effetto mosso. A tale proposito, vengono presentate due tipologie di compensazione, una basata sulla deconvoluzione in dominio cepstrum e l'altra sulla deconvoluzione con filtro di Wiener. Ciascuna tecnica viene poi testata su esperimenti di tipo sintetico, ossia su immagini in cui l'effetto mosso è stato generato numericamente. L'obbiettivo è quello di verificare che entrambi gli algoritmi di compensazione siano in grado di migliorare l'accuratezza delle misurazioni con Digital Image Correlation.
La parte finale di questo studio viene dedicata alla validazione sperimentale delle tecniche appena descritte. Al fine di simulare una possibile applicazione in campo dinamico, viene utilizzato uno shaker per imporre al target (in questo caso una trave incastrata) una legge di moto di tipo sinusoidale, generando così nelle immagini acquisite dalla telecamera diverse condizioni di effetto mosso. Esse costituiscono un ottimo banco di prova per l'applicazione degli algoritmi di stima e rimozione dell'effetto mosso. Anche in questo caso l'intera procedura è finalizzata alla riduzione dell'incertezza di misura stimata tramite metodo DIC dopo la rimozione dell'effetto mosso.

<u>Parole chiave:</u> sistemi di visione; misura di vibrazioni; Digital Image Correlation (DIC); dinamica; effetto mosso; incertezza di misura; analisi cepstrale; deblurring; deconvoluzione di immagini; filtro di Wiener.

List of figures

List of tables

CHAPTER 1
DIGITAL IMAGE CORRELATION AND MOTION BLUR

1.1 Full-field measurements and Digital Image Correlation

The measurement of surface deformation and displacement of materials or structures subjected to various loading conditions (e.g. mechanical loading or thermal loading) is one of the fundamental task of experimental mechanics. Traditional strain gauges are by far the most exploited technique when local measurements are required. Instead, in case of full-field measurements, vision based techniques have been developed and applied, including both interferometric techniques (such as holography interferometry, speckle interferometry, moiré interferometry [1]) and non-interferometric techniques (such as the grid method [2], [3] and digital image correlation (DIC)).

In the firsts, the measurement surface, usually characterized by uniform white texture, is lighted by means of structured light (using lasers or fringe projectors). The measure is obtained processing the phase difference of the scattered light wave from the test object surface before and after the loading, by means of fringe processing and phase analysis.

Non-interferometric techniques, instead, determine the surface deformation by comparing the gray intensity changes of the object surface before and after deformation, and generally have less severe requirements under experimental conditions.

As a representative non-interferometric optical technique, the DIC method has been widely accepted and adopted in solid mechanics, because of its good capability and flexibility to

measure surface deformations. It directly provides full-field displacements and strains by comparing the digital images of the specimen surface in the un-deformed (or reference) and deformed states respectively.
The technique, originally developed by a group of researchers at the University of South Carolina in the 80's [4]-[9], is known in literature with different names, such as digital speckle correlation [10], [11], texture correlation [12], computer aided speckle interferometry [13], [14] and electronic speckle photography [15]-[18]. During the past few years, the DIC method has been extensively investigated and significantly improved for reducing computation complexity, achieving high accuracy of measurement and expanding the application range. For example, the two-dimensional (2D) DIC method using a single fixed camera is limited to in-plane deformation measurement of the planar object surface. To obtain reliable measurements, some requirements on the measuring system must be met [8], [9]. If the test object is of a curved surface, or three-dimensional (3D) deformation occurs during loading, the 2D DIC method is no longer applicable. To overcome this disadvantage, 3D DIC based on the principle of binocular stereovision [19], [20] was developed.

The current thesis is only focused on the 2D DIC method for in-plane displacement measurement. It should be noted at first that both laser speckle patterns [17], [21] and artificial white-light speckle patterns (or more accurately, the random gray intensity pattern of the object surface) have been used as the carrier of surface deformation information in 2D DIC. The laser speckle pattern can be produced by illuminating the optically rough surface with a coherent light source (laser beam). However, a serious decorrelation effect occurs when the test object is subjected to rigid body motion, as well as excessive straining and out-of-plane displacement [22], which prevents its practicality. In contrast, the white-light speckle is more robust and appealing. Indeed, it can easily be found that most of the current publications regarding DIC employ white-light speckle patterns, which used a white light source or natural light illumination.
Compared to the interferometric optical techniques used for in-plane deformation measurement, the 2D DIC method has both advantages and disadvantages. For instance, it offers the following attractive advantages:

- Simple experimental setup and specimen preparation: only one fixed camera is needed to record the digital images of the tested specimen surface before and after deformation. Specimen preparation is unnecessary if the natural texture of a specimen surface has a random gray intensity distribution, or can simply be made by spraying paints onto the specimen surface.

- Low requirements in measurement environment: 2D-DIC does not require a laser source. A white light source or natural light can be used for illumination during loading. Thus, it is suitable for both laboratory and field applications.
- Wide range of measurement sensitivity and resolution: since the 2D DIC method deals with digital images, thus the digital images recorded by various high spatial-resolution digital image acquisition devices can be directly processed by the 2D DIC method. This allows 2D DIC to be coupled with optical microscopy or scanning electron microscopy (SEM), to realize microscale to nanoscale deformation measurement. Similarly, the instantaneous deformation measurement can be realized by analysing the dynamic sequence of digital images recorded with high-speed cameras using the 2D DIC method [23]-[24].

Therefore, it can be said that the 2D DIC method is one of the current most active optical measurement technologies, and demonstrates increasingly broad application prospects.
Nevertheless, the 2D DIC method also suffers some disadvantages:

- the test planar object surface must have a random gray intensity distribution;
- the measurements depend heavily on the quality of the imaging system;
- at present, the strain measurement accuracy of the 2D DIC method is lower than the one of interferometric techniques, and is not recommended as an effective tool for non-homogeneous small deformation measurement.

1.2 Two-dimensional DIC

The standard implementation of a two-dimensional digital image correlation measurement system is basically composed by three steps:

1. Specimen surface and measurement setup preparation
2. Image acquisition of the specimen before (reference) and after loading
3. Digital image processing to estimate displacements and strains induced during loding

In the following, a general framework about the required setup characteristics and the state of the art of digital image correlation algorithms will be presented.

Testing layout

An example of standard measurement layout for 2D DIC application is reported in Figure 1.

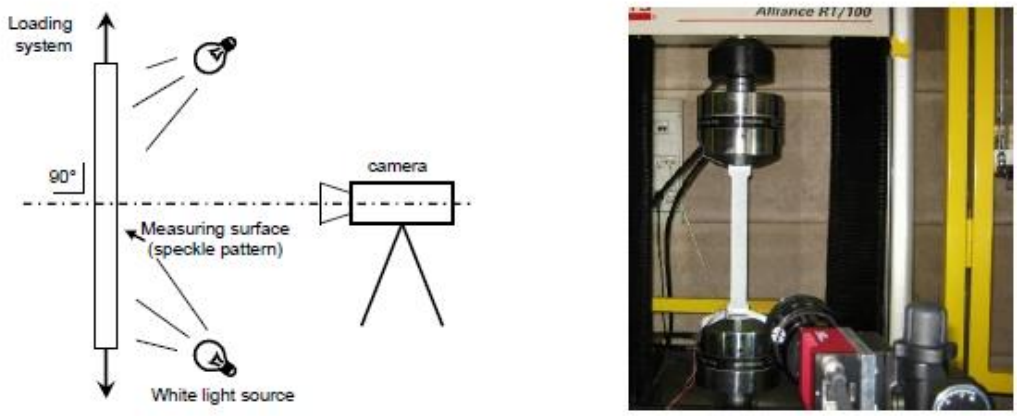

Figure 1 Measurement layout for 2-D DIC

The specimen is mounted on a loading structure (e.g. a standard tensile machine) and lighted by means of white illumination. A digital camera frames the specimen, collecting one static image as reference and several images during the test execution, each of them will be independently analysed to quantify the full-field deformation maps.

Surface properties

Two-dimensional digital image correlation technique works properly when dealing with planar problems. The specimen surface must be flat and out-of-plane displacements or strains field must not arise during the loading [1], [3]. As already mentioned in the introduction, one of the key aspects in which digital image correlation relies on is the surface textures of the specimen. From its analysis it is possible to retrieve the full field displacement map (and consequently the surface state of strain), comparing the gray intensity changes of the surface in the acquired image sequence. A local point-by-point correspondence among acquired and reference images is estimated by the DIC algorithm in the whole analysed area in order to compute the motion field. Being difficult to find the correspondence between a single pixel of an image in a second one (the gray value associated to a single pixel can be found in thousands of other pixels in the second image with no unique correspondence), the analysis extends the searching of a small neighbourhood (called subset) around the pixel of interest.
To reduce the issues related to this “correspondence problem” [3], a randomly textured flat surface is mandatory. This characteristic can be rarely found in the natural texture of tested materials and consequently random textures, namely “speckle pattern”, are artificially applied on the specimen before starting the tests (Figure 2).

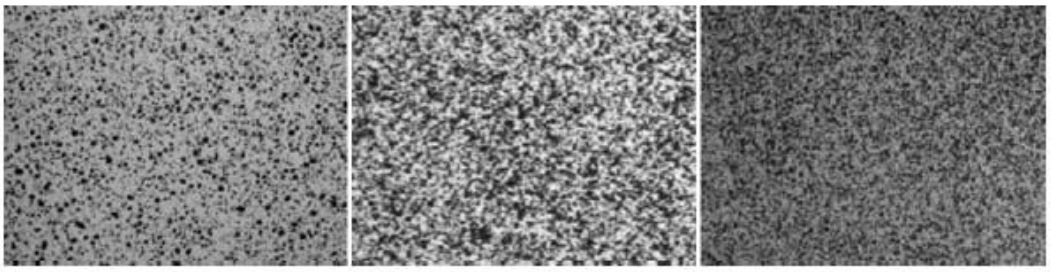

Figure 2 Examples of typical DIC patterns

Subset matching

The basic principle according to which 2-D DIC operates is the matching of the same points (or pixels) between images recorded before and after deformation. In order to compute the displacements of a single point *P*, usually a square reference subset of $(2M + 1) \times (2M + 1)$ pixels centred at point $P\ (x_0, y_0)$ from the reference image is chosen and used to track its corresponding location in the deformed image, as schematically illustrated in Figure 3. The reason why a subset, rather than an individual pixel, is selected for matching is that the subset includes a wider variation in gray levels, being more uniquely identified in the deformed image, as already explained.

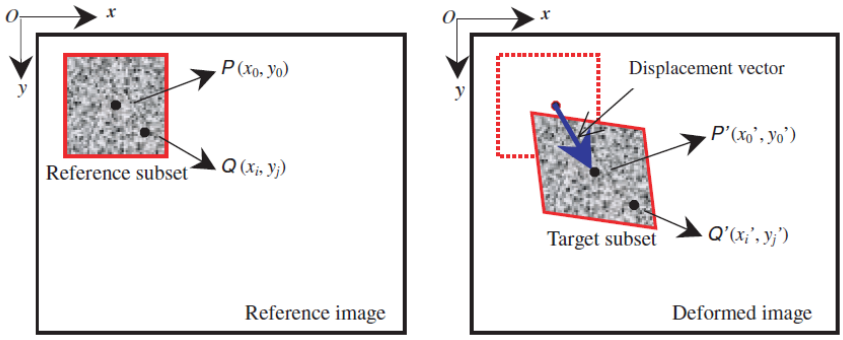

Figure 3 Schematic illustration of a reference squared subset and target subset after deformation

A quantitative evaluation of the similarity degree between the original subset and any selected area of the deformed image has to be introduced, in order to identify P' as the position that best matches P in the whole deformed image. This can be obtained through different (but equivalent) approaches: cross-correlation (CC) criteria, according to which P' is defined as the position that maximizes the cross-correlation function between the original subset and the

deformed subset, or sum-squared difference (SSD) correlation criteria, where P' is defined as the position able to minimize an bi-dimensional error function [27], [28].
In detail, being f the reference image and g the deformed one, and (x_i, y_i), (x_i', y_i') the coordinates in their respective reference systems, the two criteria are defined as:

$$C_{CC} = \sum_{i=-M}^{M} \sum_{j=-M}^{M} [f(x_i, y_i)\mathrm{g}(x_i', y_i')\,] \tag{1}$$

$$C_{SSD} = \sum_{i=-M}^{M} \sum_{j=-M}^{M} [f(x_i, y_i) - \mathrm{g}(x_i', y_i')]^2 \tag{2}$$

For a given square subset of size $(2M\ +\ 1) \times (2M\ +\ 1)$.
Since it has been proven [3] that the presented parameters are sensitive to linear scale and offset in illumination lighting, issues that normally occur during a standard test, their normalized versions (ZNCC – zero normalized cross correlation and ZNSSD – zero normalized sum of squared differences) are generally preferred, able to successfully handle lighting variations [3].

Shape functions and interpolation

It is reasonable to assume that the shape of the reference square subset could change in the deformed image. However, relying on the hypothesis of deformation continuity of a solid object, a set of adjacent points in a reference subset remains as adjacent points in the target subset. Thus, recalling Figure 3, the coordinates of point $Q\ (x_i, y_i)$ around the subset centre $P\ (x_0, y_0)$ in the reference subset can be mapped to point $Q'(x_i', y_i')$ in the target subset according to the so-called shape function [29] or displacement mapping function [30]:

$$\begin{aligned} x_i' &= x_i + \xi(x_i, y_j) \\ y_j' &= y_j + \eta(x_i, y_j) \end{aligned} \tag{3}$$

Where ξ and η identify the analytical formulations of the mapping functions. In addition, the coordinates of point $Q\ (x_i, y_i)$ in the deformed subset may locate at non-integer pixel positions (i.e. subpixel location). To apply the correlation criterion, interpolation of the subset intensity is consequently required. In literature, many different interpolation algorithms have been used to accomplish this task. High order interpolation functions (as bicubic or biquintic spline) must be preferred [31], since they provide higher accuracy and better convergence of the algorithm with respect to a simpler interpolation scheme.

Initial guess of deformation and calculation path

To provide a motion estimation of the central point of the considered subset with subpixel accuracy, the matching procedure is split in two separate steps. The macroscopic position of the subset is identified at first and then refined in order to achieve higher accuracy. In other words, a proper initial guess needs to be provided before starting the subpixel registration algorithms. When the relative deformation or rotation between the reference subset and the deformed one is quite small, the initial guess can be easily estimated with 1-pixel accuracy using both spatial domain [32] or frequency domain [13], [15] methods.
Instead, when the single subset is subjected to large strains or rotations, more complex algorithms need to be exploited [33].

Subset matching-fine matching

A variety of fine matching algorithms for digital image correlation has been presented in the years in scientific literature [1]. Coarse-to-fine searching strategies can be extended to a subpixel accuracy simply changing the searching step from integer pixel values to fractional pixel values [4]. Nevertheless, image interpolation at subpixel values is always required in advance and this results in time consuming approaches.
To overcome this issue, which strongly limits the practical use of digital image correlation, iterative spatial domain cross-correlation algorithms are by far the most adopted fine-matching strategies. In these algorithms, the previously presented shape functions are applied on the reference subset in order to iteratively deforming it until the convergence in the identified area of the deformed image is reached. Newton-Rapson method [34] is the most used searching strategy.

Displacement field measurement

Once a single subset is tracked, the extension to full-field motion estimation is quite trivial. At first, the object region to be analysed (AOI, “area of interest” or “ROI”, region of interest) is manually selected on the reference image (green area in Figure *4*). Within this area, a regular matrix of points to be tracked is identified (red dots): these points represent the subset centres. They are equally spaced in both vertical and horizontal directions, with a predefined grid spacing (usually called “step”). The step among subsets is independent from the subsets dimension, since the regular grid is built partially overlapping adjacent subsets to increase the analysis spatial resolution.

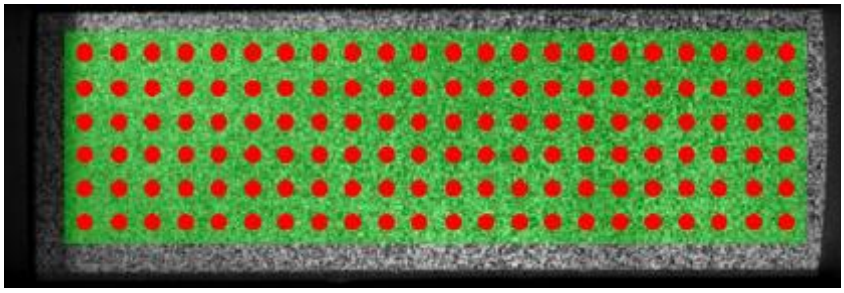

Figure 4 DIC working principle: ROI and subsets definition

Due to the high number of subsets to be tracked, the initialization plus fine matching procedure is too demanding to be repeated for each subset. To speed calculation, the initialization is actually performed only on the first subset and the analysis is carried out by rows (or by columns) using the displacement and strain of the current point as initialization for the adjacent ones [1]. This approach could become critical in case of discontinuities in the displacement field (e.g. associated to cracks in the surface) or high uncertainty in the single subset estimated motion (due for example to local poor textures of the speckle pattern). To solve this problem, in [35] the so called "reliability guided" DIC (RG-DIC) method is presented, where the calculation path is guided by the ZNCC coefficient itself. The subsets used to initialize the neighbourhoods are the ones characterized by the highest matching score in the correlation process. Thus, the calculation path is always along the most reliable direction.

1.3 DIC uncertainty in dynamic applications

As one of the most interesting full-field measurement technique, DIC becomes a relevant topic for the scientific community in the recent years. The available literature in case of static DIC applications is wide and a lot of studies have been done to investigate the main sources of measurement uncertainty coming from this method, aiming to furtherly improve the accuracy of the results. To name a few, M. Bornert et al. [36] proposed a general procedure to evaluate DIC displacement measurements errors. It uses synthetic speckle pattern images undergoing spatially fluctuating sinusoidal displacement fields. They evaluated the RMS error of displacement obtained with various DIC formulations for different subset sizes, speckle sizes and other parameters. The sensitivity of displacement evaluation to the image acquisition noise (e.g. digitization, read-out noise, black current noise, photon noise) were analysed for the first time in [37], [38]. Their analysis was based on corrupting reference image by various levels of zero mean Gaussian noise and without imposing any displacement field on the image. They demonstrated that the standard deviation of the displacement error is proportional to

the standard deviation of the image noise and inversely proportional to the average of the squared grey level gradients and to the subset size.

Wang et al. quantified the expectation (bias) and variance in image motions in presence of uncorrelated Gaussian noise for each pixel location, as a function of interpolation method, sub-pixel motion, intensity noise, contrast, level of uniaxial normal strain and subset size. Their theoretical results showed that the expectations for the local parameters are biased and a function of the interpolation difference between the translated and reference images, the magnitude of white noise, the decimal part of the motion and the intensity pattern gradients [39], [40]. Other studies have been made to theoretically estimate the DIC uncertainty. Among them, Reu et al. quantitatively calculated the errors which will result from any given set of real images obtained in an experiment and concluded that the bias errors can be minimized by selecting higher ordered shape functions, increasing image contrast, and selecting a subset with adequate information content. In addition, they suggested that the variance parameter can be minimized by decreasing intensity noise in the images through better imaging equipment, improved illumination, lower camera gain, averaging multiple images at each step [41]. In the same year, Pan et al. investigated the influence of the speckle patterns on the accuracy and precision of displacement measurement. They derived that the speckle pattern does not introduce systematic error but a random error in the measured displacement [42].

Even though the above-mentioned works were mostly focused on static issues, DIC has been recently exploited in dynamic applications too. Some innovative fields are mode shape recognition [43], [44] and vibration analysis [45], [46]. In 2003, Schmidt et al. [47] implemented digital image correlation technique in two dynamic applications. The first one used short duration white light pulses to study a car tire on road with up to 240 km/h speed. The second study used a pulsed laser to study a flywheel in a spin pit.

Later on, Kirugulige et al. investigated the dynamic crack growth behaviour of a polymeric beam subjected to impact loading using DIC methodology [48]. DIC have been applied also to the problem of modal analysis and vibration measurement. In this group of studies, the results of DIC measurement have been compared with the results obtained from accelerometers, scanning laser vibrometer or finite element method (FEM) [49]–[50].

1.4 Effect of motion blur on DIC uncertainty

Dealing with DIC dynamic applications, the relative motion between a moving target and the camera can cause a motion effect (i.e. blurring) on the acquired images. This motion effect would not exist if the acquisition was instantaneous, but in reality, it is not a valid assumption to be made. In fact, the effective duration in which a camera shutter is open (namely shutter or exposure time) is usually not negligible with respect to the velocity of the target. It means

that a single dot on the target would appear as a stripe on the acquired image, due to the target displacement during the exposure time. Analytically, the phenomenon can be explained assuming that, during the exposure time (T), k scene points pass through the position of the image pixel $P_{i,j}$, with brightness values ($C_1 \dots C_k$) respectively, such that the resulting brightness value for pixel $P_{i,j}$ is given by eq.(4) (in case of continuous movement the summation is replaced by integration). According to this formulation, the blurring of the image exists only along the direction of the motion. This effect of relative motion between the measurand and the camera is known as motion blur.

$$P_{i,j} = \frac{1}{k}\sum_{l=1}^{k} C_l \qquad (4)$$

Motion blur represents an important source of measurement uncertainty using Digital Image Correlation (DIC) technique, which needs to be investigated. Even though in the recent years the scientific community devoted big efforts to analyse and evaluate the most common sources of DIC uncertainty, the literature is missing information able to quantify the impact of motion blur on the total amount of uncertainty. This situation could represent a critical point for many applications involving dynamic strain and displacement measurements. In the early documented dynamic applications of DIC [51], [52], the problem of motion blur was already seen as a relevant one; however, they chose to avoid the quantification of this component by limiting exposure time at the lowest possible value. This result is achieved by boosting lighting at elevated levels with the help of pulsed light.

Figure 5 Example of image blurring in horizontal direction

In the last years significant steps forward have been done. Zappa et al. [53] develop a method able to generate motion effect on a reference image, simulating a real dynamic test and estimating the uncertainty caused by motion blur. In [54], it was analysed how motion blur deteriorates the acquired patterns and how this degradation interferes with measurement uncertainty. In other words, it was modelled a process which defines how the standard deviation of measured displacement was influenced by motion blur.
One of the aim of this thesis is to continue on these directions, investigating which are the effects of motion blur on DIC displacement measurement and then proposing a technique able to improve DIC performances in dynamics (i.e. reducing the measurement uncertainty due to blurring conditions).

1.4.1 MIG and SSSIG indexes

To analyse the effects of motion blur in terms of image degradation and measurement uncertainty, two indexes, widely adopted in the literature, are introduced: the mean intensity gradient (MIG) proposed by Pan et al. [55] and proved to be closely related to both bias error and random error of displacement, and the sum of square of subset intensity gradient (SSSIG), which is mainly focused on the random error due to blur [54].
Let us consider an image where $f(x, y)$ is the pixel intensity at point (x, y), while n and m are the number of pixels in the x and y directions, respectively.
The MIG is computed as the average value of the modulus of the omnidirectional image gradient, normalized by the size of the image:

$$MIG = \frac{1}{m \cdot n} \sum_{i,j=1}^{m,n} \left[\sqrt{\left(\frac{\partial \mathrm{f}}{\partial \mathrm{x}}\Big|_{xi,j} \right)^2 + \left(\frac{\partial \mathrm{f}}{\partial \mathrm{y}}\Big|_{xi,j} \right)^2} \right] \tag{5}$$

Instead the SSSIG is calculated, along the blur direction, as:

$$SSSIG = \sum_{i,j=1}^{m,n} \left(\frac{\partial \mathrm{f}}{\partial \mathrm{x}}\Big|_{xi,j} \right)^2 \tag{6}$$

As we can see from equations *(5)* and *(6),* a good matching exists between such indexes and the DIC working principle, since all of them relies on image gradients.

1.4.2 Blur simulation in case of constant velocity motion

When there is a need to replicate a dynamic test involving DIC technique, sets of reference images of a target are required. The current section describes the numerical approach applied to obtain these groups of images, as presented in [53]. The method allows to simulate both shifting 'a' and blurring 'w' in the generated images, under the hypothesis of constant velocity motion of the target during exposure time. Then, the images can be used to quantify, by means of DIC analysis, the measurement uncertainty induced by motion effect.

Subpixel shifting using DFT

The simulation of the pure translation 'a' of the target is the first step towards simulating the motion effect. Although different methods were introduced in the literature, Fourier shifting method is claimed to be the optimum sub-pixel shifting technique [56]. It is based on convolving the image with a shifted impulse function and it can be resumed in three simple steps:

1. The image is transformed into frequency domain via Discrete Fourier Transform (DFT).
2. A linear phase shift, proportional to the spatial frequency, is applied in the complex plane. The amount of added phase determines the amount of spatial shift.
3. The image is transformed back to the spatial domain via Inverse Discrete Fourier Transform (IDFT).

Note that the transforms are done by means of 1-D DFT/IDFT of a single row or a single column at a time. It is important to remark that the application of a linear phase shift to the image in frequency domain is equivalent to convolving the image with an impulse function at a time different from zero.

Motion effect simulation using square pulse (numerical method)

Different techniques to simulate motion effect are available in literature [57]. However, the numerical method adopted here [53] is based on convolution of the reference image with a square pulse. Before explaining the motion effect simulation technique, a brief review of square pulse characteristics seems to be necessary. The square pulse $g(x)$, symmetric with respect to spatial position $x = 0$, is defined as:

$$g(x) = rect\left(\frac{x}{w}\right) = \begin{cases} 1 & if\ |x| < w/2 \\ 0 & if\ |x| > w/2 \end{cases} \quad (7)$$

Where $'w'$ is the parameter which indicates the width of the rectangle, corresponding to the length of blur generated into the image. It was demonstrated [58], that continuous Fourier transform of this function can be written as follows:

$$G(f) = \int_{-\infty}^{\infty} rect\left(\frac{x}{w}\right) e^{-j2\pi fx} dx = w\frac{sin(w\pi f)}{w\pi f} = w\, sinc(wf) \tag{8}$$

The result of equation (8), models only the situation where the rectangular window is symmetric. In the general case, rectangular window may be translated in space by a generic value a. In this case it is possible to write the acquisition window as $g(x-a)$.
In case of dealing with a shifted square pulse as in Figure 6, the Fourier transform is calculated as below:

$$FT[g(x-a)] = FT[g(x)] \times e^{-2i\pi fa} \tag{9}$$

Where 'a' represents the spatial shift of the square pulse.

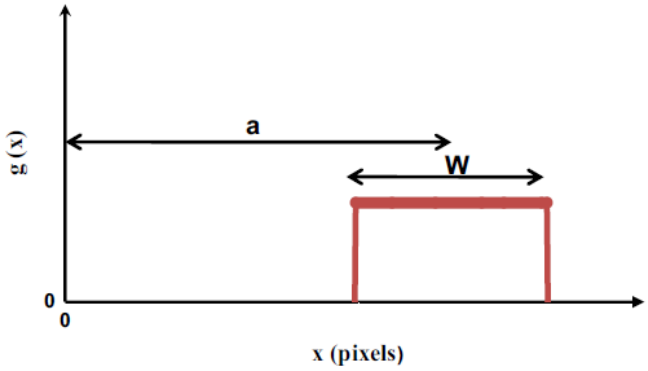

Figure 6 Square pulse g(x) with parameters 'w' (width of the square pulse) and 'a' (shift)

According to equation (8), the continuous Fourier transform of a square pulse is a sinc function. It is important to point out that some differences exist passing to the discrete Fourier transform. It requires the discrete definition of the square pulse in time domain $x[n]$:

$$x[n] = \begin{cases} 1 & 0 \le n \le N \\ 0 & otherwise \end{cases} \tag{10}$$

Starting from that, the DFT of $x[n]$ becomes [58]:

$$x(e^{j\omega}) = \sum_{-\infty}^{\infty} x[n]e^{-jn\omega} = \sum_{n=0}^{N-1} x[n]e^{-jn\omega} = \frac{1-(e^{-Nj\omega})}{1-e^{j\omega}} = e^{-\frac{j\omega(N-1)}{2}} \times \frac{\sin(\frac{\omega N}{2})}{\sin(\frac{\omega}{2})} \quad (11)$$

Since convolution in space domain corresponds to multiplication in spatial frequency domain, the proposed technique suggests calculating the DFT of each row of the image and multiply it by the DFT of the square pulse and finally calculate the inverse DFT of the product. In this way, the final result is a simulation of motion effect in horizontal direction. Note that the same process can be implemented on the columns of the image to obtain blurring in vertical direction. Similarly, repeating the above procedure using a shifted square pulse allows to get a shifted image with motion effect.

Motion effect simulation using square pulse (analytical method)

The limitation of using the numerical method presented before is that the definition of square pulse width in spatial domain permits to handle only integer pixel values. Since there's a need to simulate the motion blur with sub-pixel accuracy, an analytical method was proposed to be applied. It is based on creating the Fourier transform of the square pulse directly in frequency domain. Then, the continuous Fourier transform of the square pulse (i.e. the sinc function) is multiplied by the DFT of each row of the reference image and then the IDFT of the product is computed. An important issue for the implementation of this method is the correct definition of oddity or evenity of the signal length in frequency domain [59]. Figure *7* enhances the differences between continuous and discrete Fourier transform adopted in the numerical and analytical methods, respectively.

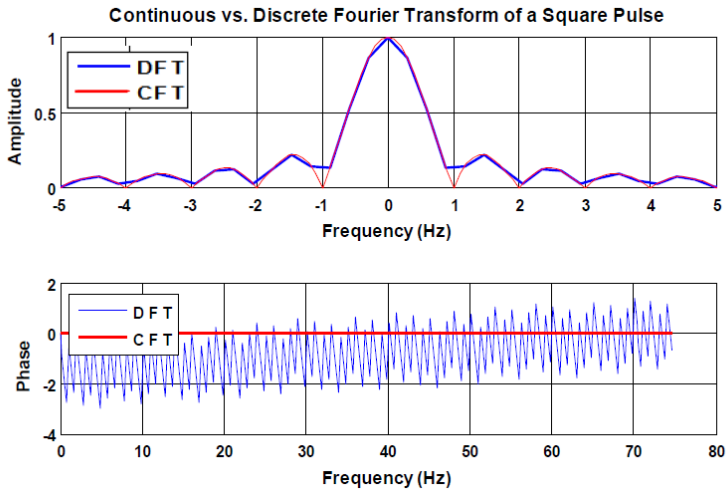

Figure 7 Continuous and discrete Fourier transforms of a centred square pulse having width equal to 1 px

CHAPTER 2
IMAGE DECONVOLUTION AND COMPLEX CEPSTRUM

2.1 Introduction to image deconvolution

In the previous chapter motion blur has been identified as one of the main source of uncertainty when vision systems are applied on dynamic measurands. The effect of blur has been simulated using a theoretical approach based on the theory of convolution. Therefore, convolution phenomena are identified as a relevant issue in dynamic imaging and required the work of several scientists and experimenters.

With analogue photography, it was only possible to try to avoid the generation of motion blur before taking the photo but, once blur has been generated, there was no possibility to recover the frame. Once digital imaging has been introduced during the late 70's, allowing the procedure of storing, analysing and treating images, researchers started to work on the moderation of motion blur on the acquired photographs [60]. At this time the practice of deconvolution de-blurring was born. The research field in deconvolution algorithms started with mono dimensional deconvolution problem applied to general digitally recorded electric signals. The first published article about a deconvolution algorithm was [61]. Since then, the family of deconvolution algorithm have been divided in three:

- blind deconvolution
- referenced deconvolution
- deterministic (non-blind) deconvolution

Blind deconvolution represents the most common case in the generic use of cameras [62], where a blurred image is recovered without knowing the convolution function (also named Point Spread Function, PSF) and without having a non-blurred image of the recorded scene. Referenced deconvolution is the situation where a reference non-blurred picture of the scene is available, while the PSF still remains unknown. Non-blind deconvolution applies when convolution function has been determined experimentally (or known a-priori). Therefore, deconvolution turn into a deterministic problem, which is not in the interest of this dissertation. Anyway, this sector of research attracts a broad interest, due to the application in the field of microscopy [63], medical imaging and astronomy [64].

In any case, the development of deconvolution algorithms has been strongly pushed by the exigence of enhance image readability [65], [66] from a human point of view, without worrying about possible deterioration of metrologic information contained in the image. Lately, the wide diffusion of digital cameras (also embedded in small portable devices) encouraged the development of real time algorithms for image stabilization and enhancement [67], [68].

All these applications require that image processing is done without any a-priori knowledge of the convolution function or of the recorded scene. Hence, almost the totality of researches on deconvolution is focused on blind deconvolution. Purpose of this dissertation, oppositely, is to work on image restoration from a metrologic point of view. Considering that a reference image of the measurand is available, referenced deconvolution is a viable choice. Furthermore, the existence of reference image grants the consistency of some metrologic information (i.e. distances, displacements). However, the task is not trivial, especially for the ill-conditioned nature of the blur operator: the observed image does not uniquely and stably determine the underlying original image [69]. Since the problem is already serious when blur is known, it becomes very critical when there is even a slight mismatch between the assumed blur and the true one. In the field of referenced deconvolution applied to blurring conditions, it is not possible to recognize a homogeneous research path. This is due to the relatively smaller field of application of these techniques. The first recognizable research is [70], where a computational model to calculate motion out of blurred images has been proposed. In this case deconvolution is applied to the marker position time history, rather than on the acquired image. The estimation of deconvolution parameter is done by comparing the width of the original marker with the width of acquired one. Another proposal has been made by Wang et al. [71]. Their research is focused onto estimating vibration amplitude out of blurred image. They gave an optical model of how a target vibrating mono-dimensionally with an unknown amplitude generates a motion blur trail of measured length. In the same year Guan et al. demonstrated the feasibility of recognizing image blur parameters by the comparison of an acquired image with a reference one, even in case of an unknown motion transformation between the two images [72].

2.1.1 Image blur model

The possibility of identifying a reference image for the scene changes completely the way to approach the deconvolution problem. In fact, dealing with dynamic applications, every image recorded from the vision system can be described as the result of a convolution process that transforms the reference image into the grabbed one, as specified in eq.*(12)*:

$$g(x,y) = f(x,y) * h(x,y) + n(x,y) \tag{12}$$

Where $f(x,y)$ is the original image, $h(x,y)$ is the generic function describing the acquisition process (called point spread function, PSF), $n(x,y)$ is the additive noise and $g(x,y)$ represents the grabbed image. In case of a dynamic acquisition, the mathematical description involves a PSF where target translation is followed by frame blurring. Such a procedure can be fully determined only when both rigid translation a and image blur intensity w are identified (Figure 8).

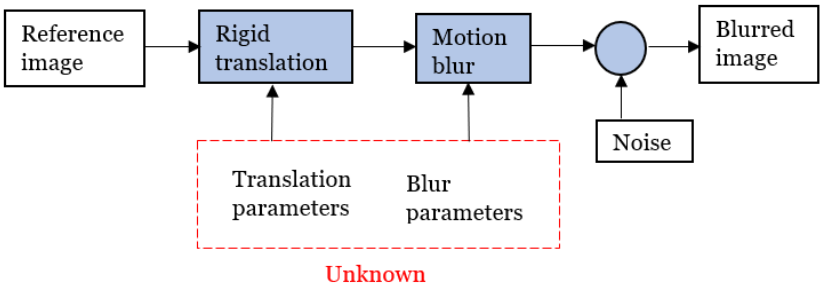

Figure 8 Block scheme describing the process of image acquisition of a moving target

Over the last decade, a great number of works have been introduced for estimating the motion blur point spread function in frequency domain [73], [74]. If a reference (still) image of the acquired target is available, it is possible to formulate the problem in a closed way. The blurring process is modelled as the convolution of the static image with an acquisition window of a given length w and shift a, as described in section 1.4.2.
According to convolution theorem [75], [76] the convolution of eq.(12) becomes a product passing to frequency domain:

$$G(u,v) = H(u,v)F(u,v) + N(u,v) \tag{13}$$

Where $H(u,v)$ is the 2-D frequency response of the PSF, also named Optical Transfer Function (OTF), and $G(u,v), F(u,v), N(u,v)$ are the discrete Fourier transforms of the blurred image, original image and noise, respectively. One approach to determine the acquisition window $h(x,y)$ is to identify the component $H(u,v)$ in frequency domain, which has the form of a sinc function:

$$H(u,v) = w \cdot \frac{\sin(\pi w f)}{\pi w f} = w \cdot sinc(wf) \tag{14}$$

where $f = u \cdot cos(\vartheta) + v \cdot sin(\vartheta)$ represents the blur direction and w is the blur length. Alternate lobes in the sinc produce phase shifts of π radians, and the amplitude at the higher frequencies is attenuated. The estimation of blur extent can be done by searching the zero crossings of the sinc function, taking into account that they occur along the direction perpendicular to the blur orientation and the half-width of the main lobe is inversely proportional to the duration of the acquisition window (i.e. the blur intensity w), as shown in Figure 9.

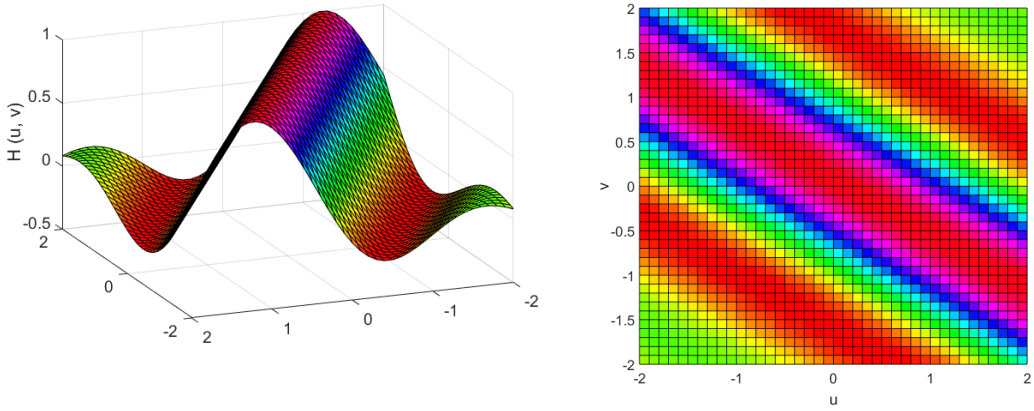

Figure 9 Two dimensional OTF model, having blur intensity equal to 1 and blur orientation of 45°

Since the image degradation process is interpreted as a convolution, image restoration attempts to recover an image by modelling the degradation function and applying the inverse process, i.e. a 'deconvolution'. Once the blurring PSF has been fully identified, it can be removed from the grabbed image in frequency domain with the help of the most common image recovery algorithms.

The basic idea is to perform an inverse filtering, where the Fourier transform of the original image $F(u,v)$ is calculated simply dividing $G(u,v)$ for the degradation function $H(u,v)$:

$$F(u,v) = \frac{G(u,v)}{H(u,v)} \tag{15}$$

This formulation holds only under ideal conditions, where the exact knowledge of the PSF is available and the noise contribution is assumed negligible. Since it is not possible to achieve a faultless $H(u,v)$ description and since the noise effect is always present, the image spectrum after inverse filtering represents only an estimation of the expected one ($\hat{F}(u,v)$).

2.1.2 Wiener filter

Wiener filter is a widely applied filter for image restoration when it has been possible to identify or estimate a certain Point Spread Function able to model the blur [78]. In order to describe the working procedure of the filter let us recall eq.*(12)*, where $g(x,y)$ represents the grabbed image, $f(x,y)$ the blur restored (yet unknown) image, $h(x,y)$ the identified PSF and $n(x,y)$ the uncorrelated noise.
This time the goal is to find a deconvolution operator $p(x,y)$ able to estimate the unknown 2D signal $f(x,y)$ in the way described by eq.(16):

$$f(x,y) = p(x,y) * g(x,y) \tag{16}$$

It has been demonstrated [78] that, under the hypothesis of signals affected by uncorrelated noise, the solution of the exposed problem can be found in the frequency domain and it is expressed by eq.(17), where $P(f)$ represents the deconvolution operator, $H(f)$ the convolution model, $S(f)$ the power spectral density (PSD) of the acquired image $g(x,y)$ and $N(f)$ the noise spectral distribution.

$$P(f) = \frac{H(f)S(f)}{|H(f)|^2 S(f) + N(f)} \tag{17}$$

Since the noise frequency distribution may be hard to retrieve in most of the cases, it is possible to rewrite the previous equation, multiplying and dividing by $S(f)$ the whole expression. At the end eq.(18) is obtained, where the signal-to-noise ratio (SNR) compares.

$$P(f) = \frac{1}{H(f)}\left[\frac{|H(f)|^2}{|H(f)|^2 + \frac{N(f)}{S(f)}}\right] = \frac{1}{H(f)}\left[\frac{|H(f)|^2}{|H(f)|^2 + \frac{1}{SNR(f)}}\right] \quad (18)$$

This last formulation is the most diffused due to its versatility, since it handles SNR either as a frequency distribution or as a scalar value as well.

2.2 Basic theory of cepstrum

The cepstrum was first proposed in 1963 [79] and defined as the power spectrum of the logarithmic power spectrum of a signal. The related application at that time was to determine the depth of the hypocentre of a seismic event, exploiting the function ability to recognise periodic structures. In the recent years, different classifications have been given for the cepstrum, depending on the application that was used [80], [81]. However, the most adopted definitions for signal processing are those of power cepstrum and complex cepstrum. Given a generic signal f, the power cepstrum is defined as the inverse Fourier transform of the logarithmic power spectrum:

$$C_{px}(\tau) = \mathcal{F}^{-1}\{\ln[S_{xx}(f)]\} \quad (19)$$

Where the independent variable τ has the same dimensions of time.
The complex cepstrum, instead, is defined as the inverse Fourier transform of the logarithm of the complex spectrum:

$$C_{cx}(\tau) = \mathcal{F}^{-1}\{\ln[X(f)]\} \quad (20)$$

It has been decided to consider only the definition of complex cepstrum, because it offers many advantages, unlike power cepstrum, related to signal deconvolution.
Complex cepstrum is a real-valued function, whose name indicates that it is obtained from the complex spectrum, with no loss of phase information. For this reason, the process by which it is calculated is reversible, allowing to rebuild the original signal after performing filtering operations [81]. Connected to this, suppose that $x(nT)$ is a signal coming from the convolution of two discrete data sequences,

$$x(nT) = f(nT) * g(nT) \quad (21)$$

and apply all the analytical passages in order to pass to cepstrum domain. The following expressions are obtained:

$$X(f) = F(f)G(f) \tag{22}$$

$$ln\big(X(f)\big) = \ln\big(F(f)\big) + \ln(G(f)) \tag{23}$$

$$c_x(nT) = c_f(nT) + c_g(nT) \tag{24}$$

As can be seen, not only the effects of convolution are separated in the complex cepstrum, but it is possible to remove one completely, and then return to the original signal without this effect. The advantage of doing this in cepstrum instead of frequency domain, is that the former requires to operate only on a single function rather than on amplitude and phase separately.

2.2.1 Applications of cepstrum

Due to its main properties of periodicity and separability, the complex cepstrum can be used not only for harmonic components detection, but also for wavelet recovery, since it is able to retain the phase information. The related literature is rich and varied, and can be divided into pure diagnostic, processing of signals containing echoes [82], [83], speech analysis [84], [85], and machine diagnostics [86].

Cepstral analysis has been extended to image processing. In [87], cepstrum has been used in nonlinear filtering image enhancement, where the logarithm of the Fourier transform is used to amplify the information in the frequency domain and the inverse Fourier transform is used to filter certain features. Other common applications are optical flow estimation [88] and passive stereopsis [89].

The fact that the cepstrum transform maps convolution into addition may be very useful in image deblurring. As the degraded image $g(x, y)$ is the result of convolution of the original image $f(x, y)$ with the blur model $h(x, y)$, it is impossible to separate the blur in spatial domain. However, the blur information can be easily extracted in the cepstrum domain.

The cepstrum of $g(x, y)$ is defined as follows [90]:

$$C_g(p, q) = \mathcal{F}^{-1}\{\ln|G(u, v)|\} \tag{25}$$

where $G(u, v)$ is the Fourier transform of $g(x, y)$ and $\mathcal{F}^{-1}$ is the inverse Fourier transform.

As eq.(25) shows, the image in cepstrum domain is the inverse Fourier transform of the logarithm power spectrum of the blurred image.
For the computational consideration (the logarithm of zero is negative infinite), the cepstrum of an image is also calculated as follows:

$$C_g(p,q) = \mathcal{F}^{-1}\{1 + \ln|G(u,v)|\} \tag{26}$$

Such form magnifies small differences, and keeps the zero values of Fourier spectral nulls.
By converting the model shown in eq.(12) into cepstrum domain neglecting the noise effect, we have [90]:

$$C_g(p,q) = C_f(p,q) + C_h(p,q) \tag{27}$$

The convolution operator in spatial domain becomes additive in cepstrum domain, thus the blur detection is made much easier.
Therefore, the motion effect estimation and the following removal in cepstrum domain is a growing area for the research field. In [91], different approaches to estimate the parameters of motion blur, namely direction and length, are compared directly from the observed image with and without the influence of Gaussian noise. Then, these parameters are used in a standard non-blind deconvolutions algorithm. In [92], the authors proposed a novel method to estimate the parameters of motion blur and out-of-focus from the cepstrum peak detection. Similarly, Shiqian et al. [93] find a procedure to be used for blind image blur evaluation, able to automatically identify the blur type and its relevant parameters. In [94], an algorithm that extracts the blurred object from the background first, and then estimates the parameters of the PSF using the cepstrum method, is described. Final restoration is achieved by using a classical Wiener filter. Experimental results show that the proposed method is able to achieve satisfactory restored images. However, in this dissertation it has been decided to use the cepstral analysis only for the blur compensation step, while for the estimation of the PSF blur parameters a fitting procedure which comes back to frequency domain is adopted (see chapter 3), since it is already consolidated [95] and guarantees a good accuracy of the results.

CHAPTER 3
MOTION BLUR ESTIMATION

In the following chapter, two methods allowing to estimate motion blur parameters are proposed. Suppose to know both the reference still image and its blurred version. Due to the property of cepstral analysis, the difference between the cepstrum of the blurred image and the cepstrum of the reference one permits to extract a function containing all the information about motion blur. Thus, starting from such a difference and passing to a frequency domain analysis, it is possible to evaluate motion blur parameters. At the end of the chapter, the estimation performances are presented, paying attention to the influence of uncorrelated noise and image pattern type on the estimation process.

3.1 Detect motion blur and net displacement using complex cepstrum

The main goal of interest is to extract the most significative motion blur parameters, namely the blur length 'w' and the net displacement 'a', from a generic image of an object, given that a reference image (without motion blur) of the same object is known. To estimate them, an approach based on complex cepstrum is proposed.
As explained in section 2.1.1, blurred images existing in dynamic acquisitions can be modelled in space domain as the convolution between the static image and a rectangular pulse having a width equal to the pixel motion w of the target during the exposure time. According to the convolution theorem, this corresponds, in spatial frequency domain, to the product of the spectrum of the image with the Fourier transform of the rectangular pulse, i.e. a sinc function with half-width of the main lobe equal to $1/w$ (half-width is defined as the distance from zero frequency and the frequency corresponding to the zero crossing of the spectrum amplitude).

Because of the property of the logarithm in cepstral domain, this results in the summation of the cepstrum of the still image with the cepstrum of the rectangular pulse.
Thanks to the separability introduced in cepstrum domain, it is possible to de-convolute (i.e. remove motion blur) by means of a subtraction. More in detail, the difference C_{diff} between the cepstrum of the blurred image C_B and the original image C_R contains all the information about motion blur. Ideally, if noise or other transformations did not occur, $C_B - C_R$ is identically equal to the cepstrum of the rectangular pulse with generic width w. Thus, computing such difference and applying inverse complex cepstrum back to the spatial domain, should return the shape of a rectangular window, having a width equal to the motion blur value and a shift equal to the net displacement. Two key issues are related to this last point.

- Since the spatial resolution for images is the pixel unit, the description of window function in spatial domain allows to manage only the case of integer motion blur value. When dealing with non-integer values of motion blur, the spatial resolution is insufficient to reconstruct correctly the underlying transformation.
- The second limit appears in Figure 10. The blue line is the square pulse defined directly in spatial domain, with a shift equal to 60 px and width equal to 20 px, while the red line shows the square pulse calculated by inverse Fourier transform derived from frequency domain.

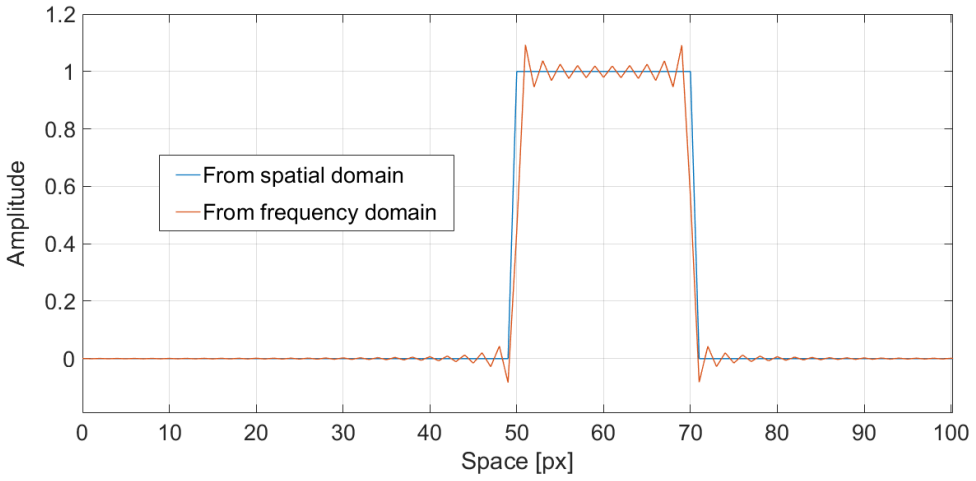

Figure 10 Shifted square pulse derived from spatial and frequency domain

Even though in this case the blur is an integer value, the discrepancy between the two methods comes from the fact that the "theoretical" window function in frequency domain should be described as an infinite series of points (according to its definition), while in a sampling case it is considered as a sinc function with a finite number of lobes.

It is possible conclude that extracting information of motion blur directly from inverse complex cepstrum, which includes the transformation from frequency to spatial domain, is not accurate. The issue is solved here applying only the first steps of the inverse cepstrum calculation, stopping the process when the frequency domain counterpart of C_{diff} is obtained. The latter is named F_{diff}. In frequency domain, F_{diff} data nominally distribute according to the Fourier transform of the rectangular pulse: i.e. a sinc function with half-width of the main lobe equal to $\frac{1}{w}$. This is confirmed by Figure 11, where the resulting F_{diff} is very similar to a sinc kernel.

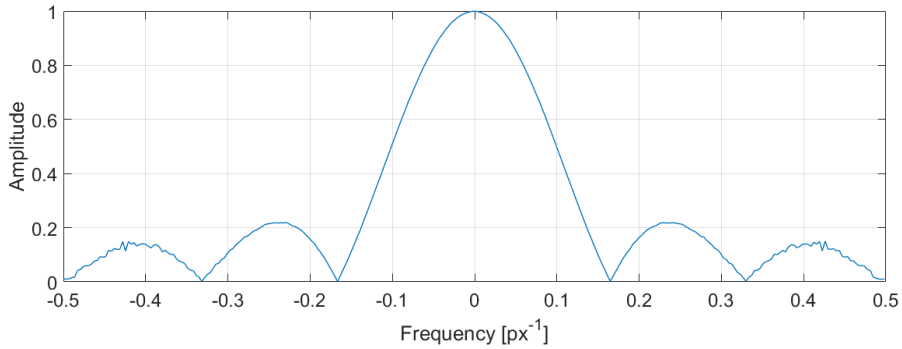

Figure 11 Absolute value of F_{diff} obtained from modified inverse cepstrum for the case w=6 px

For a given blurred image, the detailed procedure to obtain the Fourier transform of motion blur (F_{diff}) with the inverse "modified" cepstrum, is the following:

a) First, for both the blurred and reference images, compute the cepstrum of the same row (in the case of horizontal motion) or column (in the case of vertical motion).
b) Subtract the cepstrum of the row (or column) of the reference image C_R from the cesptrum of the row (or column) of the blurred image C_B.
c) Apply the "modified" inverse cepstrum on the difference $C_{diff} = C_B - C_R$.
d) Repeat the procedure for all the rows (or columns) present in the images and then average the results. Note that this resulting signal represents the DFT of a 1D square pulse with determinable 'w' and 'a' parameters (F_{diff}).

3.2 Estimate motion blur and net displacement

Once obtained the Fourier transform of square pulse (F_{diff}) with the "modified" inverse cepstrum, the following step is to extract blur parameters from it. Two techniques able to estimate motion blur are proposed:

- Sinc fitting method, which is the most accurate, even though it requests higher computational efforts and it could give not reliable results in case of small *w* values.
- First estimation method, which is simpler and requires low computational efforts. However, it is capable to give only a rough estimation of blur.

3.2.1 Sinc fitting method

Since for the generic image the values of F_{diff} may be dispersed due to noise and other transformation, a fitting procedure (where the fitting function represents a sinc kernel) of its amplitude and phase returns a reliable estimation of motion blur parameters.
Before describing the algorithm, it is necessary to make an observation in advance. Let us consider an image having a small value of motion blur (i.e. lower than one) and calculate F_{diff} by means of "modified" inverse cepstrum, as explained in the previous section.
Since the width of the main lobe is inversely proportional to the length of motion blur and since the Nyquist frequency in image processing is 0.5 px^{-1}, when the blur value is rather small the first lobe of the sinc function appears too wide to be completely shown in the considered frequency range.

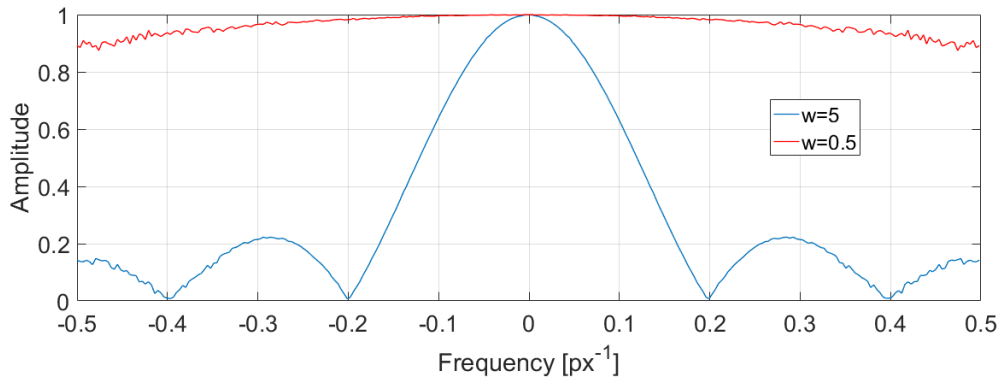

Figure 12 F_{diff} for different values of blur

In Figure 12 is reported the comparison between two sinc-like functions (F_{diff}) coming from distinct values of motion blur. For w=0.5 px, the plot is quite flat and does not reach the minimum point of the main lobe inside the visible frequency range. Moreover, the shape of the function becomes noisy as frequency increases, worsening the fitting accuracy.
A possible solution to overcome this problem is to select only one portion of the plot on which performing the fitting to estimate blur parameters. In particular, there is a need to set a threshold for the amplitude of F_{diff}, such that the fitting algorithm operates only in the part from zero frequency to the first frequency at which the amplitude equals the threshold.
For low values of motion blur the main lobe of F_{diff} is flat, meaning that a high threshold (close to one) is required. Conversely, as blur increases, a lower threshold can be used for the fitting, because the main lobe becomes steeper.
In agreement with that, an automatic procedure is implemented, able to select for each value of motion blur the most appropriate threshold, depending on the value assumed by the ratio between the "slope" of the fitting function and the level of "noise" present in F_{diff}. The basic idea on which it relies is that for small values of blur, where the spline shape is flat and the noise contribute in the main lobe of the F_{diff} is relevant, the resulting ratio results very small. As the blur grows, the slope of the spline increases, and noise reduces, bringing to an overall raise of the ratio. So, the user has only to introduce a reference value for the ratio (named *ratiolimit*), beyond which it is possible to fit F_{diff} from the higher to the lower amplitude.
The overall procedure is described in detail as below:

a) Fit the F_{diff} function with a spline.
b) Calculate the "slope" of the spline as difference between its maximum and minimum point.
c) Calculate the standard deviation of the difference between F_{diff} and the corresponding fitting function, which represents an index for the level of "noise".
d) Calculate the *ratio* slope/noise.
e) Compare it with the limit reference ratio. If *ratio* < *ratiolimit* (small blur), perform the fitting on the portion of main lobe up to the higher threshold amplitude. If *ratio* > *ratiolimit* (high blur), perform the fitting on the portion of main lobe up to the lower threshold amplitude.

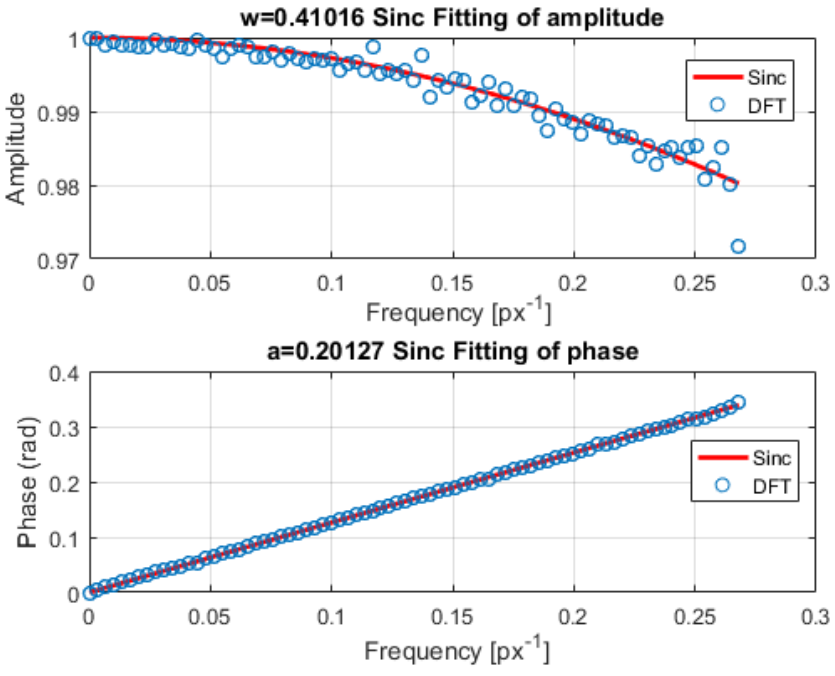

(a)

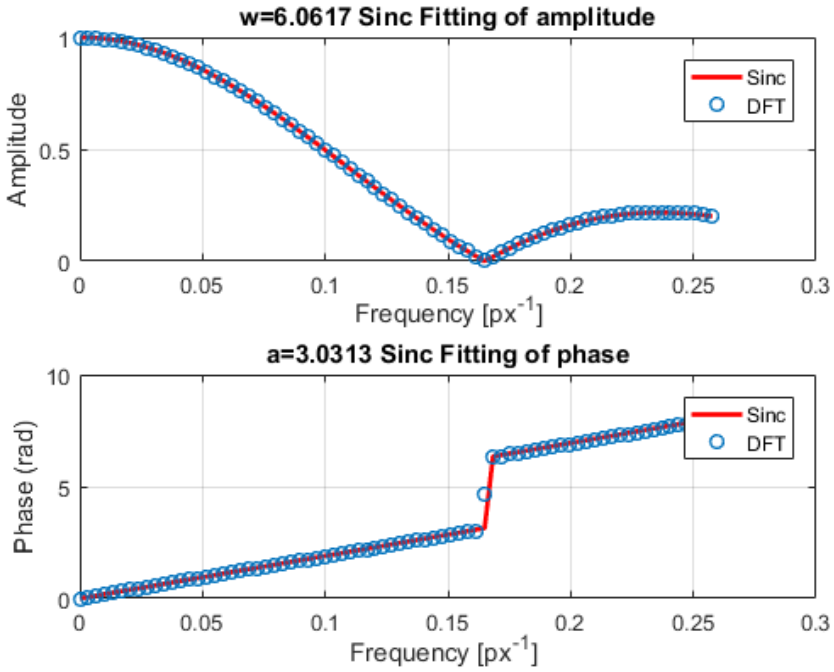

(b)

Figure 13 Sinc fitting method for different values of blur. (a) w=0.4 px, a=0.2 px. (b) w=6 px, a=3 px.

In Figure 13, the function F_{diff} coming from "modified" inverse cepstrum and the corresponding fitting spline are plotted for two different values of imposed motion effect and shift. The comparison of Figure 13 (a) with (b) reveals that in both cases the imposed shift is correctly interpolated. Conversely, the graphs show better fitting when it comes to higher motion blur values w, while in presence of lower motion effect, where the amplitude of the DFT signal is almost constant (close to 1), fluctuations in the curve due to noise become critical and misleading for the fitting procedure.

3.2.2 First estimate method

As just explained, since the fitting accuracy reduces dealing with small values of motion blur, a method able to get a first estimation of motion blur in advance is necessary, in order to compare it with the results coming from fitting. Therefore, a complementary technique is proposed, which is simple and works quite well with low values of blur. The procedure is described in detail as below:

a) Compute analytically the integral of the absolute value of theoretical sinc function between minus Nyquist frequency and plus Nyquist frequency (e.g. $-0.5\ px^{-1}$ to $+0.5\ px^{-1}$ in image processing) as a function of w. In this case, a series of sinc function having the form $sinc\ (freq * w)$ are considered, where w ranges from 0 to 8. Each time for a specific motion blur value w, the integral command is used to calculate the area under $sinc\ (freq * w)$, called "AVG_sinc". As motion blur w varies, a curve representing the values of "AVG_sinc" versus w is obtained, like the one in Figure 14.

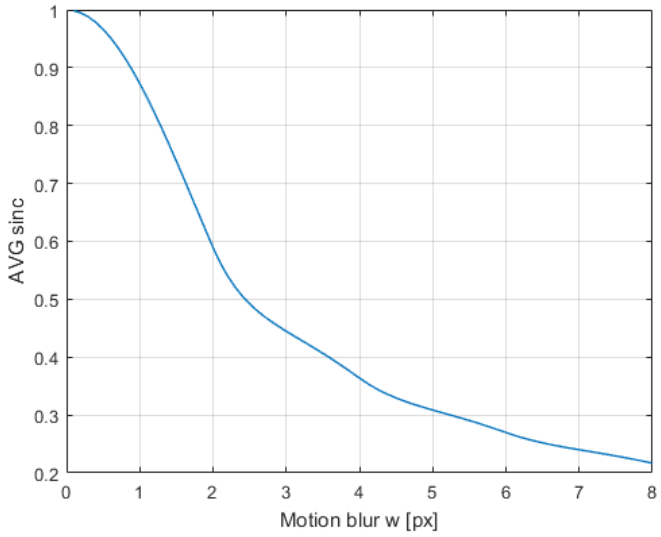

Figure 14 Area under sinc function (AVG sinc) for different values of motion blur

For small motion blur, the first lobe of sinc function is flat and nearly equal to one into the Nyquist frequency range. So, the overall area under sinc function approaches the value 1*[0.5- (-0.5)] =1. When blur increases, as in the case of w=5 px in Figure 12, both the main lobe and lateral lobes appears in the frequency range. The amplitude of sinc function varies from 1 to 0, resulting in an underlying area smaller than one. It is possible to conclude that, as motion blur increases, the area under sinc function decreases.

b) Select a blurred image and compute the cepstrum of the rectangular pulse (F_{diff}) in the same way explained at the beginning of section 3.1.

c) Fit F_{diff} with a spline and calculate the underlying area, (which is indicated by "AVG_exp"). The considered frequency is always from minus Nyquist to plus Nyquist.

d) Enter in the diagram obtained at step a) with the value of "AVG_exp" to get the first estimation of motion blur.

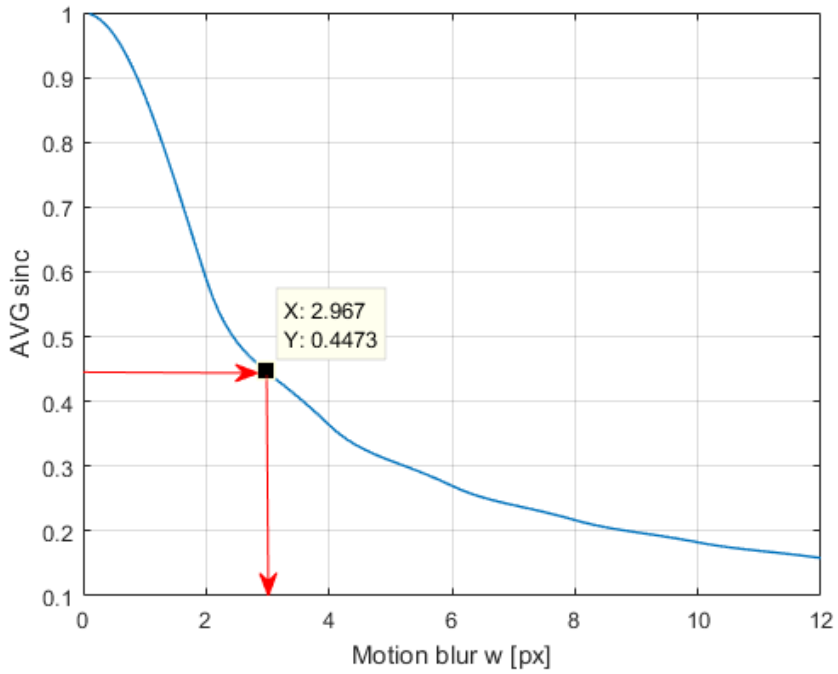

Figure 15 Example of First estimation method application

The example of Figure 15 indicates that, if the area AVG_exp is equal to 0.4473, according to the diagram "AVG_sinc vs motion blur", the first estimation of motion blur is 2.967 px.

3.3 Error of estimation for different reference images

To validate the whole procedure, three different types of synthetic DIC pattern were used. For each pattern, motion blur is numerically simulated according to the analytical method described in section 1.4.2. Motion blur levels up to 8 px were generated. Then, both Sinc fitting and First estimation methods were applied. The aim is to understand either the performances of the two techniques varying motion blur intensity or the influence of the image type on the estimation process. Finally, Gaussian noise is added to each blurred image, to simulate a real digital acquisition and to study the impact of noise in the estimation reliability.

3.3.1 Case 1: Realistic DIC speckle

In case 1, a reference image having a regular speckle pattern (named '*Fullspeckle'*) and designed for the specific use in DIC applications is adopted (Figure 16).

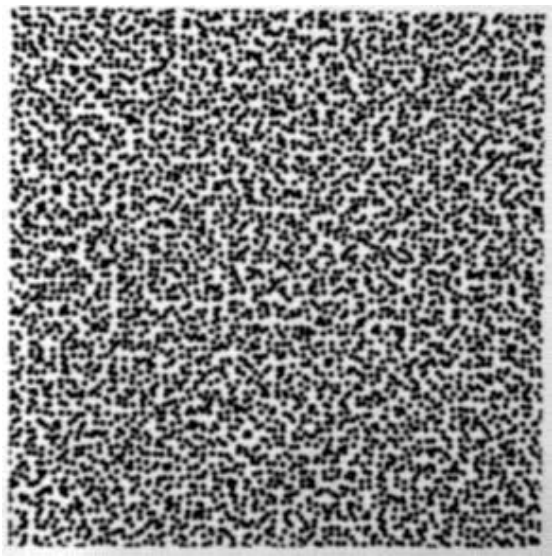

Figure 16 Reference image for Case 1

To study the influence of noise on the generated images, Gaussian noise is added to each blurred image in two distinct levels, to understand how the estimation error trend varies. Since 8-bit images are considered, whose full dynamic range is between 0 and 255, noise level1 and noise level2 are two zero mean Gaussian noises with standard deviation of 2% and 8% of 255, respectively. It's important to underline that the addition of noise modifies the variability of the F_{diff} function (Figure 17), reducing the previously described ratio slope/noise.

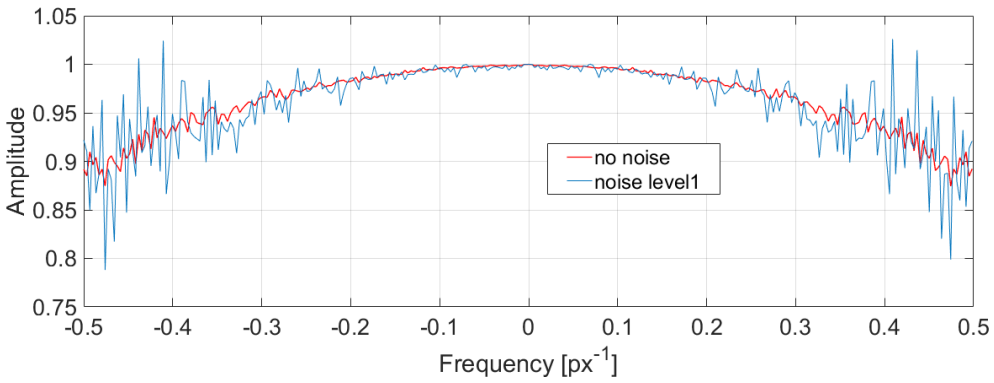

Figure 17 Influence of noise on sinc function behaviour

Thus, there's a need to redefine the limit ratio according to which it is possible to pass from the fitting of F_{diff} with a higher threshold amplitude to the one with a lower amplitude. The adopted fitting parameters are the same for all the types of pattern and are reported in Table 1.

Table 1 Fitting parameters for the considered pattern types

Fitting parameters	No noise	Noise level1	Noise level2
ratiolimit	5	0.45	0.15
Thresh amp max	0.98	0.91	0.85
Thresh amp min	0.3	0.5	0.5

In Figure 18 are reported the results, in terms of estimation error, obtained applying Sinc fitting and First estimation methods on 'Fullspeckle' images, expressed as difference between the nominal blur value and the estimated one.

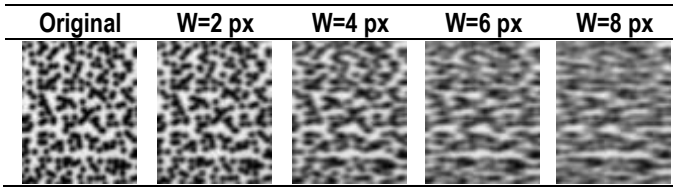

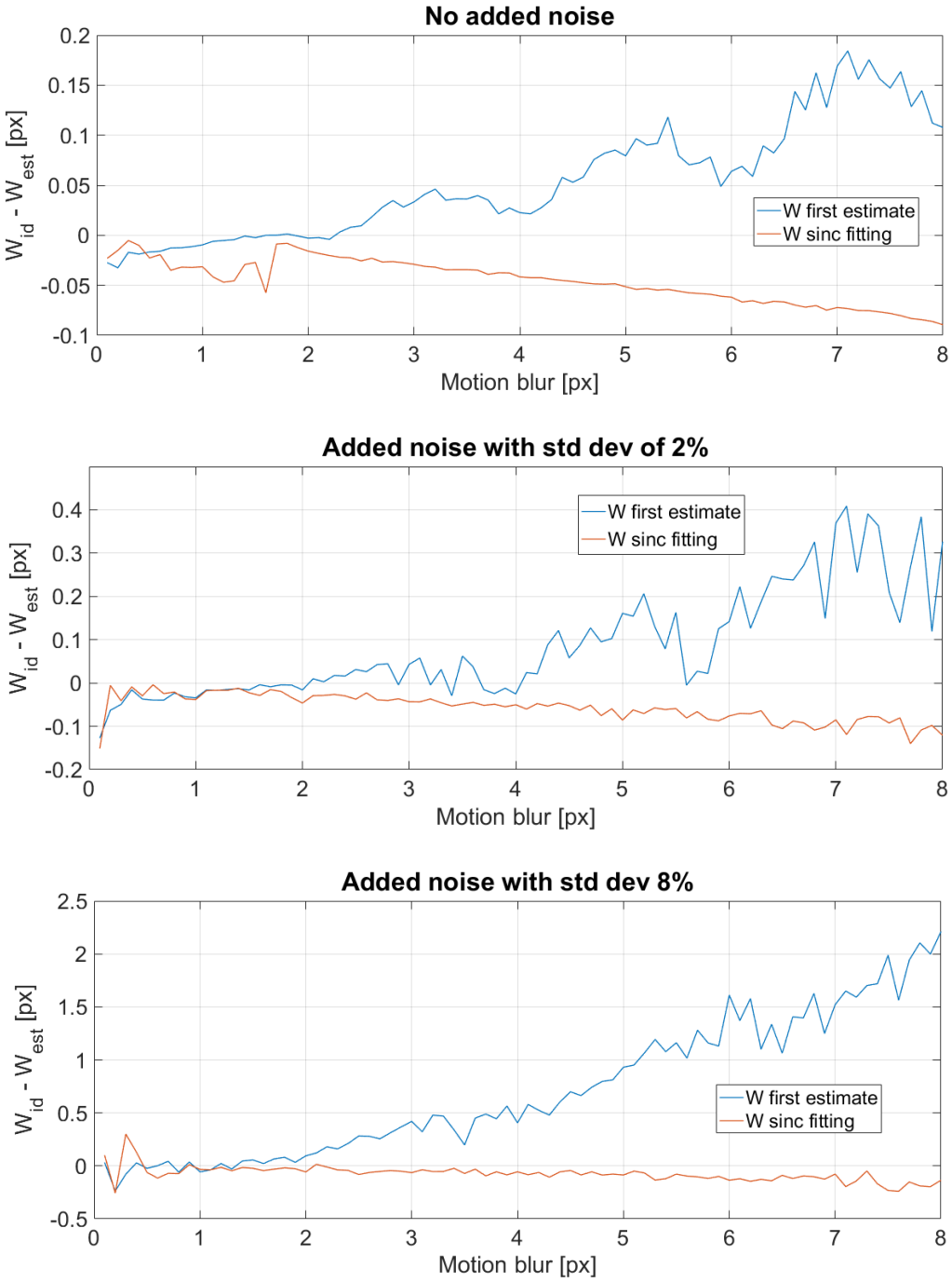

Figure 18 Error of estimation for Case 1

3.3.2 Case 2: 'Sample 3b' from DIC challenge

The purpose of the SEM's DIC challenge [96] is to supply a set of images for software testing and verification. The use of a common image data set removes the experimental errors associated with multiple hardware, providing a framework in which all codes can be tested, validated and improved for use in experimental mechanics.
These types of DIC pattern are tested to verify the robustness of our technique. In this section, 'Sample 3b' from DIC challenge database is used as reference image (Figure 19).

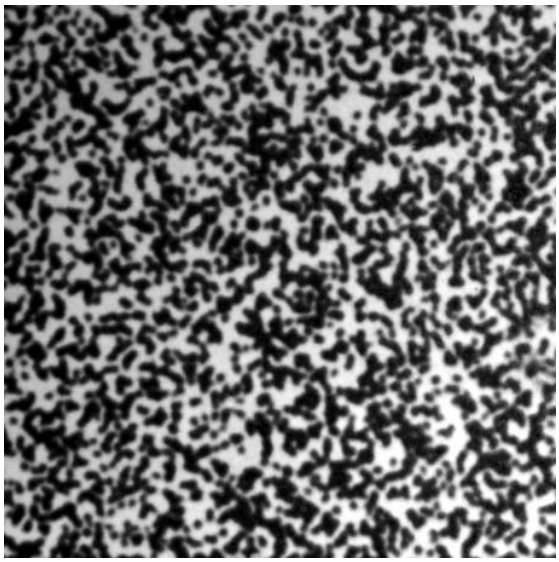

Figure 19 Reference image for Case 2

Also in this situation, the same procedure and analysis implemented for case 1 is carried out, and results reported in Figure 20.

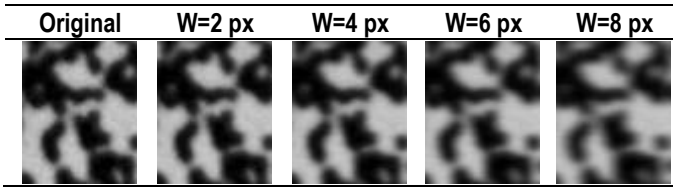

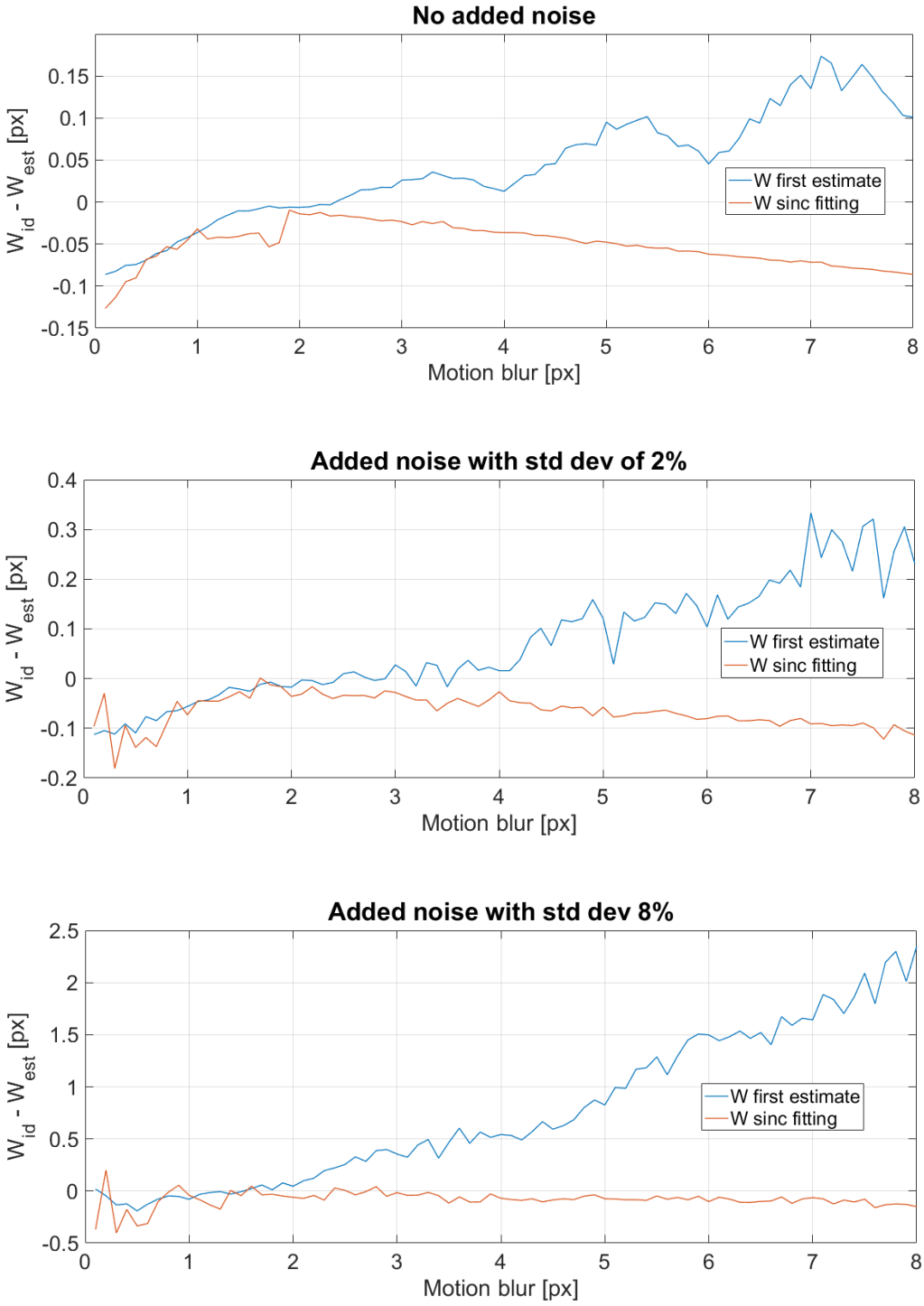

Figure 20 Error of estimation for Case 2

3.3.3 Case 3: Sample 7 from DIC challenge

In this section, the reference image 'Sample 7' from DIC challenge database is tested (Figure 21)

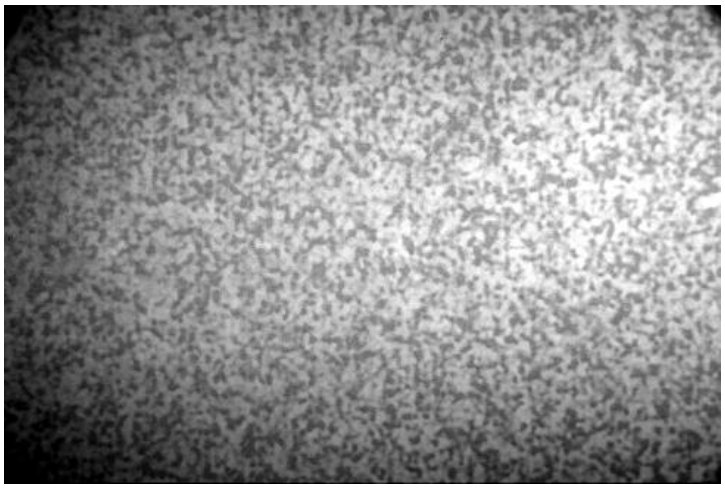

Figure 21 Reference image for Case 3

Again, the same procedure and analysis implemented for case 1 and case 2 is carried out, and results reported in Figure 22.

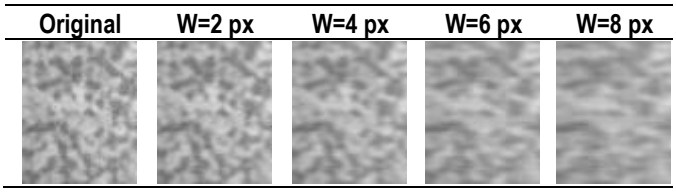

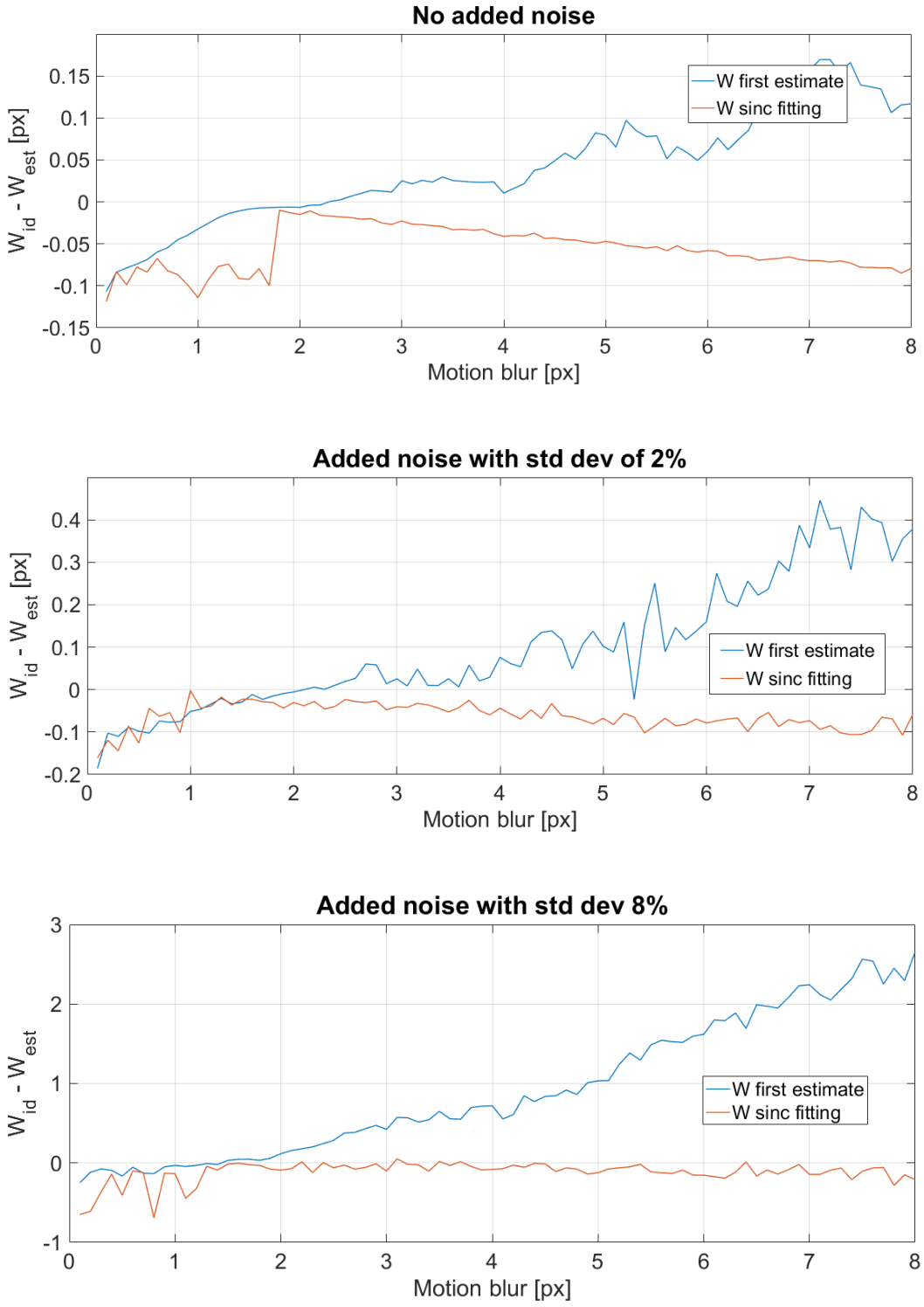

Figure 22 Error of estimation for Case 3

3.4 Comparison and analysis

In the following paragraph the estimation error obtained at the previous steps is analysed in detail, to validate the robustness of the proposed estimation algorithm.
The first general conclusion that emerges from the graphs of sections 3.3.1, 3.3.2, 3.3.3 is that Sinc fitting is the most reliable method when dealing with high values of motion blur, while for very small values (w<1 px), the relative error increases, because the motion blur is too small to get a meaningful result. For this latter situation, First estimation approaches better the nominal values. From now on, it has been decided to take into account only Sinc fitting technique, since when w is very small, it can be considered negligible with respect to the further purposes (impact on DIC uncertainty).
Then, the results between no-noise estimation and with-noise estimation for each image pattern are compared, to infer the influence of noise on motion blur estimation. Finally, the analysis moves on the influence of image pattern on motion blur estimation.

3.4.1 Influence of noise on motion blur estimation

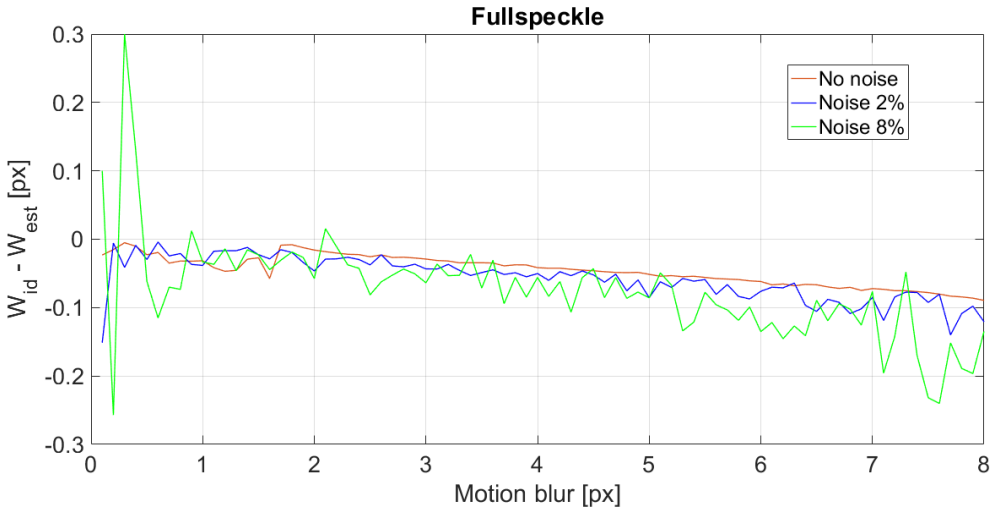

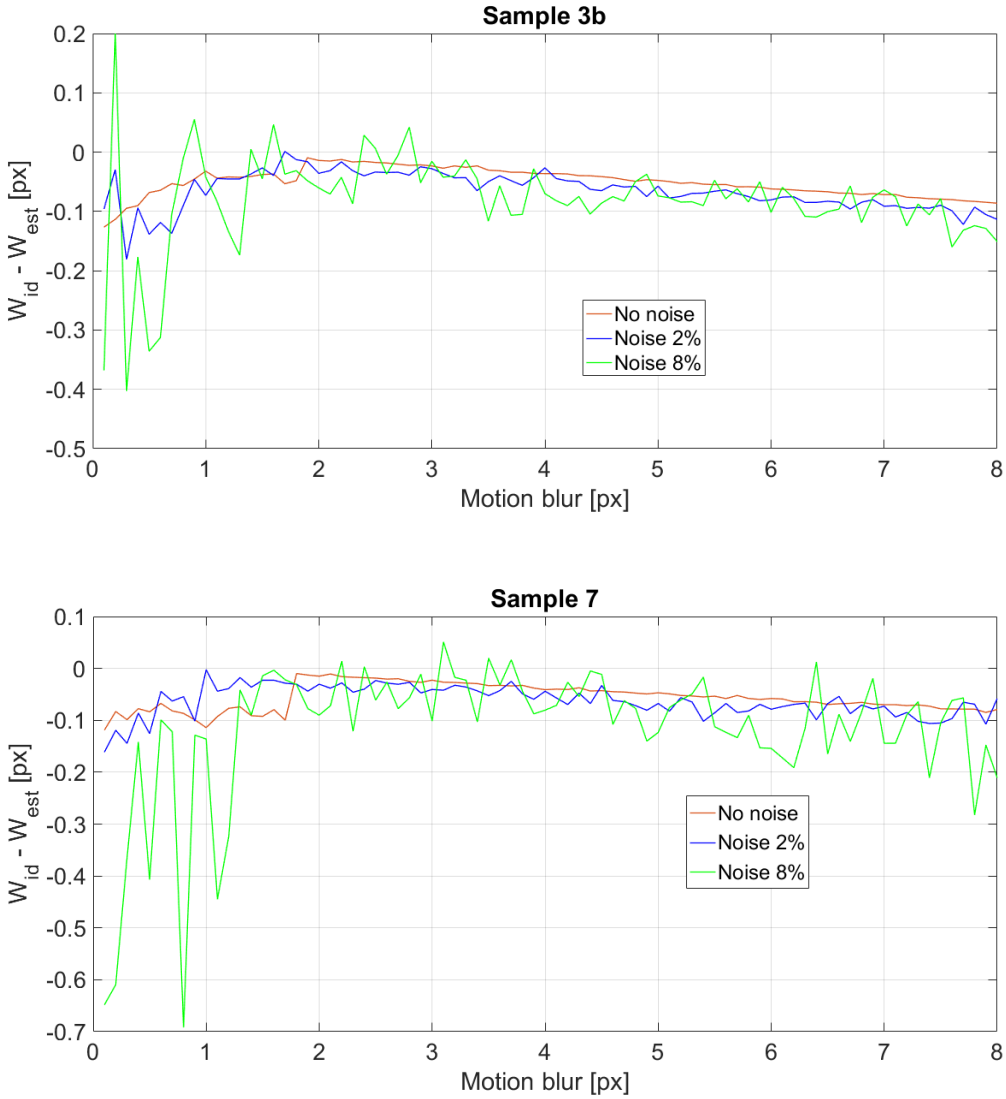

Figure 23 Influence of noise on blur estimation for different image types

As can be seen from Figure 23, the relative error increases proportionally to the amount of noise for all the considered image types. Adding noise enhances both the uncertainty in motion blur estimation and, as consequence, the uncertainty of the following image processing techniques, as blur compensation and DIC analysis. It should be noted that images without presence of noise represent only an ideal case, given that modern cameras usually operate with a noise level between 0.5% and 2% of the dynamic range [97]. Since for all image types the blue curve (no noise) and the red curve (added noise level1) are very similar, it can be inferred that, although adding moderate levels of Gaussian noise to the image affects the estimation process, the blurring due to motion remains the predominant source of error.

It is possible to conclude that Sinc fitting algorithm works well for low-noise acquired images, even though it shows a strong sensitivity when noise level increases; as represented by the green curve, the estimation error becomes important where noise standard deviation reaches 8% of 255.

3.4.2 Influence of image type on motion blur estimation

For a better awareness of the characteristic features of the involved patterns, in Figure 24 the histogram of the pixel distribution for each grayscale value is plotted.

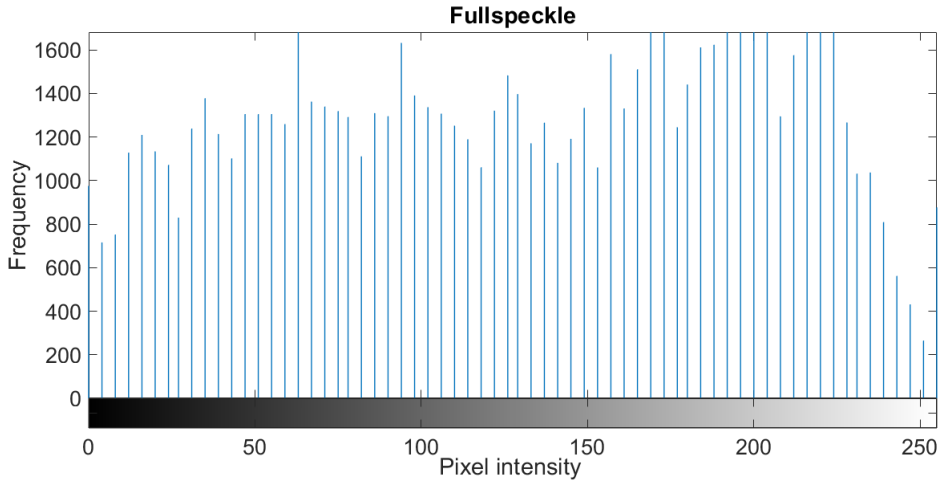

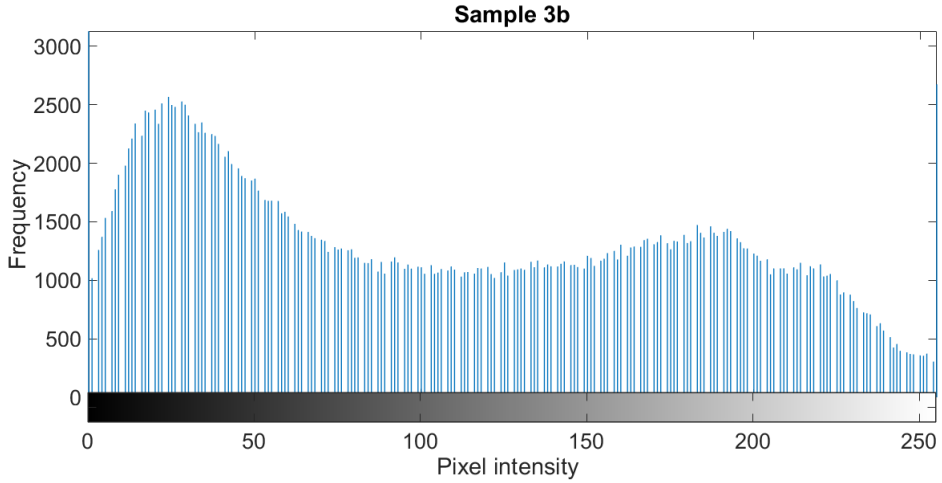

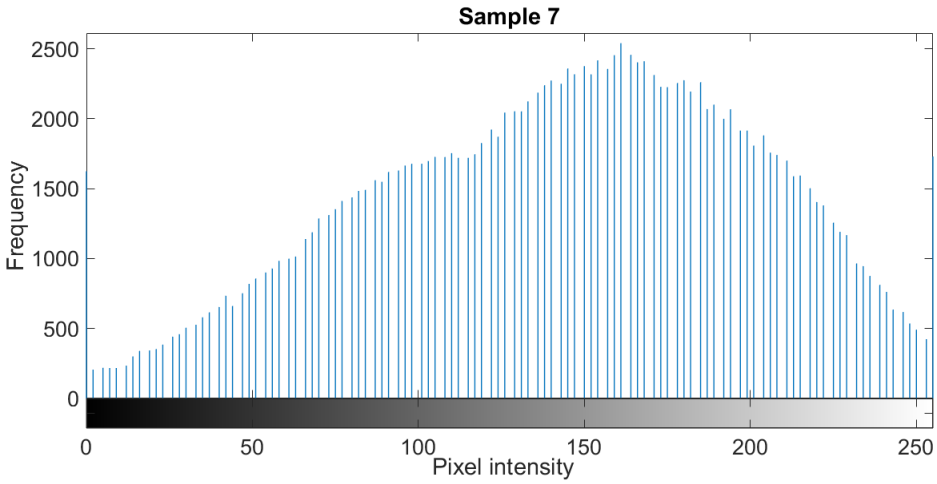

Figure 24 Histogram of pixel intensity distribution for reference images of Case 1, Case 2, Case 3

In the first pattern, pixel values are homogeneously distributed over the whole intensity range (sharp contrast). The same occurs in pattern of Sample 3b, except for a more concentrated pixel distribution in the darker area. In the third pattern, instead, pixels values are clustered in a rather small area (low contrast).

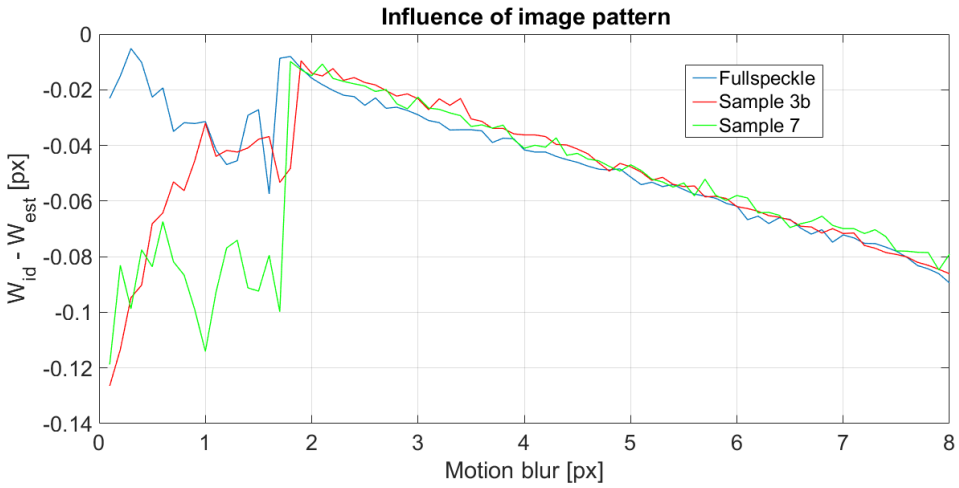

Figure 25 Influence of image type on motion blur estimation

Through the combined use of Figure 24 and Figure 25, it is possible to understand that also image pattern affects the estimation process. When blur is large (w>2 px), the trend of relative error is almost the same for all the images, while for small blur values the presence of sharp contrast helps to increase the reliability of the results.

Before concluding this chapter, it is interesting to look at a situation in which the error of estimation coming from Sinc fitting is unreliable. Let us consider 'Sample 7' as reference image, with blur length w=0.8 px and added noise level2. It can be testified from Figure 26 that the notable discrepancy between the nominal and the estimated blur value is due to the contemporary influence of low blur, presence of noise and low contrast pattern, which are dangerous parameters for an accurate fitting of the F_{diff} function.

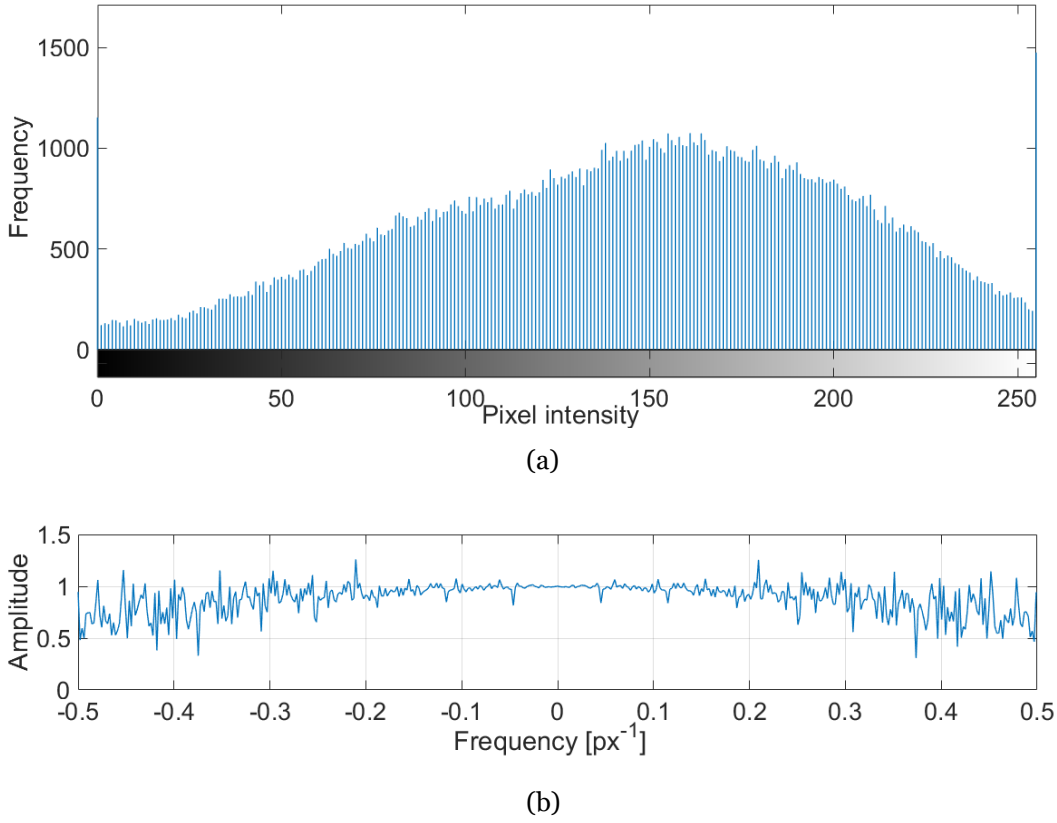

Figure 26 Histogram (a) and shape of F_{diff} function (b) of Case 3, with w=0.8 px and noise level2

CHAPTER 4
MOTION BLUR COMPENSATION

In the previous chapter a deconvolution analysis which operates in cepstrum domain has been performed to estimate the motion blur within a given image. Once motion blur has been completely identified, the next step provides for its removal. The compensation of motion blur is pursued by means of two methods: one is based on cesptral analysis and the other on the use of Wiener filter. Both are presented in this section and validated later on.

4.1 Deconvolution algorithm using complex cepstrum

The starting point of the estimation process developed in chapter 3 was to consider a static image and the same version corrupted by motion effect to identify the Fourier transform of the square pulse F_{diff}. Its absolute value and phase contains information about motion blur length and net displacement, respectively. Once they are known, it is possible to adopt the inverse procedure, relying on convolution and cepstrum properties, to remove motion blur and return to the restored image.

From section 3.1, it was claimed that the description of square pulse in space domain is not accurate, since it deals only with the case of integer motion blur values. To manage sub-pixel accuracy, there is a need to define the rectangular window in frequency domain.

The blur removal procedure assumes that the blurred image is simulated by convolving static image with a square pulse. This corresponds, in accordance to convolution theorem, to the pointwise product of their respective spectra in spatial frequency domain. Due to the properties of cepstrum, the product becomes a summation. Thus, it is possible to eliminate the effect of square pulse (motion blur) by a simple subtraction in cepstrum domain and then, by

computing backwards to space domain through inverse cepstrum, the image without blur is obtained. The transforms are done considering one row or one column at a time, depending on the blur direction. Pay attention that in this specific case it is assumed to remove both the motion blur and the net displacement. Since the original cepstrum code developed in Matlab (*'cceps.m'*) deals only with input in space domain, it has been modified to accept also input signals in spatial frequency domain. The applied procedure is described in detail as follows:

a) Define the square pulse in frequency domain, which is represented by a sinc function of assigned parameters related to motion blur length and net displacement. Note that, to remove both the motion blur and net displacement, the expression of the sinc function is the same of eq.(9), except for the sign of the phase which must be opposite:

$$G(f) = w\ sinc(wf) * e^{2i\pi fa} \tag{28}$$

b) Compute the cepstrum of sinc function.
c) Compute the cepstrum of a row (in the case of horizontal motion) or a column (in the case of vertical motion) of the blurred image.
d) Subtract the cepstrum of the sinc from the cepstrum of the row (or column) of the blurred image.
e) Compute the inverse cepstrum of this subtraction.
f) Repeat the procedure for all the rows (or columns) of the blurred image. The corresponding result will be the restored image.

4.2 Blur compensation for different reference images

To validate the effectiveness of the blur compensation method just proposed, several tests are carried out on the image groups just considered in chapter 3.

- First, starting from the static image and using the motion effect simulation method, the blurred image with the desired nominal motion blur length (w_{nom}) and nominal net displacement (a_{nom}) is generated.
- Secondly, the motion blur estimation methods (i.e. First estimation and Sinc fitting) are applied to extract blur parameters (w_{est} , a_{est}).
- At this point, a sinc function in frequency domain having nominal blur parameters is generated and used to compensate the blurred image.

- The last step is like the previous one, with the only difference that the image is deblurred using a sinc function defined with the estimated motion blur values.

The following analysis are focused on image types having specific blur values, in particular:

- Since very small values of blur (w<1 px) can be considered negligible for the purposes of this work and since Sinc fitting is not very reliable there, it has been decided to test as first the case where w=2 px.
- To check the effectiveness of deblurring technique on images with non-integer blur value, the result of deblurring when w=4.5 px is reported.
- To check the effectiveness of deblurring technique on images with relatively large and not-integer blur value, the result of de-blurring when w=7.7 px is reported.
- To understand if some differences occur in deconvolution by changing the image type, the results of deblurring in case of regular DIC pattern ('Fullspeckle') and DIC challenge's patterns ('Sample 3b', 'Sample 7') are compared.

4.2.1 Case 1: Regular DIC speckle ('Fullspeckle')

From Figure 27 to Figure 29, the compensation results are shown for different blurred images, when sinc function is defined either with nominal or with estimated values (coming from Sinc fitting) of motion blur.

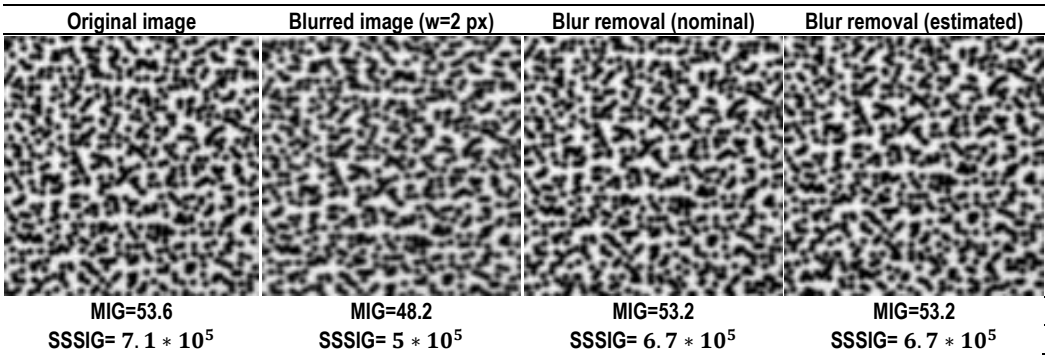

Figure 27 Compensation results for Case 1 (w=2 px and a=1 px)

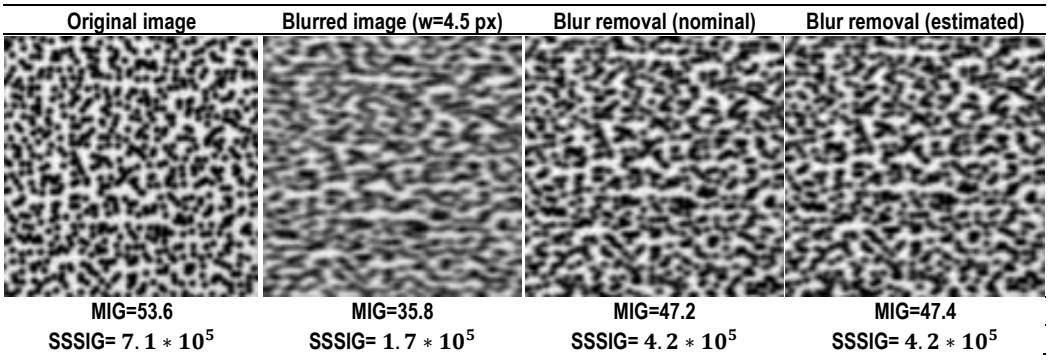

Figure 28 Compensation results for Case 1 (w=4.5 px and a=2.25 px)

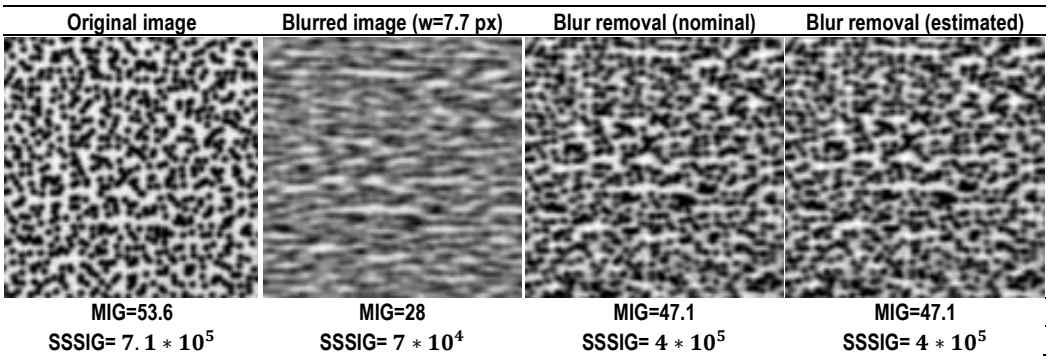

Figure 29 Compensation results for Case 1 (w=7.7 px and a=3.35 px)

4.2.2 Case 2: 'Sample 3b' from DIC challenge

From Figure 30 to Figure 32, the compensation results are shown for different blurred images, when sinc function is defined either with nominal or with estimated values (coming from Sinc fitting) of motion blur.

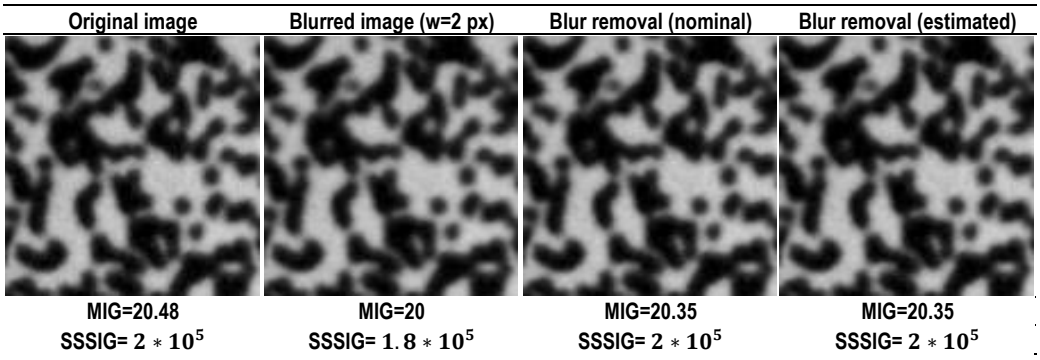

Figure 30 Compensation results for Case 2 (w=2 px and a=1 px)

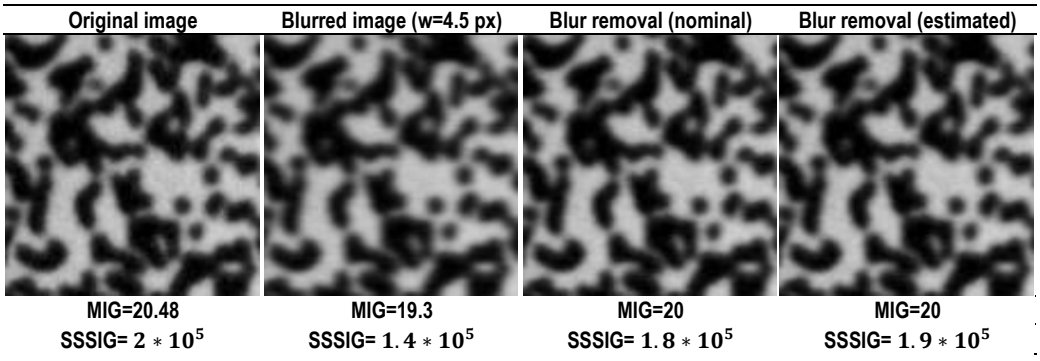

Figure 31 Compensation results for Case 2 (w=4.5 px and a=2.25 px)

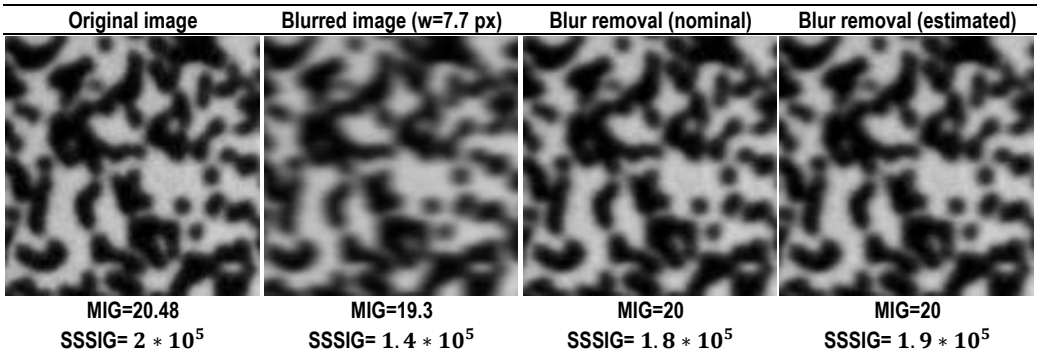

Figure 32 Compensation results for Case 2 (w=7.7 px and a=3.35 px)

4.2.3 Case 3: 'Sample 7' from DIC challenge

From Figure 33 to Figure 35, the compensation results are shown for different blurred images, when sinc function is defined either with nominal or with estimated values (coming from Sinc fitting) of motion blur.

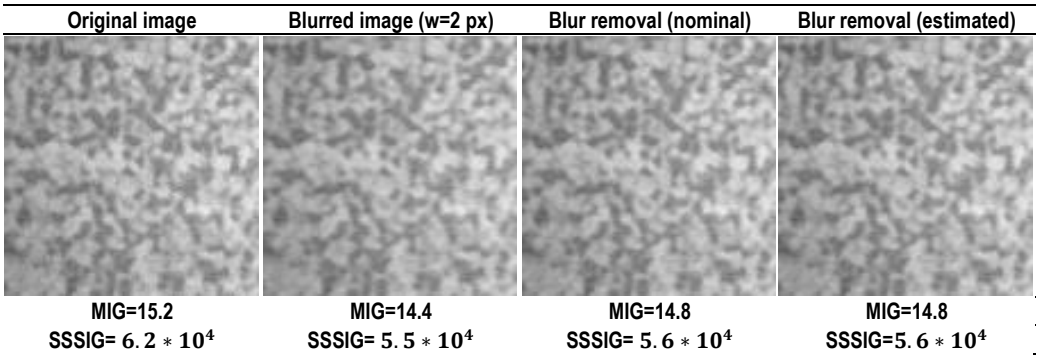

Figure 33 Compensation results for Case 3 (w=2 px and a=1 px)

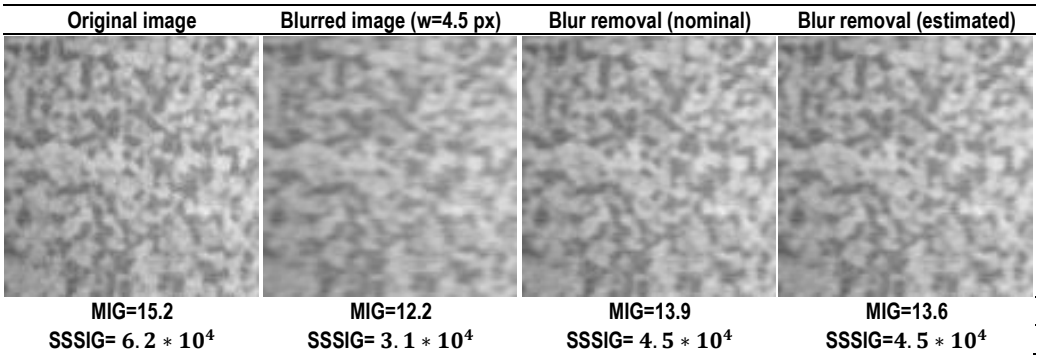

Figure 34 Compensation results for Case 3 (w=4.5 px and a=2.25 px)

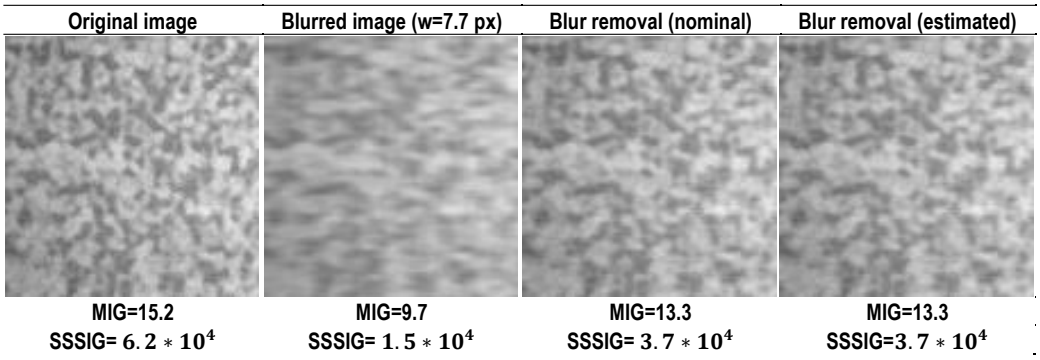

Figure 35 Compensation results for Case 3 (w=7.7 px and a=3.35 px)

4.3 Comparison and results

From a preliminary observation of figures from Figure 27 to Figure 35, the deblurred images seem to be very similar to the reference ones and it is always possible to distinguish speckles or small characters. So, the following considerations can be done:

- Motion blur is successfully removed for all the tested values of blur (w=2, 4.5, 7.7 px).
- Motion blur is successfully removed independently on the considered image type.
- The deblurring algorithm operates well both for nominal and estimated values, confirming that the estimation error found earlier is negligible.

For a quantitative analysis, the mean intensity gradient (MIG) and the sum of square of subset intensity gradient (SSSIG), already presented in section 1.4.1, were calculated for each image. The results clearly highlight that the values of both MIG and SSSIG drop proportionally to the increase of *w*, testifying that motion blur caused pattern degradation. After image restoration, the two indexes approach the values of the reference static images, meaning that an improvement in the image quality has been done.
However, to validate the blur compensation technique, a further analysis seems to be necessary. Thus, a good option is to compare the intensity profile of the same row in the reference image, blurred image and the restored one for the three image patterns. The case with w=7.7 px and a=3.35 px is selected to understand if the deblurring is able to reconstruct the image even in the worst conditions, namely when blur was high (Figure 36). Pay attention that the algorithm operates with images in double format, so the pixel brightness values are scaled between 0 and 1.

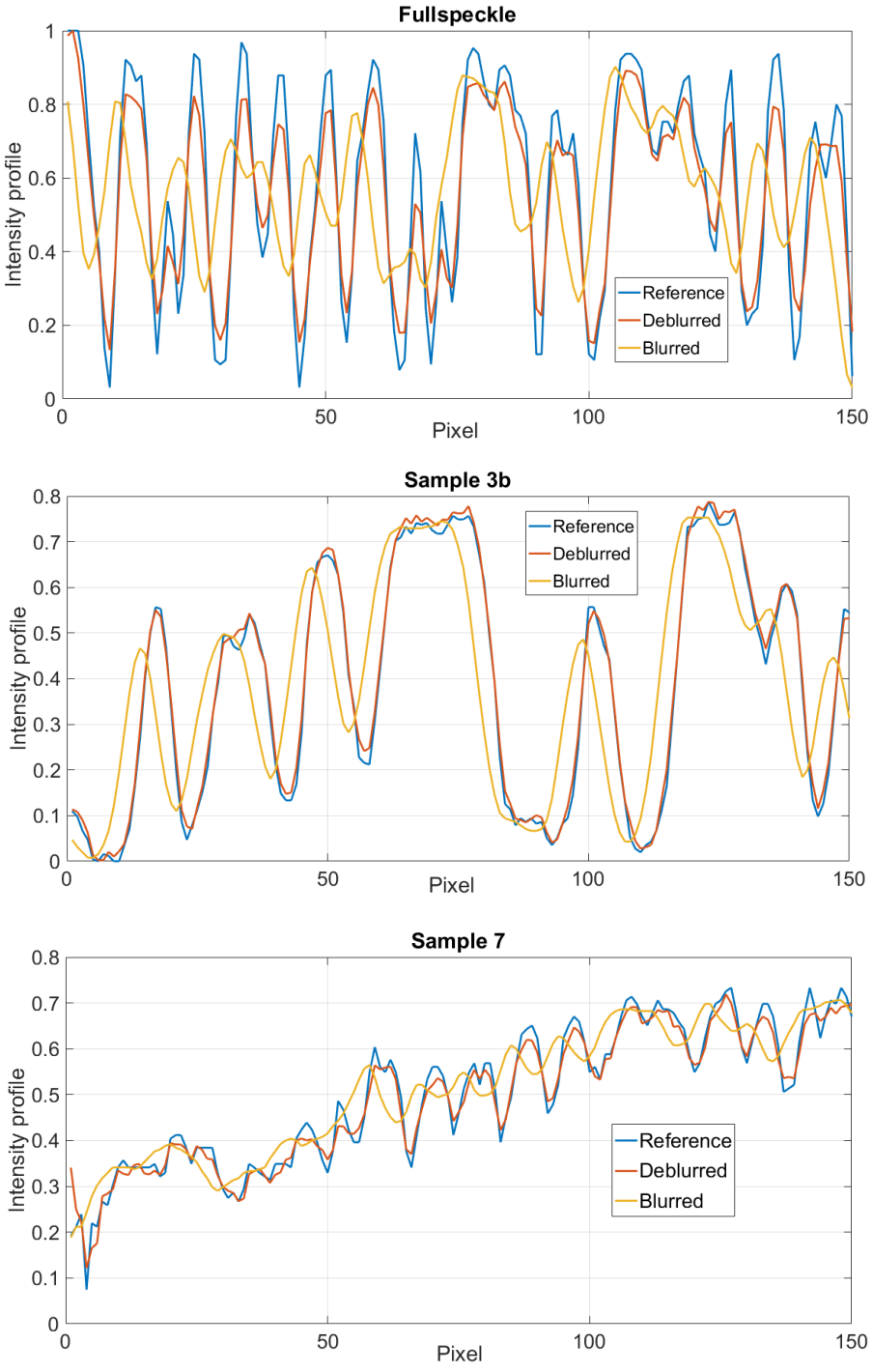

Figure 36 Row brightness profile before and after deblurring with estimated parameters, applied on blurred images with w=7.7 px and a=3.35 px

Positive confirmations are achieved from the above figure, since the row profile after the restoration process becomes very similar to the one of the reference image, meaning that the change in brightness caused by blurring is almost compensated.

4.4 Influence of noise

It has been seen from section 3.4.1 that noise plays a negative role in the blur estimation. The same could occur during blur removal. To study the noise influence in the restoring process, the three blurred images adopted in the previous section are chosen (with w=7.7 px and a=3.35 px), then Gaussian noise level2 is added. This specific choice is justified by the fact that we want to put the algorithm into a critical condition, where both high blur and noise are present. Then, the deblurring with nominal and estimated blur parameters is performed. The results appear in Figure 37.

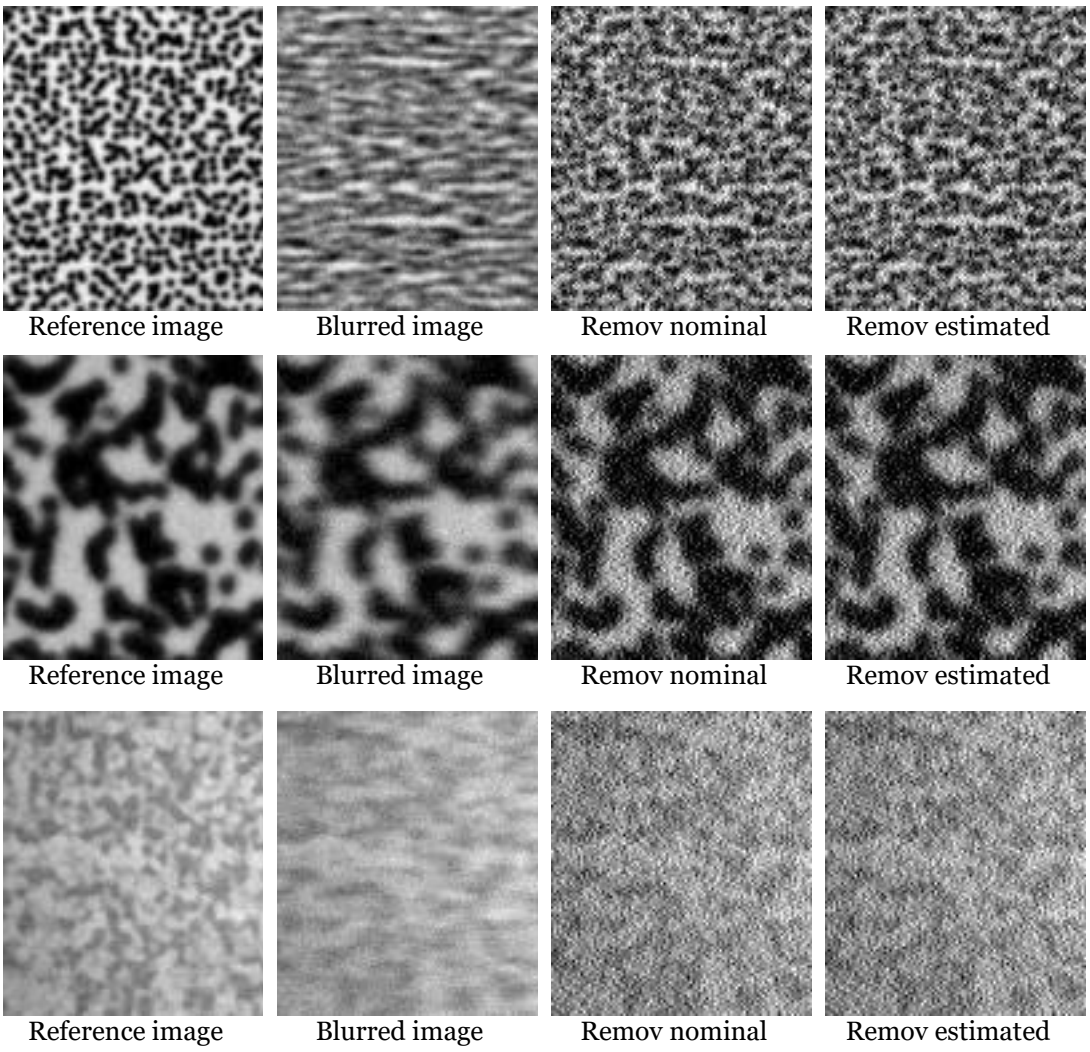

Figure 37 Compensation results for Case 1, 2, 3 (w=7.7 px and a=3.35 px) in presence of noise

The image deterioration after the deblurring process is quite evident, even though there is a partial removal of motion blur. For a detailed examination, the same procedure adopted in section 4.3 is repeated there, reporting in Figure 38 the row profile before and after deconvolution for each type of pattern.

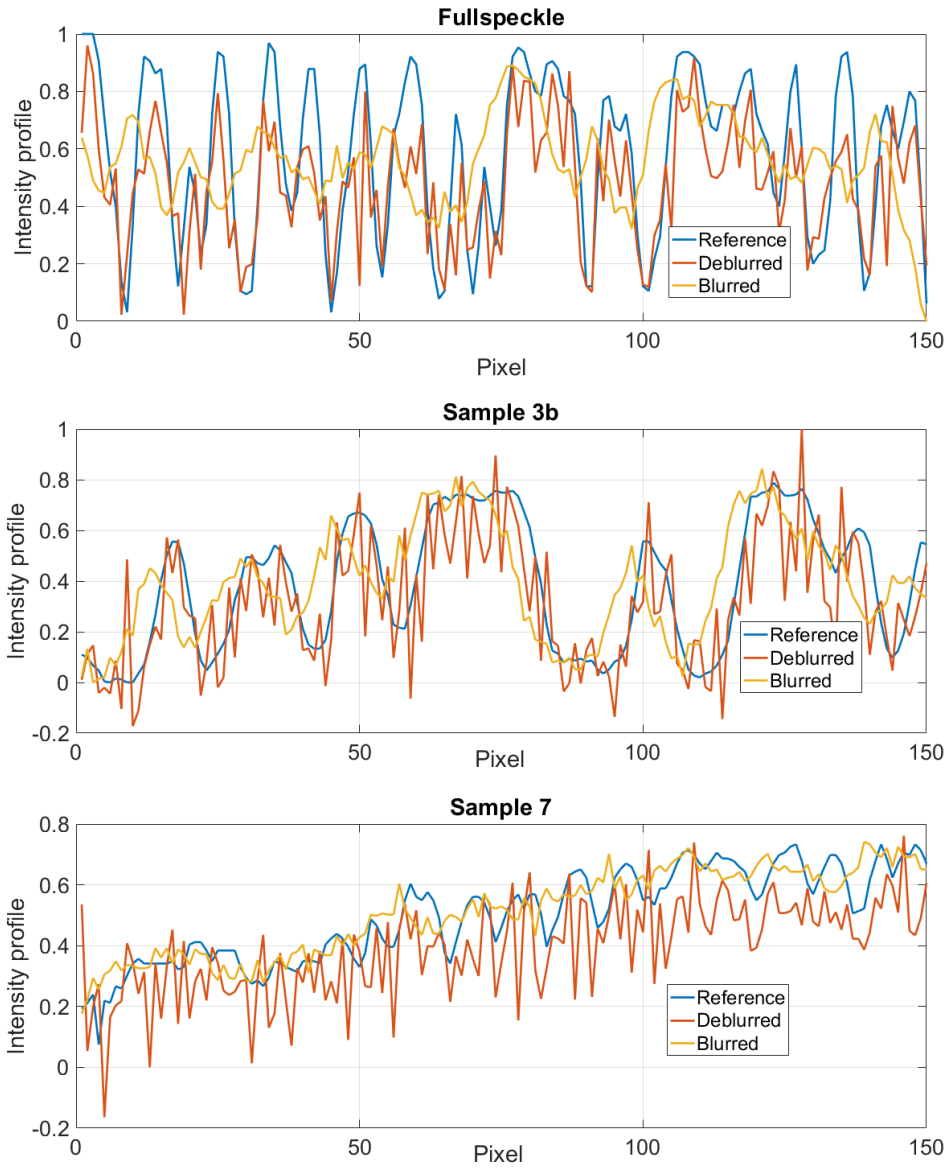

Figure 38 Row brightness profile before and after deblurring with estimated parameters, applied on blurred images with w=7.7 px, a=3.35 px and noise level2

The graph exhibits that, in presence of noise, the row profile after deconvolution is worsened, meaning that the deblurring is no more able to restore the images effectively.

Very bad results are achieved in case of 'Sample 7'. This situation can be reconnected to the same phenomenon that was happened during the estimation process (Figure 23). The combination of elevated level of noise and low contrast in the image becomes critical either for estimation through Sinc fitting or for deblurring.
It is possible to conclude that the blur removal algorithm does not reach satisfying performances if applied on images corrupted by relevant quantity of noise.

4.5 Deconvolution with Wiener filter

Moderate level of noise is always verified during actual image acquisition. Given that deconvolution in cepstrum domain does not reject the noise contribute, Wiener filter [98] is also considered as a viable solution to remove motion blur. In fact, both the Wiener causal filter and its finite impulse response (FIR) counterpart are optimal filters for the signal deconvolution in presence of additive noise.
To implement the inverse filter according to eq.(18), it is necessary to define in frequency domain both the convolution model $H(u,v)$ (i.e. the sinc function with blur parameters, named also Optical Transfer Function (OTF)) and the noise-to-signal ratio $NSR(u,v)$. It represents the ratio between the power spectral density of the noise $N(u,v)$ and the power spectral density of the original image $S(u,v)$.
However, to facilitate the operations, it is decided to use as support for Wiener deconvolution the function which is already implemented in Matlab ('*deconvwnr.m*').
It accepts as input the blurred image, the Point Spread Function (PSF) and the noise-to-signal ratio, returning as output the deblurred image.
The Point Spread Function (PSF) is the same of the OTF, but defined in space domain. It describes the degradation process (i.e. blurring) and it is simulated by the code generating a motion filter to the image, using the blur length and the blur direction specified by the user.
The Noise to Signal Ratio (NSR) is an index able to model the presence of uncorrelated noise into the image. The code allows to express the ratio either as a frequency distribution having the same size of the image ($N(u,v)/S(u,v)$), or as a scalar constant R which approximates the NSR in every point of frequency coordinates (u,v).

4.5.1 NSR definition

Since a correct definition of the NSR is crucial to achieve good deconvolution results [98], an algorithm able to estimate NSR with both the two admitted options has been developed, to understand which one is the most robust. A detailed explanation is reported.

To reproduce a real acquisition, a static reference image is selected, and the desired Gaussian noise level is added for a predefined number of times (k), obtaining new different images. The mean ($\bar{p}$) and the standard deviation (σ_p) between the k noisy images are calculated pixel by pixel, according to eq.(29), (30).

$$\bar{p} = \frac{1}{k}\sum_{i=1}^{k} p_i \tag{29}$$

$$\sigma_p = \sqrt{\frac{\sum_{i=1}^{k}(p_i - \bar{p})^2}{k}} \tag{30}$$

In this way, it is possible to assembly two matrices containing the mean and the standard deviation values for each i^{th} pixel of the image, respectively. The former can be used to find an estimation of the true signal present into the image, given by its power spectral density $S(u,v)$. To have a reliable index also for the image noise, the estimated noise variance (var_{estim}) is determined starting from the second matrix, as done in eq.(31).

$$var_{estim} = \frac{1}{MN}\sum_{i=1}^{M}\sum_{j=1}^{N} {\sigma_{p\,i,j}}^2 \tag{31}$$

Where M and N are the numbers of rows and columns of the image.
Now, a matrix with the same image dimensions is generated, containing Gaussian noise with zero mean and variance equal to var_{estim}. Its power spectral density represents an index for the image noise in frequency domain $N(u,v)$.
The second option proposes the NSR as a "mean" scalar constant through the overall frequency distribution. Let us introduce two quantities, defined as the average noise power n_a and the average signal power s_a, such that $R = n_a/s_a$ stands for the NSR estimation.

$$n_a = \frac{1}{MN}\sum_{u}\sum_{v} N(u,v) \tag{32}$$

$$s_a = \frac{1}{MN}\sum_{u}\sum_{v} S(u,v) \tag{33}$$

Once modelled the NSR according to the two methods, the Wiener filter engine is applied on some reference cases and comparisons are made. In Figure 39, it is reported as demonstration

the deblurring results for a portion of an image having realistic DIC pattern ('Fullspeckle'), blur length equal to 4 px and Gaussian noise level2.

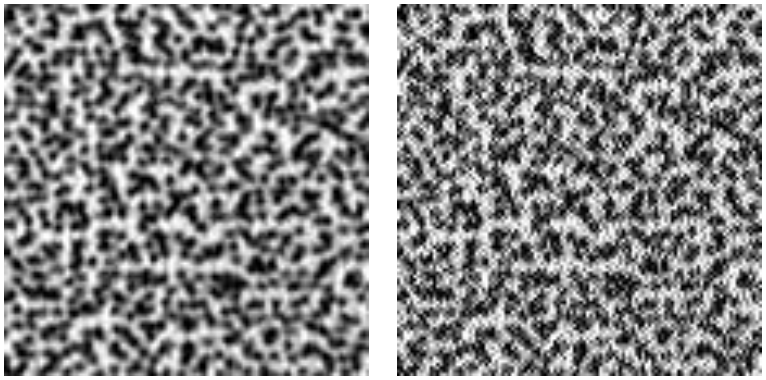

(a) (b)

Figure 39 Outcomes from Wiener filter application using two distinct NSR definitions

When NSR is defined as constant scalar value (b), new artefacts appear in the restored image. These new elements are a natural output of the Wiener filter every time the NSR does not match exactly the actual noise distribution of the reference image. In this case, by modelling the noise as constant with frequency, a quite relevant approximation has been introduced. In fact, it is well known in imaging [99] that there are several kinds of noise and most of them come with a peculiar spectrum. Therefore, the correct representation for NSR is the frequency dependent one (a), which guarantees the best trade-off between level of details and presence of artefacts. From now on, this last definition will be used dealing with Wiener filter applications.

4.5.2 Applicative example of Wiener filter

Once all the necessary parameters are defined, the filtering operation is implemented on the same noisy images of section 4.4, to see if some improvements occur with respect to deblurring with cepstrum. In Figure 40, a final comparison between the restored images coming from the two deconvolution techniques is reported.

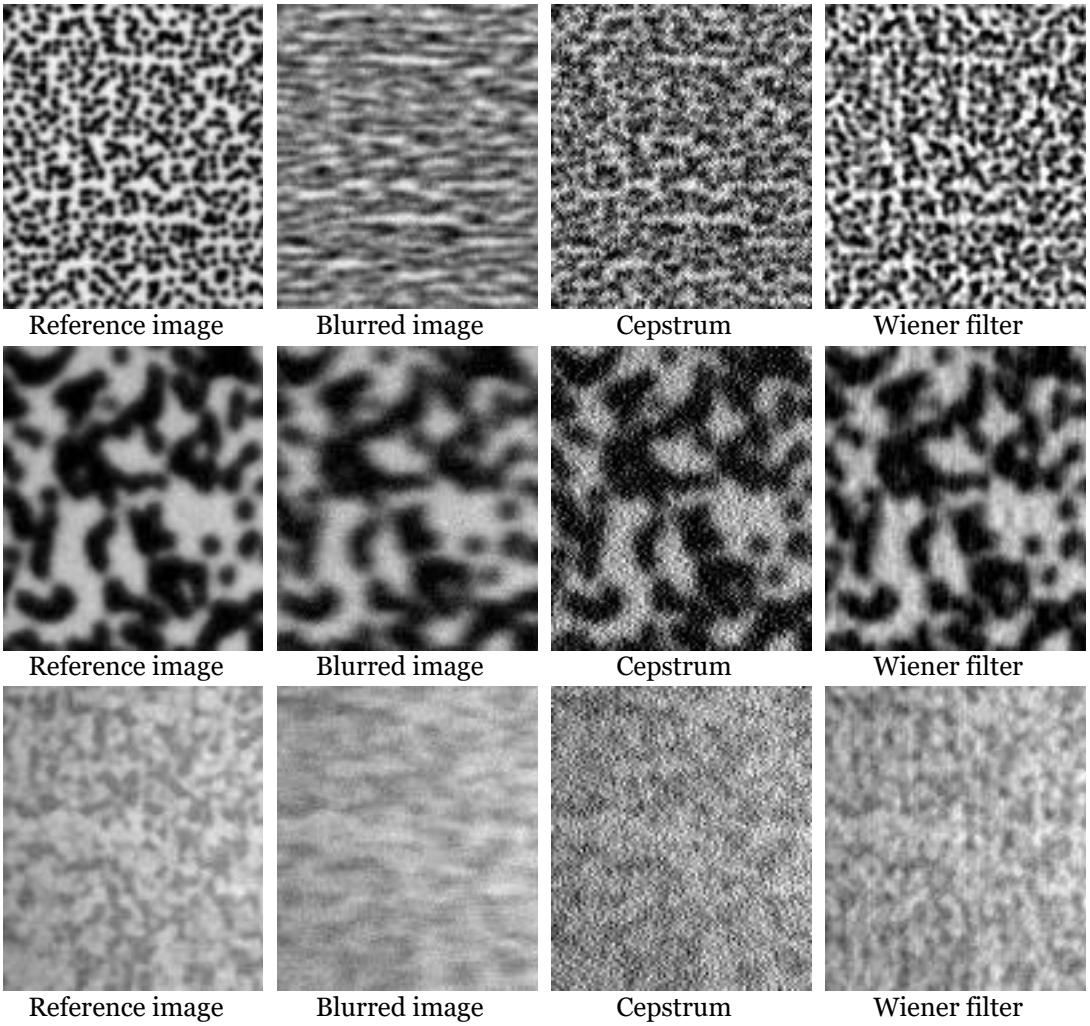

Figure 40 Comparison of results coming from cepstrum-based deconvolution (c) vs Wiener deconvolution (d), using estimated blur parameters

It can be claimed that cepstrum-based deconvolution for blur removal is very effective in absence of noise. At the same time, it becomes very sensitive as the noise level increases, returning compensated images with significant artefacts. Wiener filter, on the contrary, generates artefact-free images even in the case of noisy images, provided that the OTF and the SNR are correctly estimated.

Before concluding this chapter, it seems appropriate to remind that all the methods using spectral analysis for noise modelling and rejection have a major limitation: they work properly as long as the noise is a linear and additive stochastic process. Let us consider the case of a digital acquisition involving vision systems. The CMOS sensors mounted inside the cameras are afflicted by a phenomenon called “heteroscedastic noise”. The peculiar characteristic of

such a type of noise is that its variance is directly proportional to the pixel brightness, meaning that the noise is not linear, but strictly dependent from the signal itself. Accordingly, the approach described above for the SNR estimation must be considered with added caution passing to the case of real acquired images.

CHAPTER 5
BLUR COMPENSATION FOR DIC UNCERTAINTY REDUCTION

In this chapter the innovative approach to mitigate the effects of motion blur on 2-D digital image correlation (DIC) measurements is presented. DIC uncertainty is composed by a correlation bias (namely bias error) and a random error, that generates dispersion in the measured displacement [36]. In the context of DIC, uncertainty analysis is often carried out by means of synthetic experiments [100], where image transformations are numerically imposed. Therefore, DIC analysis on images with numerically imposed motion blur is carried out. Then, the effect of adding noise to this group of images is investigated. Finally, the blurred images are compensated using the two deconvolution techniques presented in the previous chapter, to understand if blur removal can improve DIC performances, especially in terms of measurement uncertainty reduction.

5.1 DIC analysis on images with motion effect

In the current study *Ncorr* software [101] is used to perform DIC analysis. The three reference image groups involved in chapters 3 and 4 are examined, having imposed motion effect and imposed shift equal to half of the blur length. In [53], it was demonstrated that the uncertainty of result mainly depends on the motion blur, while the imposed shifting value had a negligible effect. In order to perform an efficient analysis and maintain the same subset parameters for all the patterns (Table 2), it has been possible to consider only images having $w \leq 5.5$ px, because the risk of decorrelation for DIC grew significantly when $w>5.5$ px, returning inconsistent results.

Table 2 Parameters for Ncorr DIC analysis

Reference image	Size (px)	Subset radius (px)	Subset spacing (px)
Realistic DIC specke	291 x 291	35	3
Sample 3b	511 x 511	35	3
Sample 7	487 x 325	35	3

DIC analysis was done on images at increasing levels of motion blur, always using the original (still) image as reference. DIC process returns the displacement of each subset in which the image has been divided by the software. The displacement matrices obtained for each image are used to calculate both the bias error in mean displacement and the standard deviation of displacement estimated by DIC (Figure 41). Since motion effect has been applied along the horizontal direction, the reference displacement has been set equal to the imposed shift $w/2$ in the horizontal direction.

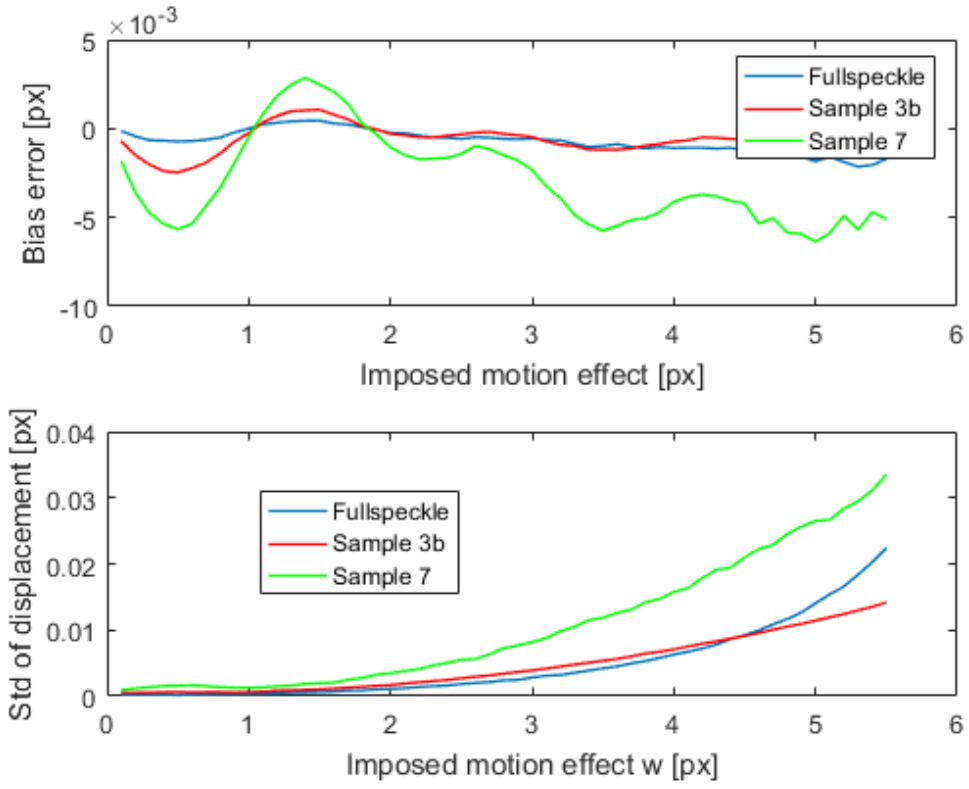

Figure 41 Bias error and standard deviation of displacement in presence of blur and rigid motion for the three reference images

As displayed in the above figure, the standard deviation of the displacement field u_e is at least one order of magnitude bigger than the corresponding bias error in mean displacement. This demonstrates that u_e can be considered a solid indicator of measurement uncertainty.

Moreover, u_e is the most meaningful quantity in the description of motion blur phenomena since it grows as faster as w increases.

5.1.1 Effect of adding Gaussian noise to images with motion blur

In this section the two levels of Gaussian noise already presented (having standard deviation equal to 2% and 8% of 255, respectively) are added to the previous images before running the DIC analysis, to check if somewhat changes in the behaviour of displacement and uncertainty.

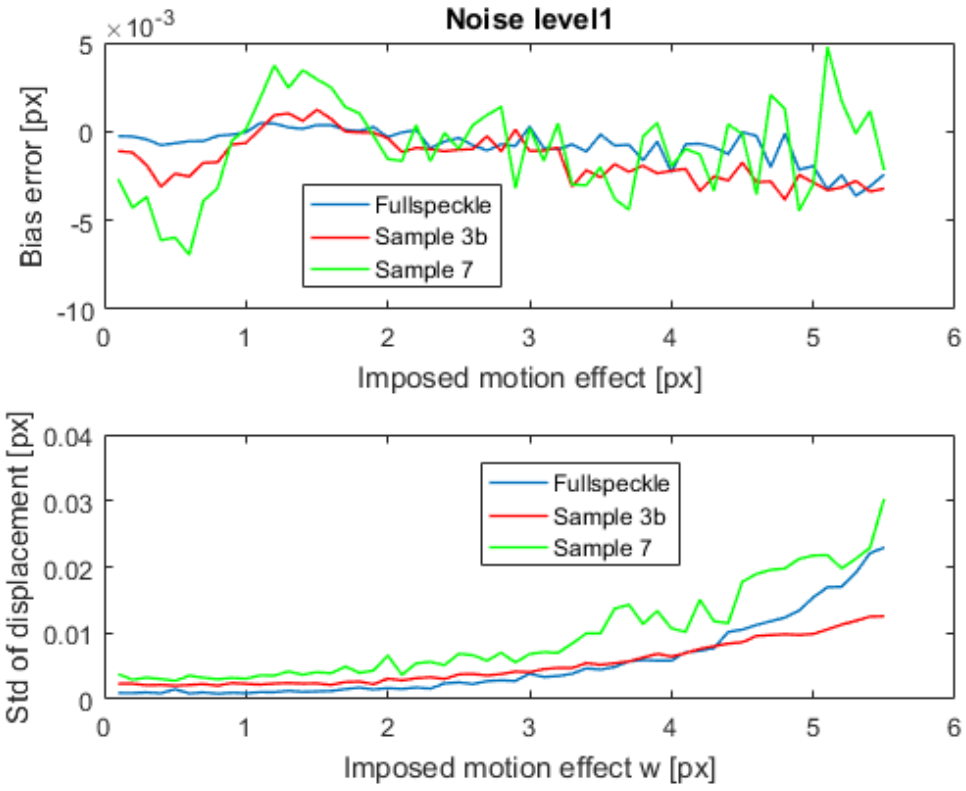

Figure 42 Bias error and standard deviation of displacement in presence of blur and rigid motion after adding noise level1

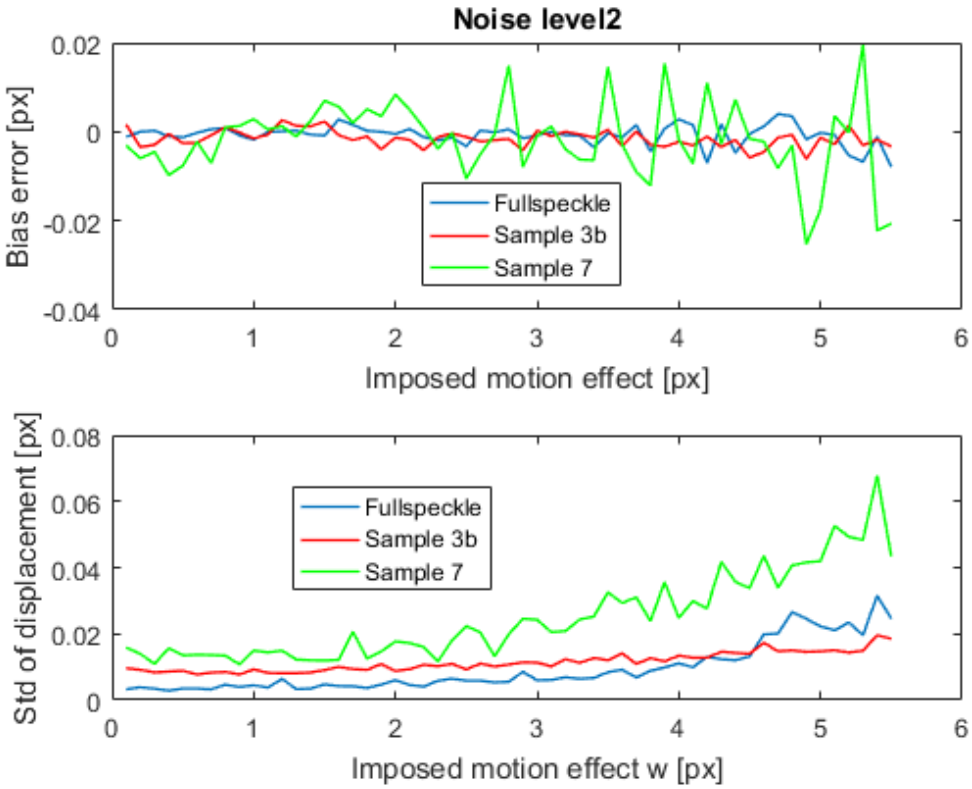

Figure 43 Bias and standard deviation of displacement in presence of blur and rigid motion after adding noise level2

Note that in the analysed motion blur range ($w \leq 5.5\ px$) the bias and the standard deviation of displacement are quite similar in Figure 41 (no noise) and Figure 42, Figure 43 (added noise). This justify that, although Gaussian noise affects both the bias and the random error, the blurring due to motion increases the uncertainty much more than the noise. Once again, the standard deviation of displacement remains one order of magnitude higher than the corresponding bias for all the image types. From now on, only the trend of standard deviation will be displayed as the meaningful quantity of interest for the dissertation.

5.2 DIC uncertainty after blur compensation using complex cepstrum

As just demonstrated, DIC measurements suffer motion blur. The uncertainty is increased, and the reconstruction of displacement field is less accurate. In this section the compensation of such a phenomenon is tested using synthetic experiments. In the next two sections the

restored images obtained from the techniques presented in chapter 4 (i.e. cepstrum-based and Wiener filter) are analysed, to see if blur removal can improve the DIC performances.
Since the deblurring using cepstrum is not robust in case of images containing relevant quantities of uncorrelated noise, the blurred, noiseless image groups are considered to apply cepstrum deconvolution, using both nominal and estimated blur parameters. DIC analysis is performed on the restored images, whose results (in terms of standard deviation of displacement) appear in Figure 44.

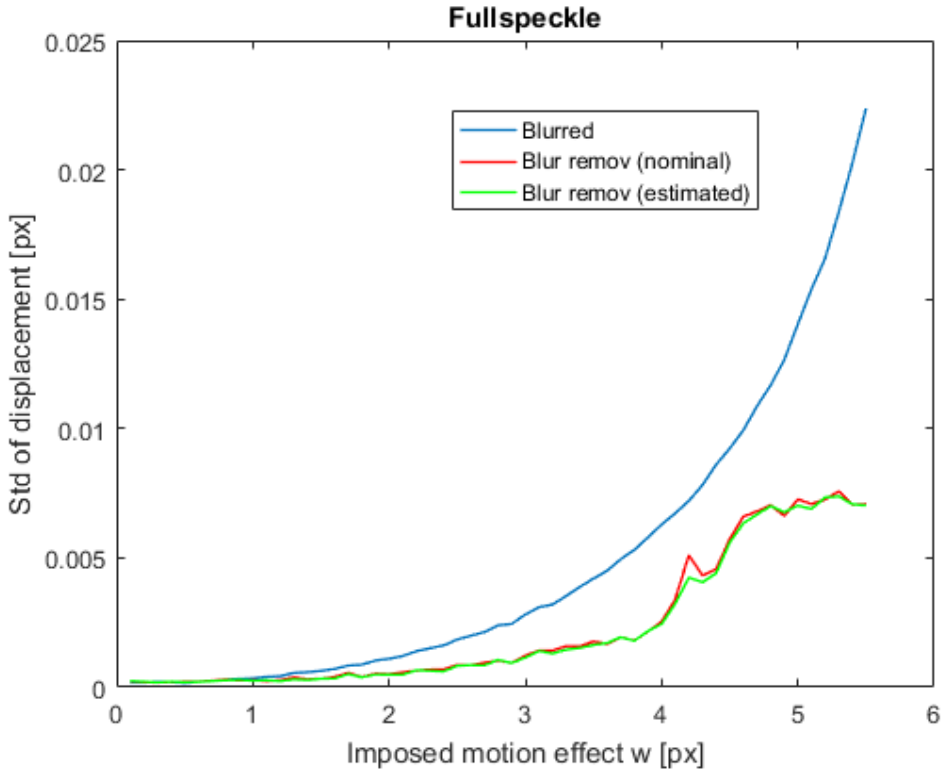

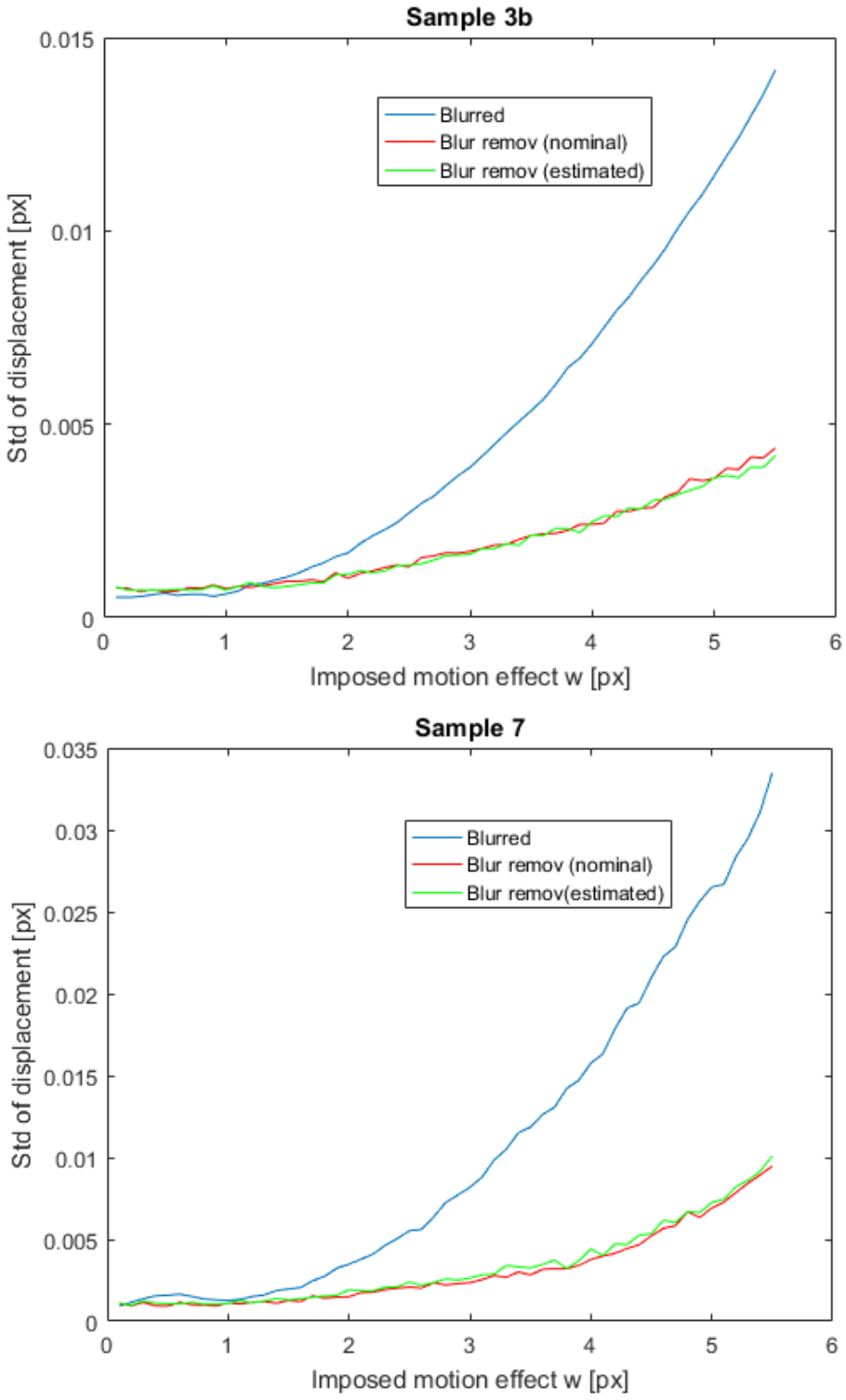

Figure 44 Standard deviation of displacement before and after blur compensation with cepstrum for the three reference image groups

By observing the trend of standard deviation for all the reference image types, it is possible to highlight some interesting features:

- the three curves become steeper as blur increases, testifying that blur is a relevant source for DIC uncertainty.
- The trend of uncertainty increase is different for distinct types of pattern.
- The maximum uncertainty value (corresponding to the point of the curves with maximum blur) is affected by the speckle type.
- After blur compensation with nominal (red line) and estimated (green line) blur parameters, the standard deviation strongly reduces, especially when blur becomes more intense (w>3 px). Such a behaviour is expected since other sources of random error exist in DIC processing (i.e. interpolation error, local luminance shift…), so the share of uncertainty reduction due to motion blur compensation decreases with *w*.

These considerations demonstrate that the proposed technique can significantly improve the accuracy of DIC (i.e. reduces the standard deviation of displacements) by means of motion blur compensation. However, the field of applicability is limited to noiseless images.
From the preceding comments, it has been found that motion blur and image pattern assume a significant role in the uncertainty behaviour. It would be useful to examine this aspect. Figure 45 illustrates portions of the preceding blurred images with an increasing motion effect, where pattern degradation becomes quite evident. For a quantitative analysis of pattern quality, the mean intensity gradient (MIG) and the sum of square of subset intensity gradient (SSSIG) are recalled.

Original image	W=2 px	W=3 px	W=4 px	W=5.5 px
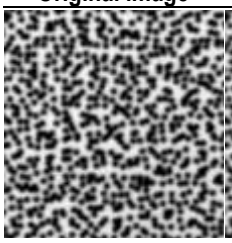	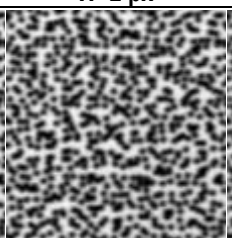	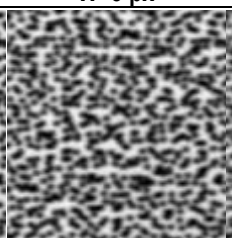	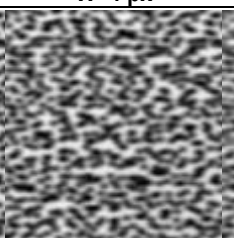	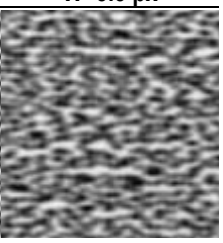
MIG=52.2	MIG=46.8	MIG=41.8	MIG=36.8	MIG=30.8
SSSIG= $7.1 * 10^5$	SSSIG= $4.9 * 10^5$	SSSIG= $3.4 * 10^5$	SSSIG= $2.1 * 10^5$	SSSIG= $1.1 * 10^5$

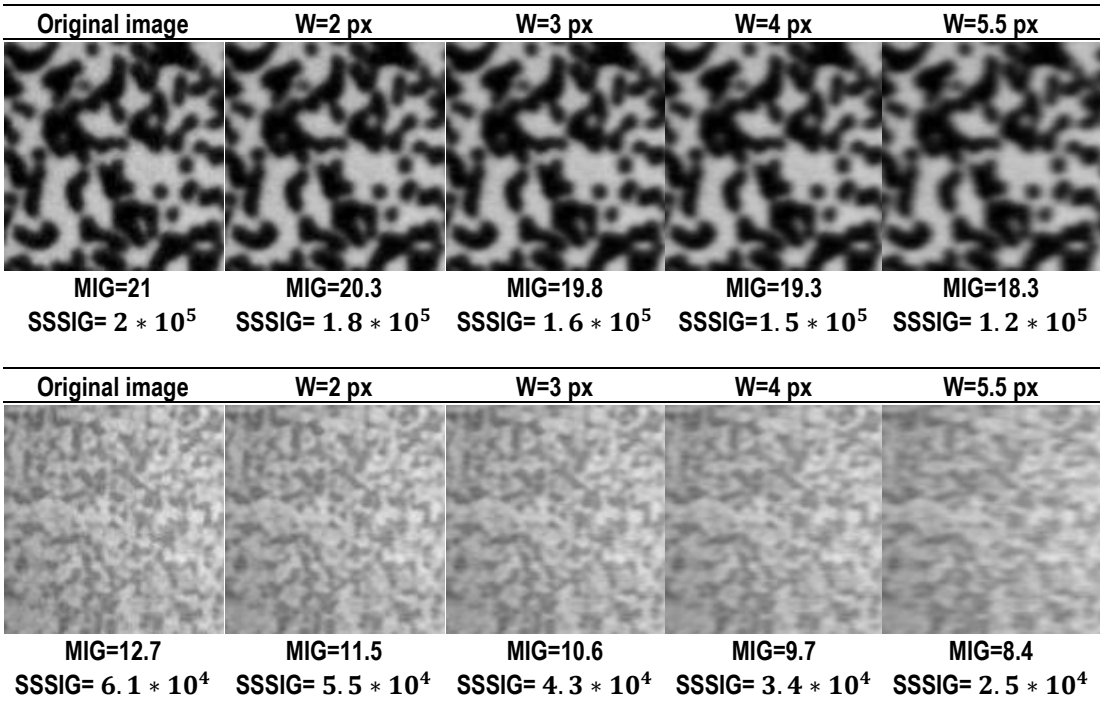

Figure 45 Portions of tested images with increasing motion effect (w) with the corresponding mean intensity gradient (MIG) and the sum of square of subset intensity gradient (SSSIG)

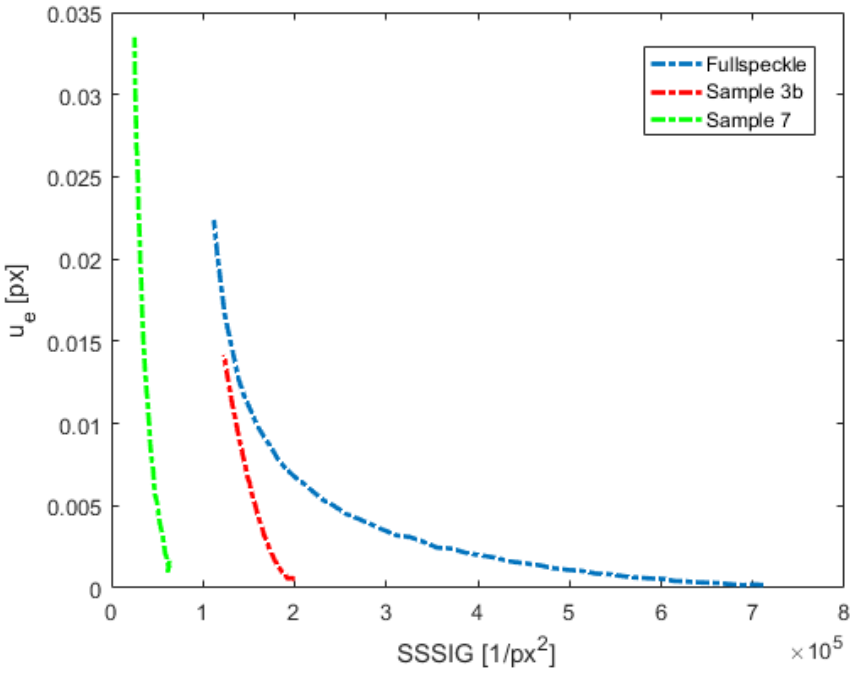

Figure 46 Dependence SSSIG-u_e

By increasing motion blur, MIG and SSSIG values drop independently on pattern type, showing that the expected uncertainty u_e grows. This is confirmed also by the previous DIC analysis.

Instead, the trend of MIG and SSSIG reduction (passing from the original image to the one having the maximum motion effect) is different for each pattern (Figure 46). To better understand the reasons of such a behaviour, it is necessary to make some considerations.

In eq.(14), motion blur has been modelled in frequency domain as a sinc function having zeros at each $1/w$, where w represents the blur length in pixels. Due to convolution theorem, the product between the spectrum of the original image and the sinc function results in the spectrum of the blurred image.

Since the frequency content strongly depends by the image type, the pattern owning the spectrum with the highest frequency components will be filtered in a more significative way by the sinc, even for low blur values, where zero-crossing occurs later. As demonstration, in Figure 47 (a) the averaged spectra of the considered reference image types are reported. As can be seen, the realistic DIC speckle ('Fullspeckle') is the pattern with the highest frequency content. For this specific situation, Figure 47 (b) shows that the effect of sinc filtering becomes relevant even when blur is small (i.e. w=2 px), modifying the spectrum of the blurred image and, consequently, the characteristics of the blurred image itself. This justifies why MIG reduction, which is synonymous of pattern degradation, is more accentuated for the first image type.

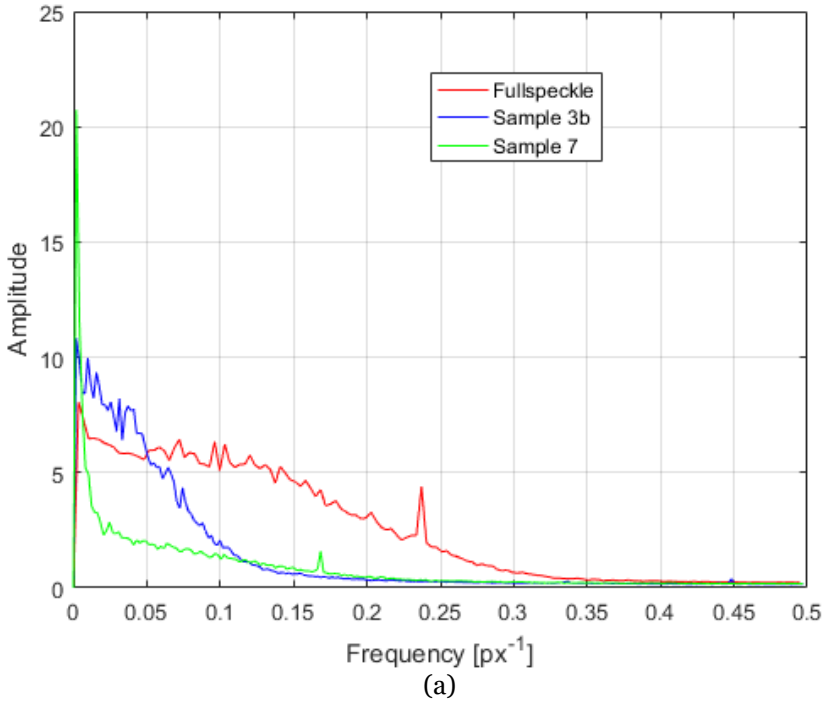

(a)

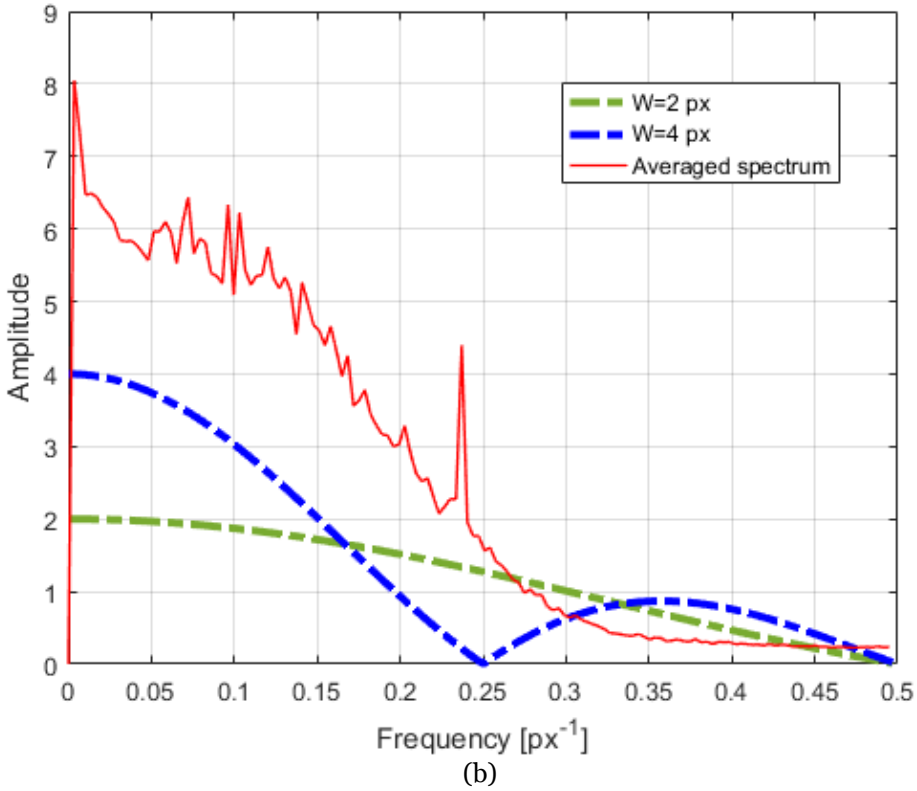

(b)

Figure 47 Averaged spectra of the three reference cases (a) and effect of different blurring condition on image spectrum (b)

5.3 DIC uncertainty after blur compensation using Wiener filter

The purpose of this section is to evaluate the improvement of DIC performances after the deblurring of images corrupted by both motion blur and noise.

As seen in chapter 4, Wiener filter is the preferential restoring technique in presence of additive noise. Thanks to the knowledge of nominal/estimated blur length, blur direction and NSR distribution, it is possible to correctly apply the filtering given a certain blurred image. Wiener filter is adopted on the same classes of blurred images of section 5.1.1, with the addition of Gaussian noise level1 (having zero mean and standard deviation equal to 2% of the dynamic range), to simulate a realistic digital acquisition with moderate noise.

The results in terms of standard deviation of displacement in horizontal direction are reported in Figure 48.

It should be noted that it is possible to perform the deblurring only on images having motion blur values greater than 1 px, because convolution processes under the sampling length of a digital signal are indeed ill-posed. In fact, given a generic sequence $x(k)$ and a generic convolution window $y(k)$, the convolution product $x(k) * y(k)$ is correctly defined for convolution windows greater or equal than the unit sample.

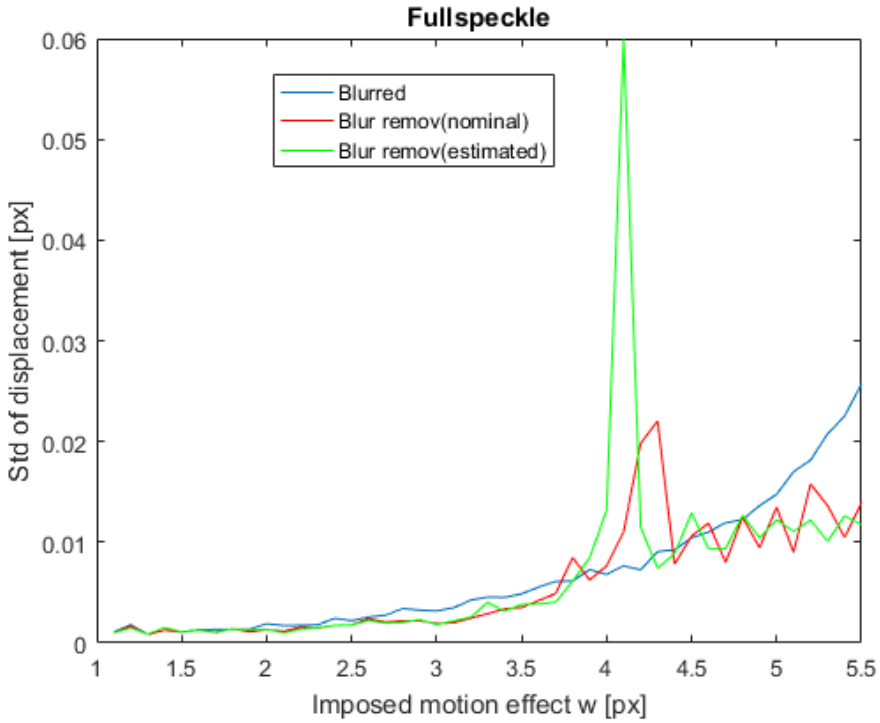

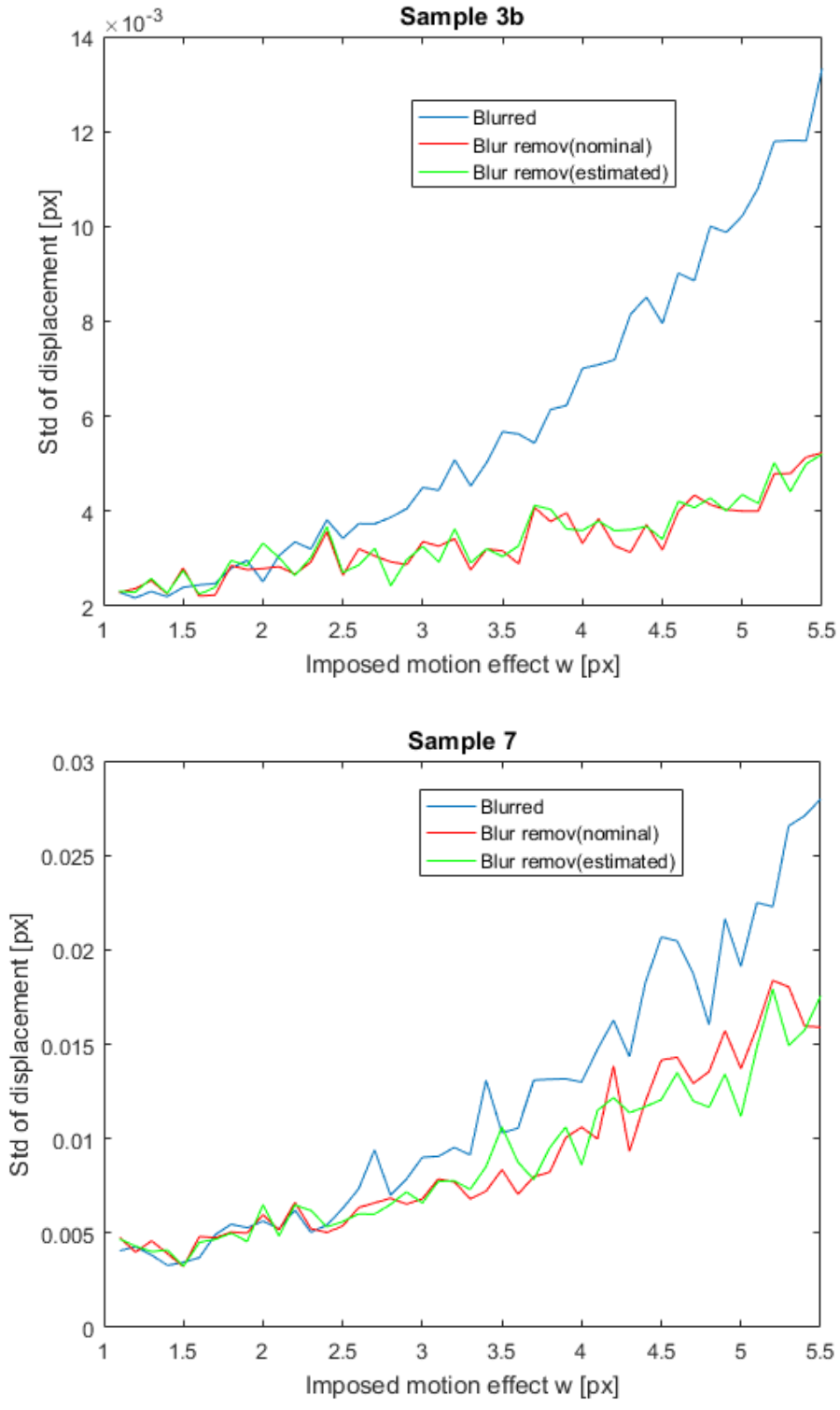

Figure 48 Standard deviation of displacement before and after blur compensation with Wiener filter for the three reference image groups corrupted with Gaussian noise level1

Also in this case, by observing the trend of standard deviation coming from DIC, it is possible to remark some key features:

- As already noted in section 5.1.1, the trend of standard deviation in blurred images is slightly modified by the presence of noise. The main source of uncertainty remains the motion blur.
- After blur compensation with nominal (red line) and estimated (green line) blur parameters, standard deviation reduces, although in a less evident way than in the case of noiseless cepstrum deconvolution. This is expected, since deconvolution compensates for the motion blur contribute, but fluctuations due to noise remain.
- 'Sample 3b' and 'Sample 7' are characterized by a better improvement in the trend of uncertainty after blur compensation with respect to 'Fullspeckle'. The reason is that non-optimal speckle patterns suffer badly the exhogenous effects (wheter they are noise or motion blur). So, the generic uncertainty rejection procedure is more effective on non-optimal patterns.

Moreover, an unusual situation after blur removal happens in the 'Fullspeckle' pattern, where a sudden increase of standard deviation occurs in the range between 4-4.5 pixel.
To understand the phenomenon, one should consider that regular DIC patterns are realized starting from a regular grid, with predefined speckles diameter and on-center spacing. The latter is then randomized with a chosen level of variability. The nominal on-center spacing of 'Fullspeckle' pattern is 4.1 pixel, meaning that the harmonic content in the spectrum of the pattern will exhibit a peak close to the frequency $\frac{1}{4.1} px \cong 0.24\ px^{-1}$ (Figure 49).

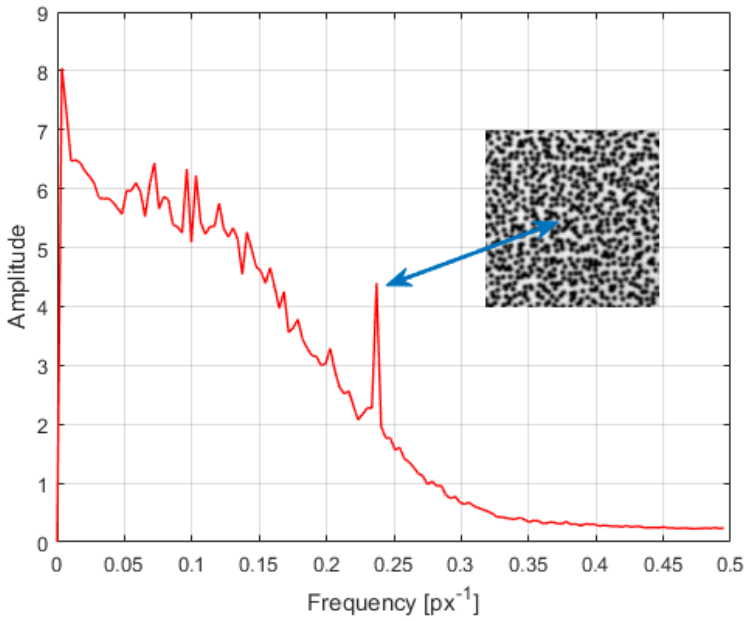

Figure 49 Peak in the image spectrum due to speckle spacing

Let us consider a blurred version of this pattern type, having a blur length which belongs to the critical range where uncertainty grows, i.e. w=4.1 px.

In frequency domain, the spectrum of an image with blur equal to 4.1 px is modelled as the product between the spectrum of the original static image and a sinc having the first zero at $\frac{1}{4.1} px^{-1}$. Similarly, motion blur compensation in frequency domain by means of Wiener filter corresponds to the point wise ratio between the spectrum of the blurred image and the sinc. In the neighbourhood of frequency $\frac{1}{4.1} \cong 0.24\ px^{-1}$, such ratio becomes huge, due to the fact that points of blurred image spectrum are divided by points close to the zero of the sinc (Figure 50 (a)). As consequence, Wiener filter is no more able to reconstruct the correct spectrum profile of the restored image and, passing to space domain, striations and artefacts will appear, as shown in Figure 50 (b). Since the artefacts are not present in the reference image, the correlation quality becomes poor. Indeed, this phenomenon boosts the displacement uncertainty in the range 4-4.5 pixel.

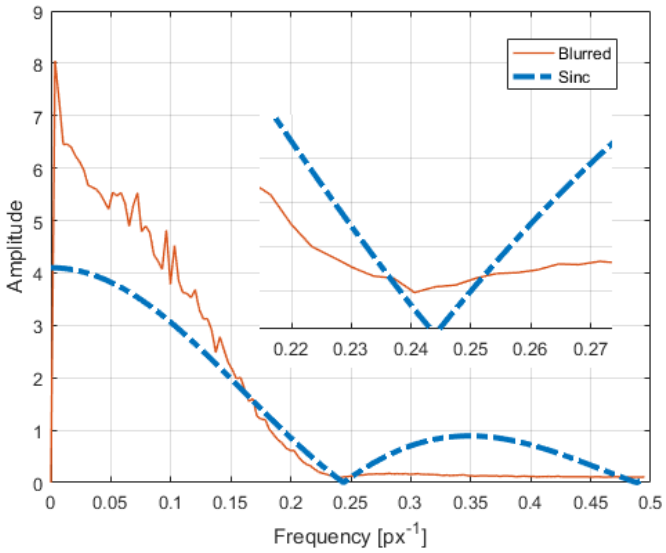

(a)

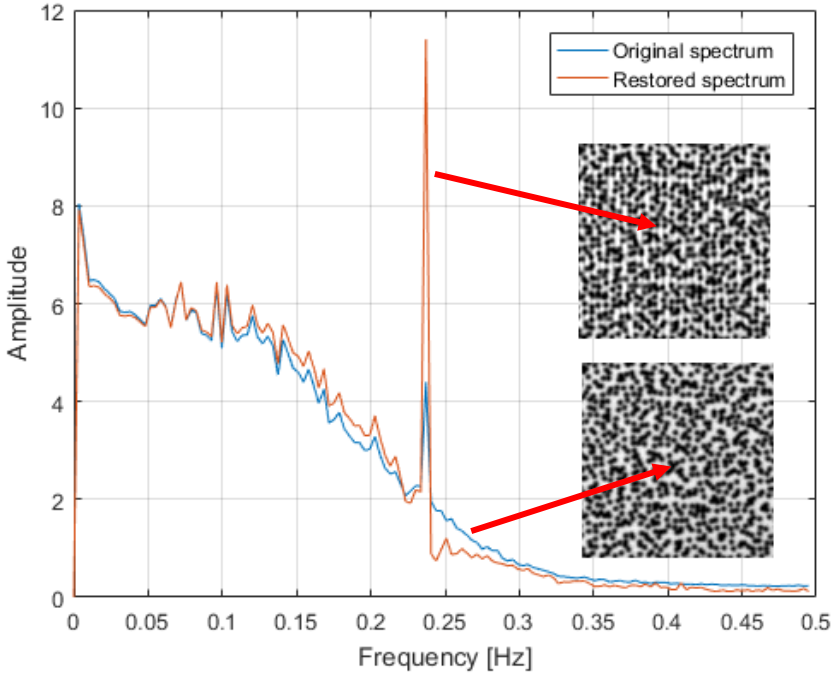

(b)

Figure 50 Deconvolution in frequency domain in case of realistic DIC pattern having blur equal to 4.1 px (a) and results in frequency and space domain after deblurring with Wiener filter (b)

CHAPTER 6
EXPERIMENTAL VALIDATION

Although the performance of the presented techniques (i.e. motion blur estimation and compensation) are proven to be acceptable in the case of numerically generated images, the principal issue is how they behave on images acquired in a real dynamic test. Therefore, a group of dedicated tests have been conducted and described in this chapter. The basic idea is to simulate a realistic dynamic application in which DIC measurements could be involved. The subject of the analysis is an aluminium bar, having U-notches in the middle and clamped at one extremity, submitted to an imposed sinusoidal vibration law through an electrodynamic shaker. Two distinct types of speckle patterns are attached on the planar surface of the beam to be tested and the target's motion is recorded by a high-speed camera. During the image processing activity, cepstrum-based algorithm is applied on the acquired images to estimate the motion blur values. Then, Wiener filter is adopted for the blur compensation. Finally, DIC analysis is performed on both blurred and deblurred images aiming to compare the behaviour of the DIC displacement uncertainty.

6.1 Experimental setup

It is of primary importance to develop a dedicated test bench able to fulfil the following requirements:

- Provide a dynamic vibrational motion with varying amplitude and frequencies
- Provide a reference measurement to be compared with the one coming from the vision system
- Being reliable and repeatable

To reach the desired goals, an LDS shaker is used to vertically vibrate the target at the desired frequencies and amplitudes, while the target's motion is recorded by a high-speed camera, equipped with a LED lighting system. The object accelerations are simultaneously measured by accelerometers, mounted on different beam positions. In the same way, the input acceleration, provided and controlled by shaker, is measured by an accelerometer. The experimental setup is shown in Figure 51, while its specifications appear in Table 3.

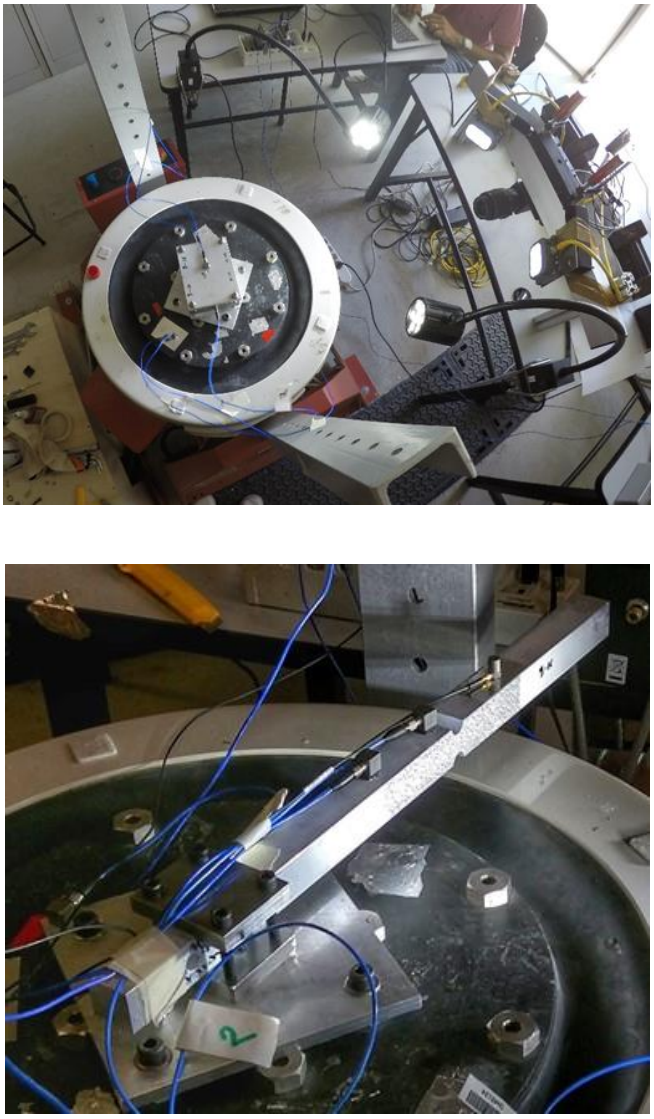

Figure 51 Experimental setup

Table 3 Setup specifications

Device	Brand and type	Technical data
Shaker	LDS V830	Max Freq = 3 kHz Max Mass = 12 kg Velocity sine peak = 2.0 m/s LMS Test Lab control
Accelerometers	PCB 333B30 (3)	Sensitivity: 100 mV/g ($\pm 10\%$) Measurement range: ± 50 g pk Frequency range:0.5 to 3000 Hz
	B&K 4516	Sensitivity: 100 mV/g ($\pm 10\%$) Measurement range: ± 500 g pk Frequency range:1 to 20000 Hz
Signal acquisition module	NI 9234	Signal ranges: $\pm$ 5 V 4 channels, BNC connectivity AC/DC coupling
High-speed camera	MotionBLITZ EoSens mini2	Sensor: CMOS, 1696 (H) x 1710 (V) pixel Pixel size: 8 x 8 µm with micro lenses Lens nominal focal length: 18 mm Image speed: up to 523 fps at full resolution, more than 200'000 fps at reduced resolution Shutter: from 2 µs to 1 s with 2 µs steps Recording time: 3 s at full resolution and full speed Amplification: Digital gain (1, 1.5, 2)

6.2 Dynamic characterization of the beam

The moving target used during the experiments is represented by a bar, which is clamped at one extremity in order to replicate a cantilever beam model. The bar has a square section, two U-notches in the middle and it is made of aluminium, whose mechanical and physical properties appear in Table 4.

Figure 52 Notched bar used in the experimental activity

Table 4 Mechanical and physical properties of Aluminium

Property	Value
Density	2,70 kg/dm^3
Yield tensile stress ($Rp_{0.2}$)	95 MPa
Ultimate tensile stress (UTS)	110 MPa
Poisson's ratio (ν)	0.34
Young's modulus (E)	70 GPa
Thermal conductivity (λ)	238 $W/(m \cdot K)$
Thermal expansion coefficient (α)	$23.5 * 10^{-6}\ K^{-1}$

A key issue before starting the tests is to select the appropriate excitation frequency to be applied on the system. Since exciting the target in resonance conditions (i.e. at a frequency equal to the natural ones) allows to produce larger displacements which can be recorded from the camera, the goal is to individuate the main natural frequencies of the cantilever beam.

The experimental evaluation of the dynamic response of the mechanical system requires the application of a dynamic force to the system itself. Since the main aim here is only to measure natural frequencies, the precision required for the FRF calculation is much less than when the measurements are to form the basis for a mathematical model or modal analysis (parameter identification). So, the adopted strategy is to impose as a shaker input signal a sweep excitation in the range between 20-3000 Hz, with a sweep rate of 2 octave/min and a closed loop control on input acceleration. The procedure provides also the use of two reference accelerometers, one mounted on the shaking table to measure the input acceleration (a_0) and the other mounted on the beam to measure the acceleration of the system (a_3), as reported in Figure 53.

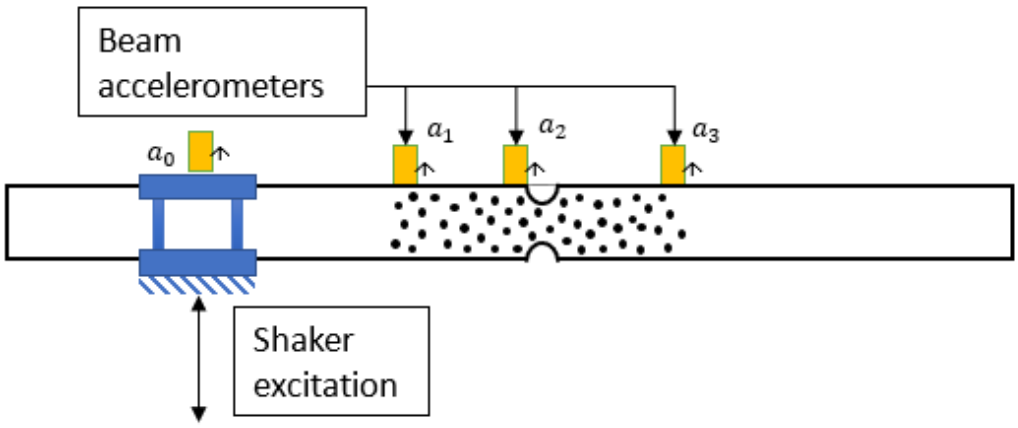

Figure 53 Accelerometers arrangement

The ratio between the spectrum of the beam response over the spectrum of the input acceleration allows to get the FRF of the mechanical system, which describes its dynamic behaviour in the frequency range of interest (Figure 54).

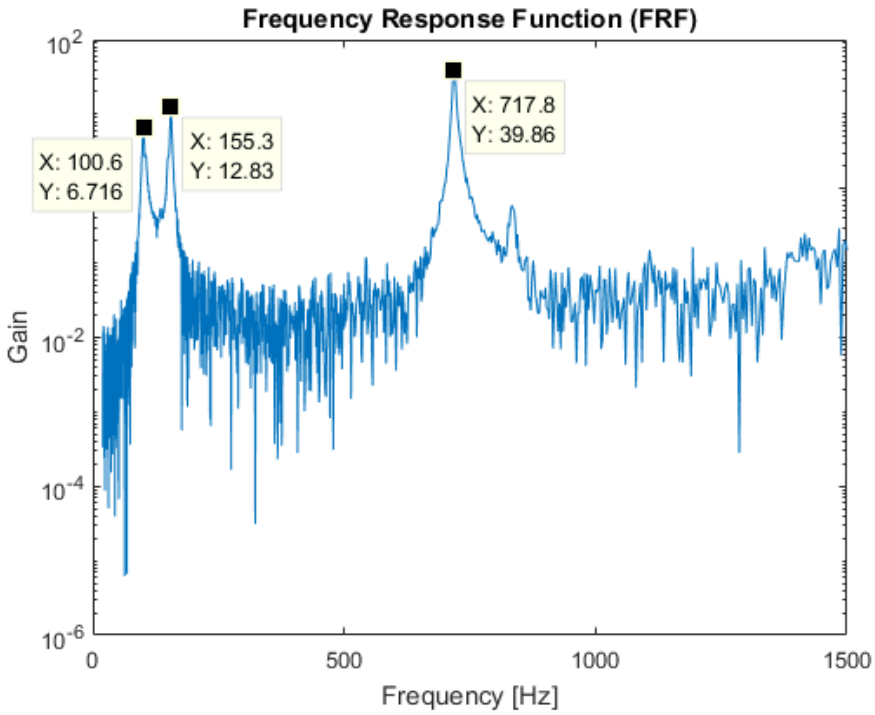

Figure 54 Frequency Response Function (FRF) of the cantilever beam

From the above figure it is possible to clearly distinguish the resonant peaks associated to the natural frequencies of the first three vibration modes. From the continuum system theory [102], it is known that the first mode is the one which generates the highest transversal displacement, dealing with a cantilever beam. For the purposes of this work, there is a need to obtain significant beam displacements, which imply the possibility for blur generation during the camera acquisition. Therefore, a sine wave having a frequency close to the first natural one (100 *Hz*) is used in the following tests, permitting to concentrate the whole excitation energy in a single frequency.

6.3 Speckle pattern realization

As explained in chapter 2, in digital image correlation technique the measurement surface must be characterized by a sufficient amount of information, i.e. variation in its colour intensity, in order to allow the algorithm to correctly retrieve displacements and deformations.

This is usually guaranteed by applying on the measurement surface an artificial random pattern ("speckle pattern"). The variety of specimen materials and sizes results in different technological approaches for the realization of the pattern itself.

Spray painting [3] is by far the most common technique for speckle pattern realization on medium size specimens (from few to some tenth of millimetres): a white paint is applied as background on the specimen and dark speckles are realized by mean of an airbrush. Tuning the viscosity of the ink, the opening of the nozzle and the spraying distance it is possible to vary the resulting speckle size, while the density of the speckles is controlled adjusting the spraying time. However, such a technique cannot allow a real control in the pattern realization, implying local areas characterized by low speckles density or, at the opposite, by too clustered blobs (Figure 55 (a)). At the same time, skilled users are required to perform the procedure and still the repeatability from one specimen to the other and the quality of the result are difficult to be guaranteed.

Therefore, an alternative technique for DIC pattern realization is adopted there, to provide an efficient, fast and flexible method for all material types, geometries and surface properties. It is based on the transfer of melted toner from a printed paper to the measurement surface.

At first, the speckle pattern is numerically designed on a calculator. Then, it is printed with a common laser printer on a paper used for tattoo making. The pattern is transferred by wetting and pressing the paper against the surface of the specimen. For a correct transfer of the toner, the surface must be smooth and clean, while for increasing pattern contrast and avoid reflections, a thin layer of white paint is sprayed as background on the object surface. Once a good adherence is achieved, the paper is removed, leaving the ink on the surface and achieving a result like the one of Figure 55 (b). The high quality of the obtained speckle pattern is clearly visible in terms of image contrast, pattern details and uniformity.

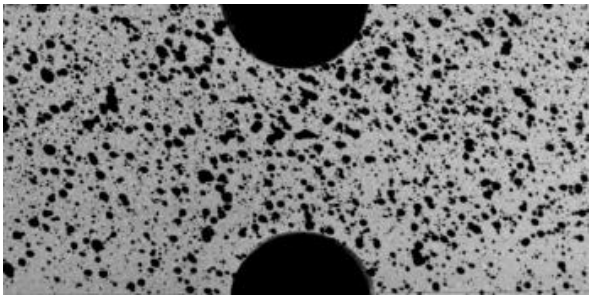

(a)

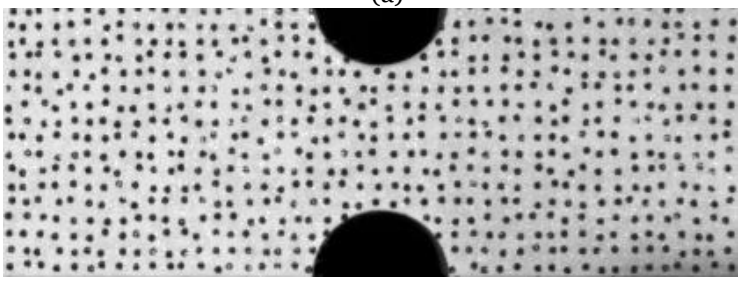

(b)

Figure 55 Spray painting (a) and toner transfer (b) techniques used to realize DIC patterns

6.4 Speckle pattern design

According to the recent literature, the quality of the speckle pattern deeply influences the final accuracy and the achievable spatial resolution of measurements made by means of digital image correlation [42]. An important characteristic of the technique adopted for pattern realization in the previous section is that the final pattern is numerically generated, meaning that it can be designed and consequently optimized by the user. Relying on literature information, the speckle shape has been selected to be circular in order to avoid preferential direction of local features. Furthermore, preventing sharp edges helps to reduce the high frequency components of the speckle pattern that may alias the measure. So, an ordinate grid of blobs with a given diameter d_p and average on-center spacing d_u is numerically generated. The ordinate grid is then randomized in both horizontal and vertical direction with a chosen level of variability (R), expressed as percentage of the on-center spacing value. Two types of synthetic speckle pattern are created (named '$P1$' and '$P2$'), varying the nominal diameter and the average distance among speckles (Figure 56). During the experimental activity, they are transferred on the two opposite beam surfaces (Figure 57), using the method explained in the previous section. Patterns characteristics are resumed in Table 5.

Table 5 Pattern properties

Pattern type	d_p[mm]	d_u[mm]	R[%]
P1	0.9	1.6	42
P2	0.7	1.4	50

Since the aim of this dissertation is to investigate the effect of motion blur on DIC measurements, the two pattern types are used only to study the influence of a realistic DIC image pattern on such a process, without dwelling on aspects connected to pattern optimization.

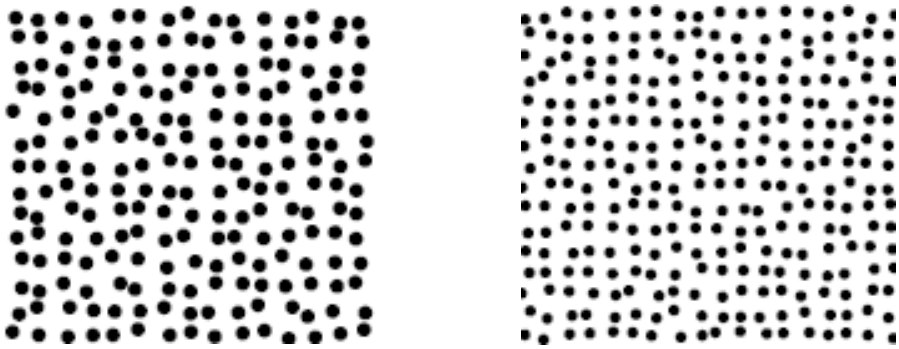

(a) (b)

Figure 56 Portions of numerically generated patterns. (a) 'P1'. (b) 'P2'

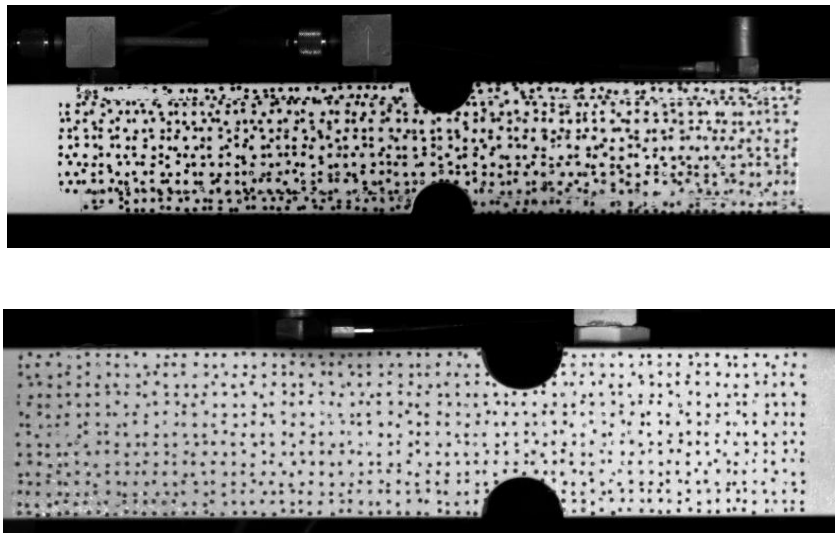

Figure 57 Synthetic patterns transferred on beam surfaces

6.5 Experimental activity

It is important to highlight that, before starting the dynamic tests, a proper combination of working distance and focal length must be chosen in order to have the total length of the beam inside the camera field of view. Moreover, the optical axis of the camera must be perpendicular with respect to the target surface to avoid geometric distortions. Since the height of the beam is limited, the vertical resolution size of the camera is reduced from top and down sides as much as possible, to increase the allowable frame rate and to reduce the amount of stored data. The latter corresponds to the possibility of increasing the recording time, achieving good frequency resolution during the following spectral analysis.
Furthermore, the lighting equipment must be regulated and oriented too, in order to guarantee the correct level of illuminance and avoid reflections (Figure 58 (a)).
Another standard procedure that needs to be carried out before running the test is the camera calibration, which allows to estimate the px to mm scaling factor, i.e. the ratio between the camera resolution (pixel) and the measurement region (mm), for the displacement fields. The procedure consists in the acquisition of a flat regular grid, as the one of Figure 58 (b), placed on the measurement surface. The physical grid spacing between the centres of each black circle is known (5 mm) and it is the same in both the horizontal and vertical directions of the image. It is consequently possible to estimate an average mm to px scaling factor for the displacements measured during DIC.

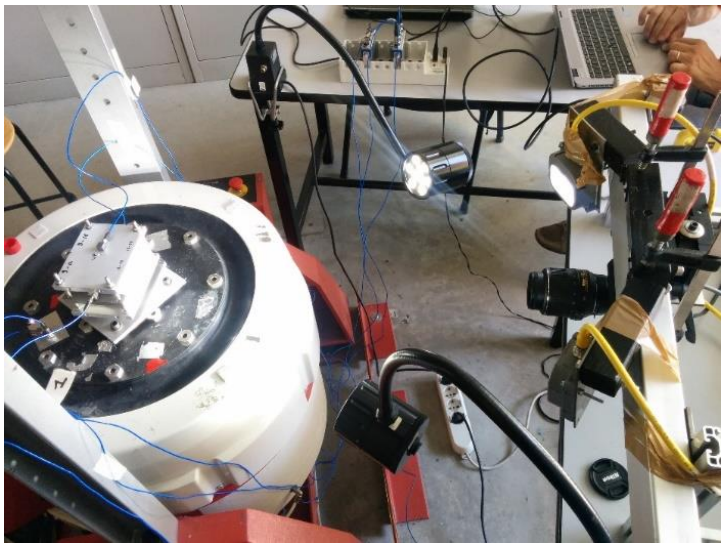

(a)

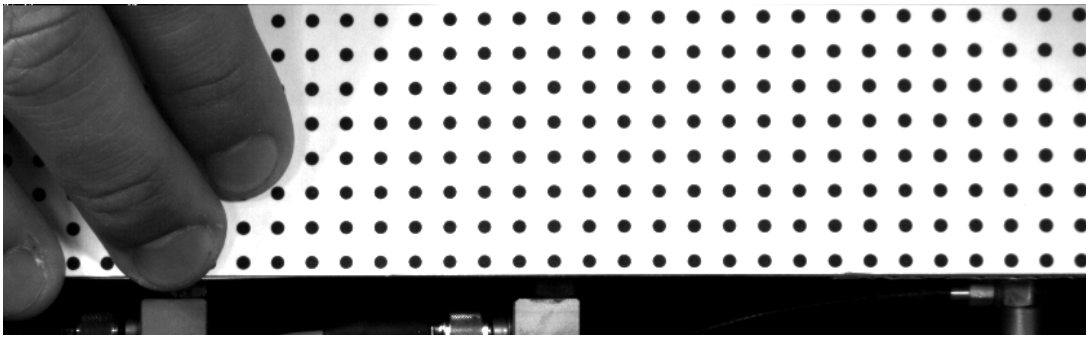

(b)

Figure 58 (a) Camera and lighting placement. (b) Calibration grid positioning

Once all the preliminary procedures have been completed, a group of experimental tests involving both the usage accelerometers and high-speed camera are conducted, tuning either the excitation or the acquisition parameters. For the harmonic test, the frequency and acceleration level are established to produce significant displacements close to the beam tip, which can be detected and measured by the camera. The selection of camera parameters, instead, requires a frame rate at least double of the excitation frequency to avoid aliasing conditions, in accordance with Shannon's theorem. Exposure time must assume relevant values to enhance the possibility for blurring conditions, while the digital gain is set equal to one for all the tests to obtain high-quality images (signal amplification implies also noise amplification). Then, an index named 'E2PR' is introduced, to quantify the ratio between the exposure time over the period of the target motion. It is a relevant parameter in case of sinusoidal motion [95].
All the experimental tests reported in Table 6 are repeated for each of the two pattern types. Before starting the excitation, a set of images of the beam in static conditions is acquired by the camera to be used as reference in the following DIC analysis.

Table 6 Specifications of the experimental tests

Type of excitation	Frequency [Hz]	Input acceleration [g]	Framerate [frame/s]	Shutter time [µs]	Gain	E2PR
Harmonic	100	2.18, 3.32, 4.43, 5.86, 7.31, 8.8	1000	998	1	0.0998
Harmonic	100	2.18, 3.32, 4.43, 5.86, 7.31, 8.8	500	1998	1	0.1998

The combination of these parameters gives origin to various levels of motion effect intensity. Furthermore, the selection of a harmonic signal as excitation implies the generation of different blurring conditions inside the single test itself. After an accurate observation of the recorded images, the harmonic test having frequency of 100 Hz, input acceleration of 5.86 g

and camera settings of 500 fps as framerate, 1998 μs as shutter time and E2PR equal to 0.1998 is chosen as reference and used for the following analysis, because it offers the possibility to find within the same test either moderate or important motion blur values on the acquired images.

6.5.1 Motion blur estimation using complex cepstrum

During the harmonic test execution, each point of the beam displaces with an increasing amplitude approaching to the free extremity, according to the first mode of the cantilever beam. As consequence, different blurring conditions appear along the beam length. It is decided to focus the further analysis on a small region of the images taken by the camera, which is located below the accelerometer mounted on the beam tip (Figure 59).

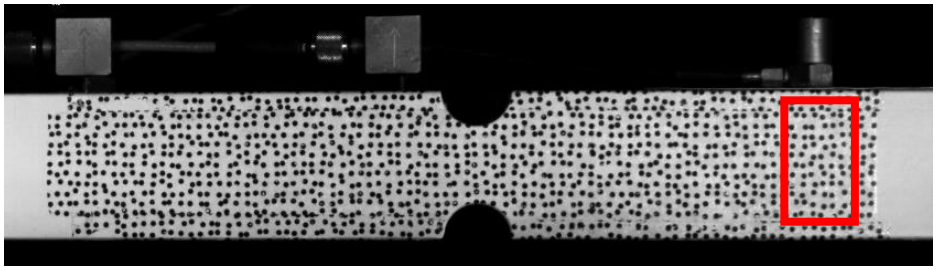

Figure 59 Region of analysis for motion blur estimation

Two periods of oscillation of the selected image region are analysed and the same procedure proposed in chapter 3 for motion blur estimation is applied to the acquired frames. In detail, the cepstrum of each column (vertical sinusoidal motion) of the blurred image C_B and that of the static image C_R are computed, then the relative difference ($C_{diff} = C_B - C_R$) is calculated. The procedure is repeated for all the columns of the images and the results are averaged. The application of inverse complex cepstrum back to frequency domain on such a difference gives as result the Fourier transform of motion blur (F_{diff}).

At this point, motion blur parameters are estimated fitting F_{diff} with a sinc function. In detail, the blur length w and the shift a are determined by fitting the amplitude and the phase of F_{diff}, respectively. It's important to underline that, for both pattern types, only the first lobe is used for the fitting, because the matching between the two curves is better in the low frequency range and therefore the estimation of motion blur is improved in this way (Figure 60). Moreover, only one threshold level is chosen, since important blur values (i.e. w>2 px) are obtained in all the analysed images, meaning that the main lobe is steep, with a zero-crossing which always occurred inside the Nyquist frequency range (0.5 px^{-1}).

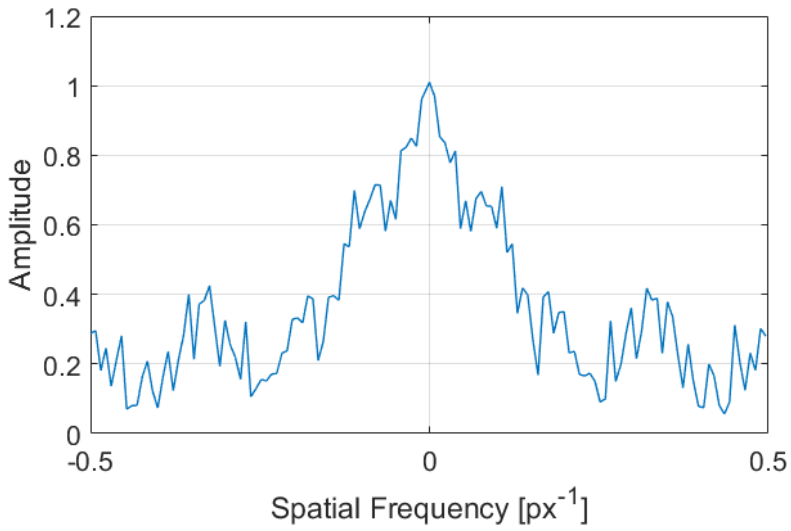

(a)

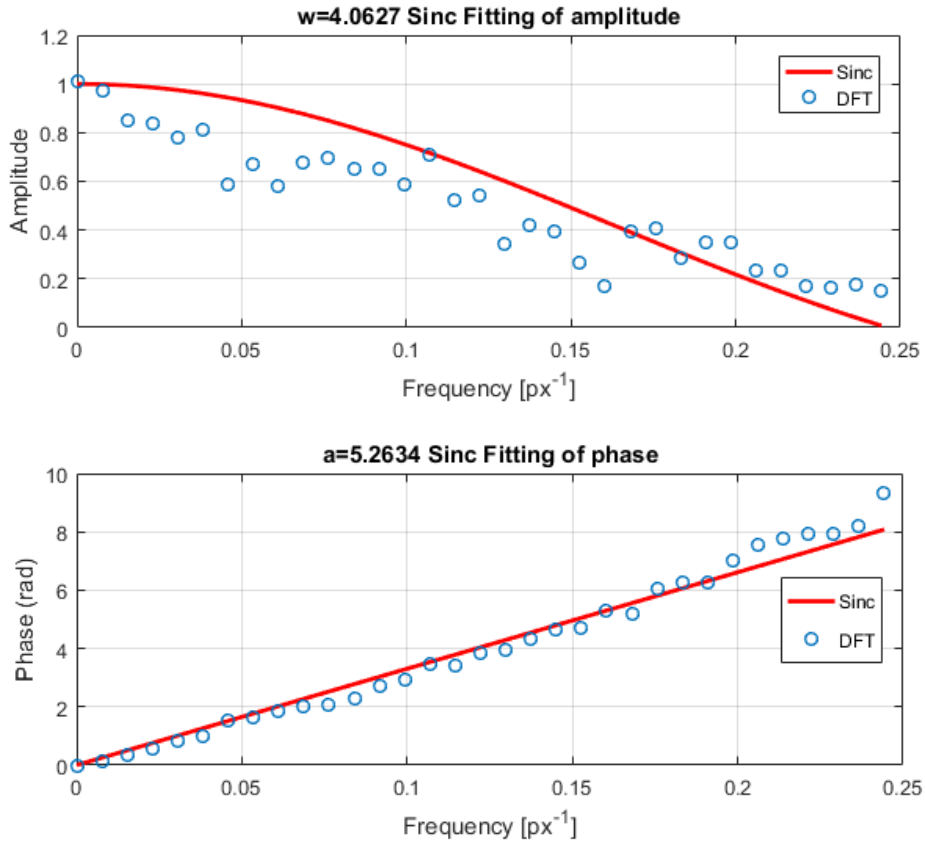

(b)

Figure 60 Example of F_{diff} function (a) and the relative fitting procedure (b)

The trend of estimated motion blur and shift are plotted in Figure 61, for all the images acquired by the camera during the two periods of oscillation. Since the excitation frequency is 100 Hz and the camera frame rate is 500 fps, during a single period of oscillation five images are grabbed.

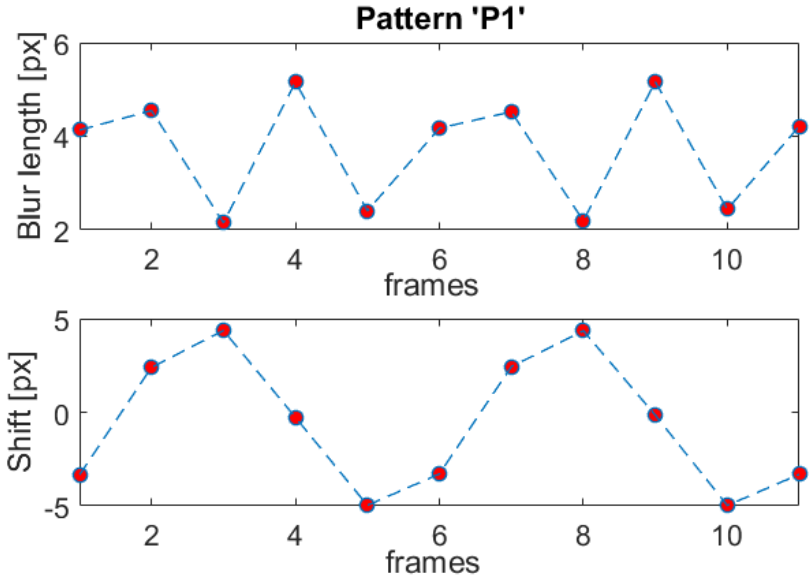

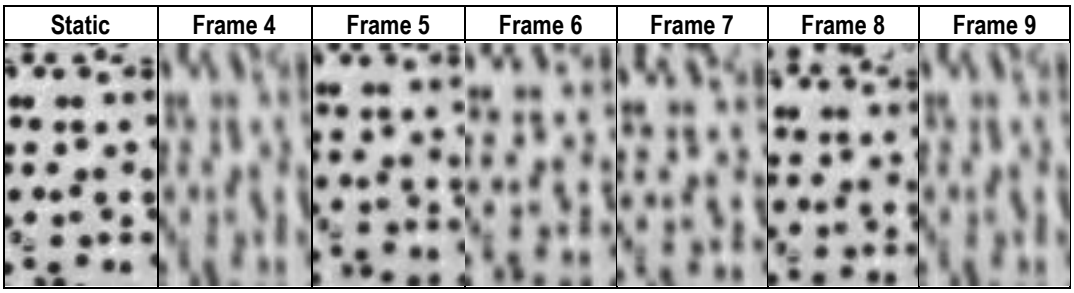

(a)

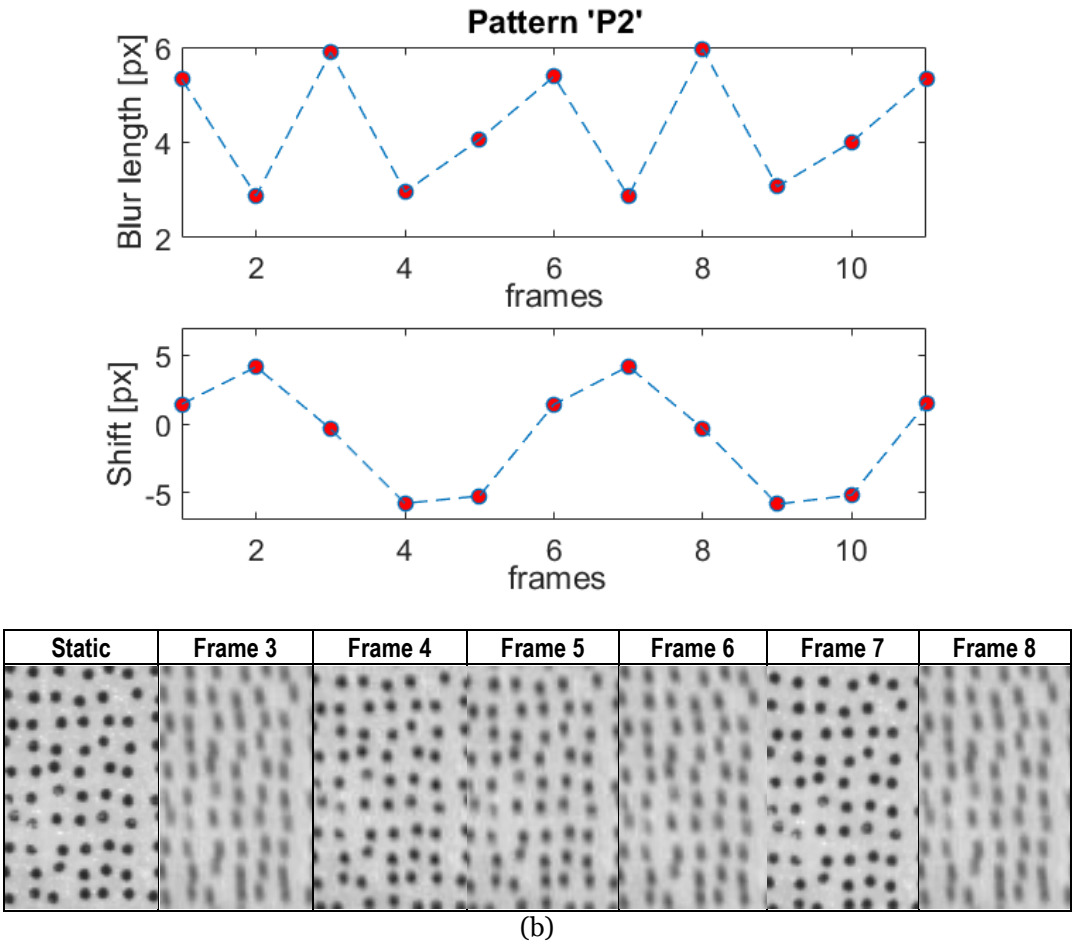

(b)

Figure 61 Estimation of motion blur and the corresponding shift in case of experimental test for Patterns 'P1' (a) and 'P2' (b)

Focusing the analysis on a single period of oscillation, i.e. frames from 4 to 9 for pattern 'P1' and frames from 3 to 8 for pattern 'P2', the highest motion effect values correspond to the moments in which the velocity of the target is the largest (zero-crossing points in sinusoidal motion). According to eq.(34), the maximum nominal blur length $w_{nom,\max}$ can be represented as the length that the target displaces during the exposure time, if it has the maximum speed in the whole interval:

$$w_{nom,max} = V_{max} \times sh = 2\pi f A_{nom} \times sh \qquad (34)$$

Where f and A_{nom} are the nominal frequency (in hertz) and the amplitude (in px) of the specific test and sh is the shutter time (in seconds).

The nominal amplitude of displacement is calculated starting from a_3 accelerometer data, dividing the amplitude of beam acceleration (estimated through spectral analysis) for the

square of the angular frequency and then converted in pixels through the scaling factor. Portion of the accelerometer time history in steady state conditions and the relative spectrum are shown in Figure 62.

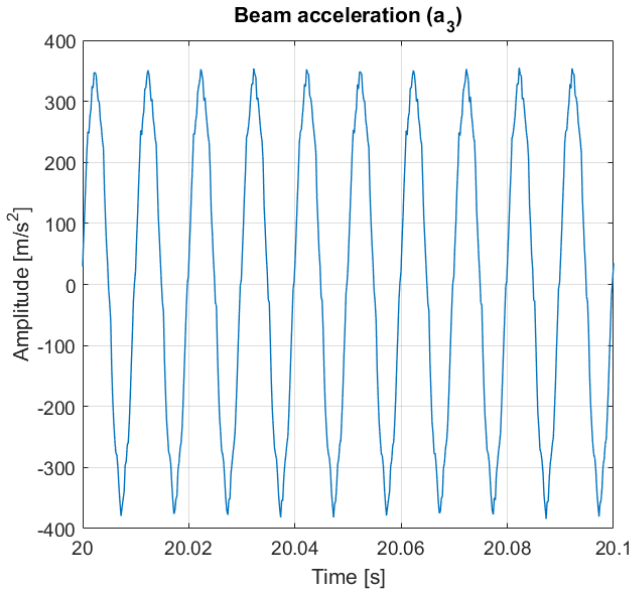

(a)

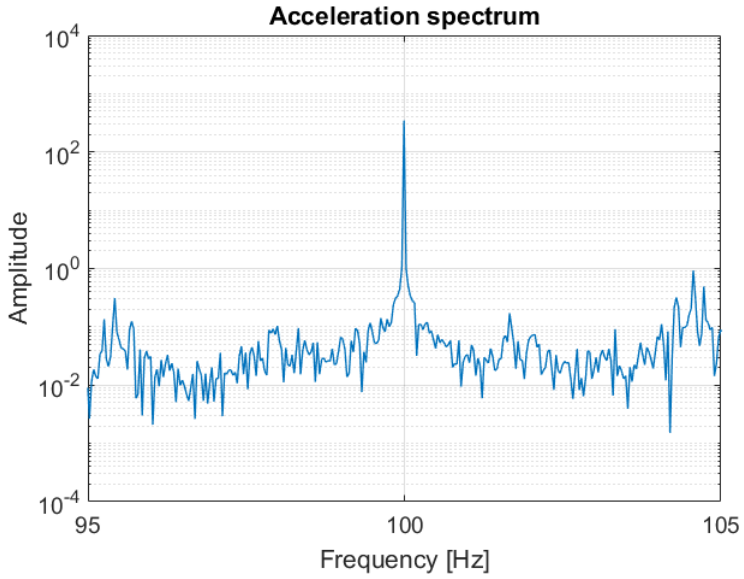

(b)

Figure 62 Portion of accelerometer a_3 time history (a) and the relative spectrum in logarithmic scale (b)

The results in terms of estimated and nominal maximum blur length for the two pattern types are reported in Table 7. They confirm that the acquired blurred images are characterized by a blur length which extends for several pixels in the region closer to the beam tip.

Table 7 Maximum nominal and estimated blur length for the two pattern types

Pattern type	A_{nom} [px]	$w_{nom,max}$ [px]	$w_{est,max}$ [px]
P1	4.98	6.26	5.16
P2	5.68	7.14	5.96

It should be emphasized that the formulation used to calculate the nominal maximum motion effect works under the hypothesis of constant target velocity during the camera exposure time. Since the ratio between the shutter time and the target motion period is relevant in the real test ($E2PR \cong 0.2$), variations in the target velocity occur inside the exposure interval and motion blur does not remain constant. For this reason, the nominal value of maximum blur length calculated with eq.(34) represents an overestimated version with respect to the real value. Another aspect to be taken into account is that the frames used for blur estimation $w_{est,max}$ could not be grabbed by the camera at the exact zero-crossing position of the sinusoidal motion. If this occurs, the motion effect present into the image only approaches the maximum quantity.

6.5.2 Motion blur removal using Wiener filter

The compensation of motion blur is pursued in this section using Wiener filter. From chapter 4, it has been possible to understand that such a method is the preferential deconvolution technique to be used for blur removal during a real image acquisition, where moderate level of noise is always present. To apply the filtering operation, it is necessary to define the optical transfer function (OTF) and the spectral distribution of the noise-to-signal ratio (NSR). The OTF is completely defined by the motion blur value w, estimated with the method described in the previous section. A correct definition of the SNR, instead, is essential to achieve good deconvolution results. The NSR is described by a matrix defined in frequency domain, having the same size of the image and containing the ratio between the power spectral density of the noise $N(u, v)$ and the power spectral density of the signal $S(u, v)$.

In a first restoration attempt of the blurred images coming from the dynamic test, the same algorithm presented in section 4.5.1 for NSR estimation has been used, giving back undesired results (Figure 63 (a)). This situation has occurred because, during the recording of the target surface in the experimental activity, various noises (e.g. heteroscedastic noise, shot noise, thermal noise, cut-off noise) and illumination lighting fluctuations are unavoidably presented

and most of them are characterized by a peculiar spectral distribution, as already demonstrated at the end of section 4.5.2. On the contrary, synthetic images were numerically generated, and the only source of noise was the Gaussian one introduced by the user. Therefore, their power spectral density distribution was much easier to be estimated.
To overcome such an issue, an alternative approach for NSR estimation is presented, aiming to mitigate the discrepancies in the matching of noise frequency distribution. In this regard, the set of static images acquired before starting the harmonic test may be useful. The first image of the series is chosen as reference and its Root Mean Square (RMS) is calculated, according to eq.(35):

$$RMS = \sqrt{\frac{\sum_{j=1}^{n}\sum_{i=1}^{m}(\bar{p} - p_{i,j})^2}{m \cdot n}} \tag{35}$$

Where $\bar{p}$ is the mean value of the image, $p_{i,j}$ is the pixel intensity and m, n are the number of columns and rows of the image, respectively.
Then, the mean value is subtracted from all the still images to compensate for variations in lighting conditions. Finally, the reference image is subtracted from each one of the remaining images, the standard deviation of the matrix difference is computed, and the results are averaged for the number of involved images.
In this way it is possible to calculate the NSR as the ratio between the averaged standard deviation of the image series, which represents an index for the noise level, and the RMS of the reference image, which represents an index for the signal level. For sake of clarity, an example of Wiener filter output using the new NSR definition is reported in Figure 63 (b).

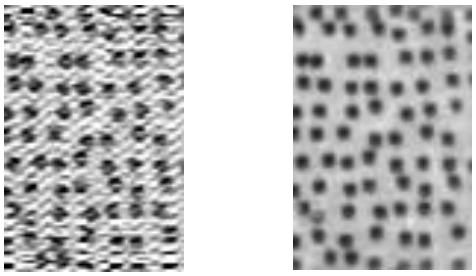

(a) (b)

Figure 63 Output of Wiener filtering coming from two different definitions of NSR

To validate the effectiveness of the compensation method, the above procedure is repeated for all the blurred images belonging to the two periods of oscillation of the sinusoidal motion. As illustrative case, in Figure 64 the images before and after blur removal are reported for the two

pattern types, focusing the attention on the same period of target motion just considered in Figure 61.

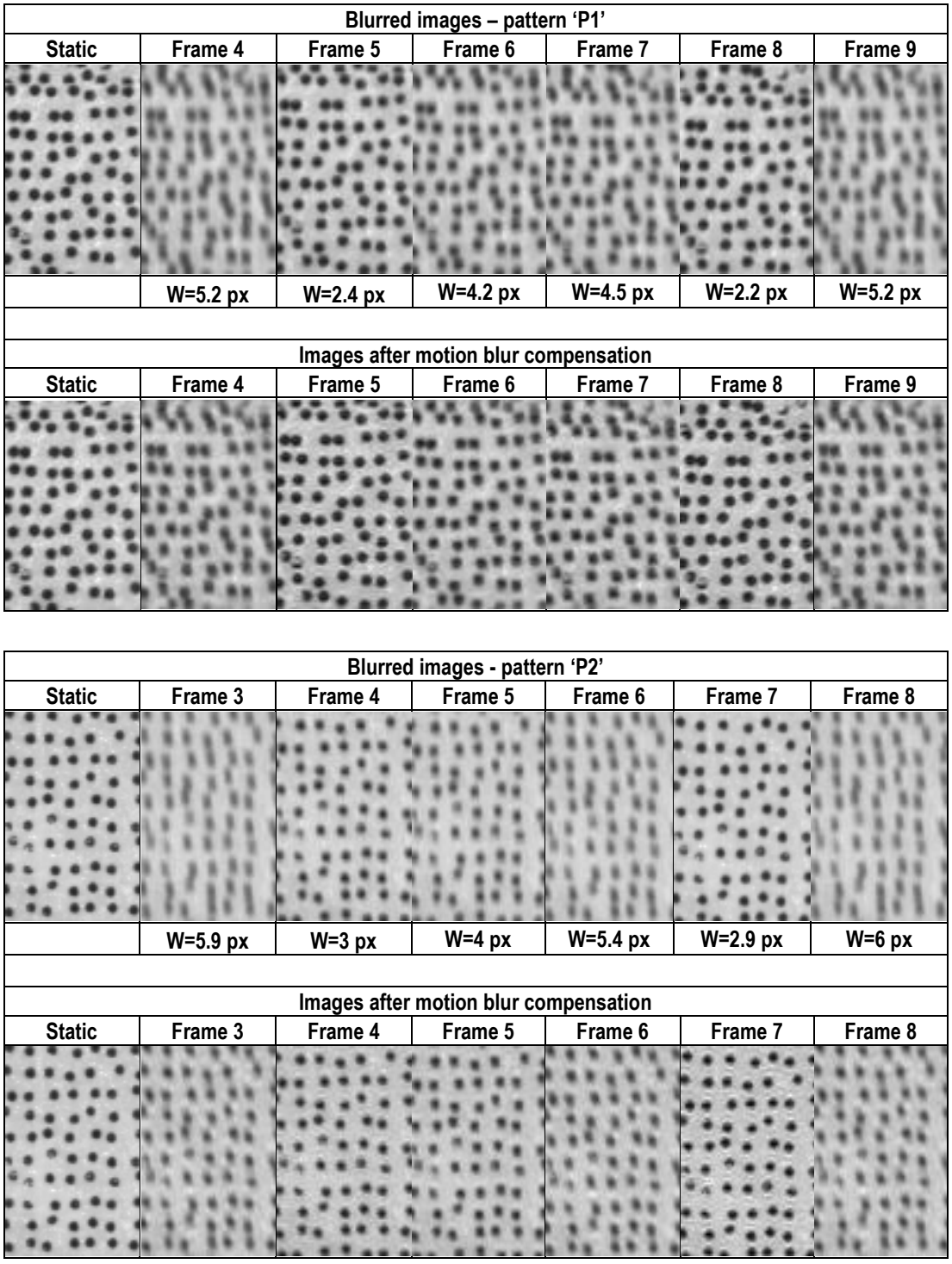

Figure 64 Compensation results after Wiener filtering for patterns 'P1' and 'P2'.

From a preliminary observation of the above figures, the images after blur removal seem to partially resemble the corresponding static case, meaning that the motion effect has been compensated in some way. However, the visual quality of the restored images is not so high as for ones of the synthetic experiments. This could be connected to different causes, including:

- Errors in the blur length estimation: the obtained Fourier transform of motion blur (F_{diff}) is very irregular, not permitting a robust fitting operation to evaluate w and, as consequence, a proper estimation of the Optical Transfer Function.
- Errors in the noise modelling: as just explained, every time the exact noise frequency distribution is not matched, artefacts are produced as output by the Wiener restoration engine.

For a quantitative analysis, the mean intensity gradient (MIG) and the sum of square of subset intensity gradient (SSSIG) are calculated and displayed in Figure 65. The lowest values of MIG and SSSIG are achieved where the motion blur intensity is the maximum, i.e. in the frames corresponding to positions closer to the zero crossing of the sinusoidal motion, confirming that motion effect is a relevant source of pattern degradation. After blur compensation, the two indexes increase their values for every frame of the period, approaching the ones of the relative static images. This testifies that an improvement in the image quality is done.

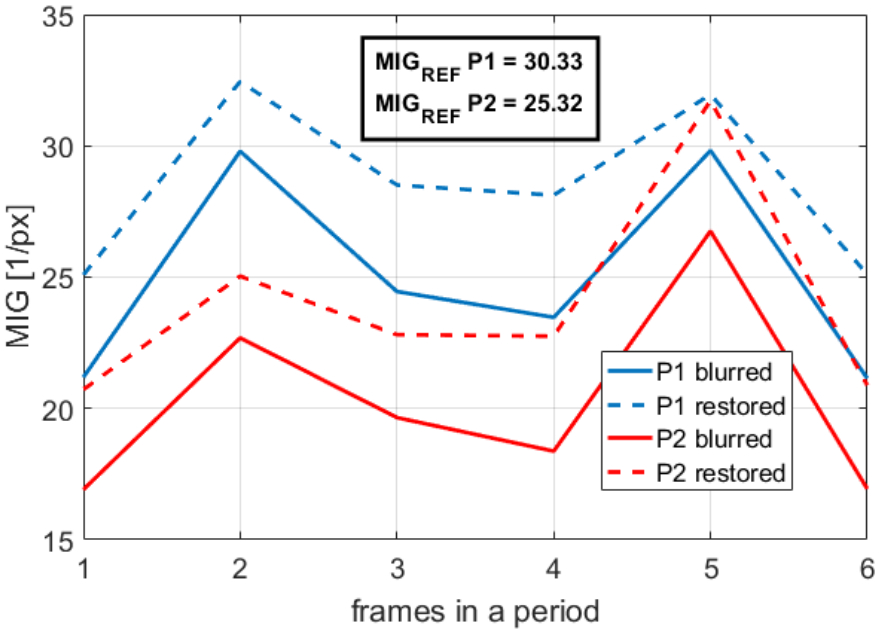

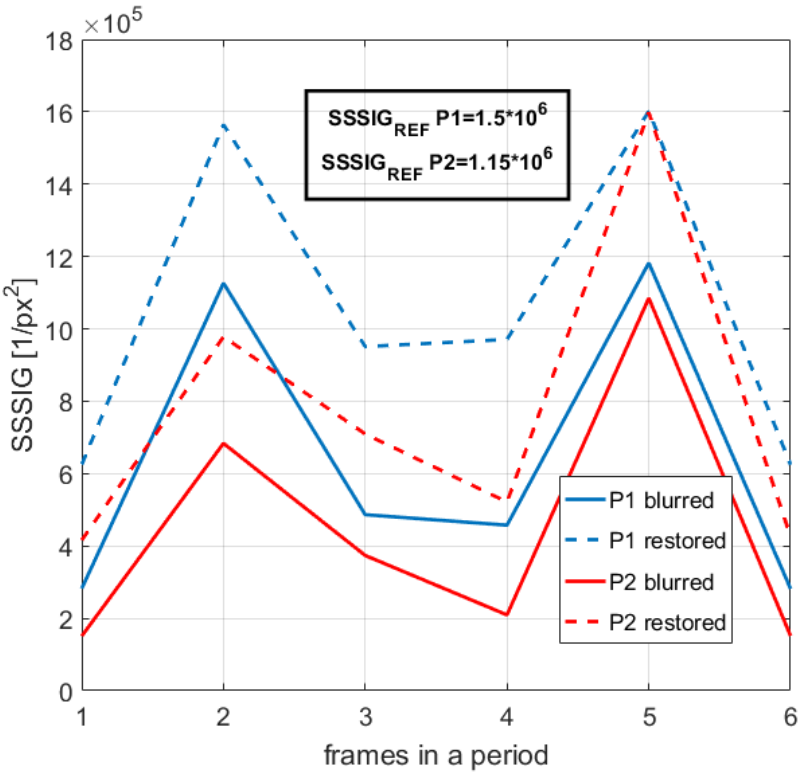

Figure 65 MIG and SSSIG trend for patterns 'P1' and 'P2' before and after blur removal, considering one period of oscillation

Since MIG and SSSIG rely on spatial gradients, which measure the change of intensity in the image pixel according to a specific direction, their values should be the maximum admitted if calculated on the static image version. In fact, motion effect is responsible of a decrease in the image contrast, which implies a reduction of the image gradient along blurring direction. In correspondence of frame 5 of the above figure, contrary to one could expect, both the MIG and SSSIG exceed the static values after blur compensation. This unexpected behaviour corresponds to a situation in which the Wiener filter generates artefacts into the restored image, which modify the original intensity image profile and so the relative MIG, SSSIG indexes.

6.5.3 DIC analysis after blur compensation

In chapter 5, it has been clearly demonstrated that the presence of motion effect has a negative influence on DIC measurements. The standard deviation of displacement (rather than the mean displacement) is the most meaningful quantity which must be considered when motion blur phenomena occur, since it grows as fast as w increases. Therefore, blur compensation could be an appropriate solution to improve the DIC performances in dynamics. A procedure similar to the one adopted for the synthetic images is developed there, since there is a need to validate it also in a real experimental context. At first, the same blurred images of section 6.5.1, corresponding to two periods of target oscillation close to beam tip, are considered and motion blur is compensated for each of them using Wiener filter. Then, DIC analysis is performed using *Ncorr* software on both the blurred and the de-blurred image series. Once again, to achieve an efficient analysis, the same subset parameters are maintained (Table 8).

Table 8 Ncorr parameters for DIC analysis on experimental images

Pattern type	Size (px)	Subset radius (px)	Subset spacing (px)
P1	61 x 91	10	2
P2	67 x 131	10	2

DIC process returns as output the mean displacement and the corresponding standard deviation for each image, considering the static image as reference version for the measurements. In Figure 66 and Figure 67 the results for patterns 'P1' and 'P2' are reported, in terms of bias error of vertical mean displacement before and after blur removal ($\bar{v}_{blur} - \bar{v}_{restored}$) and of standard deviation of displacement.

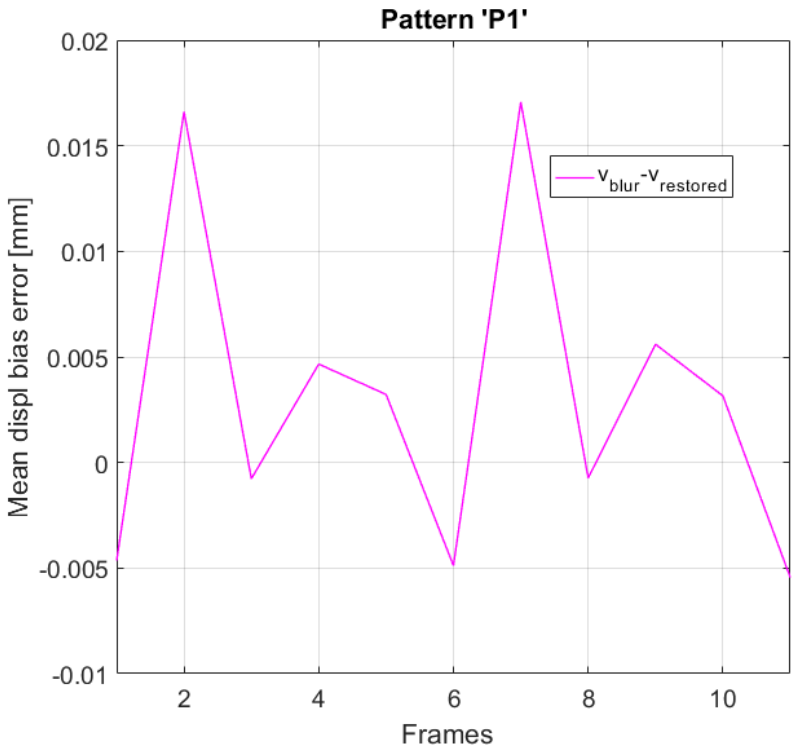

(a)

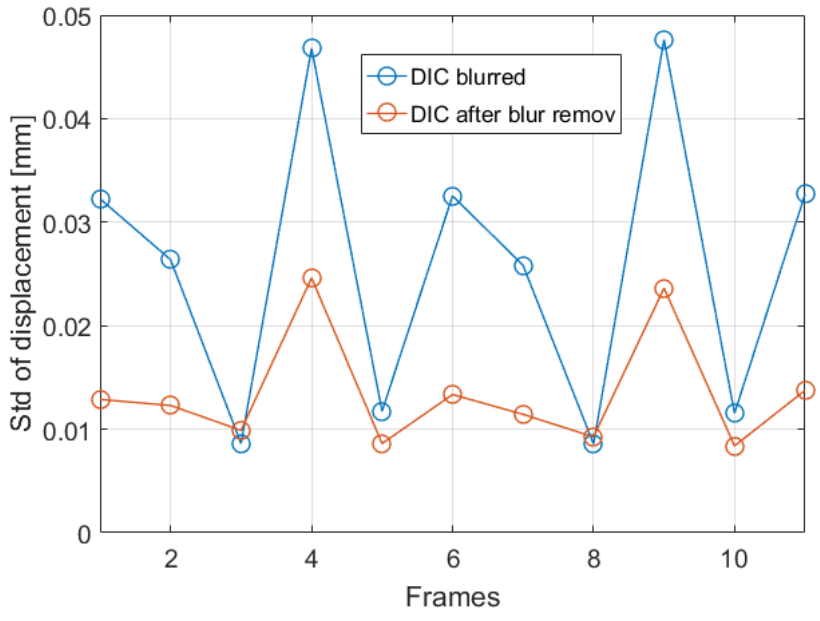

(b)

Figure 66 Mean (a) and standard deviation (b) of displacement calculated by DIC for pattern 'P1'

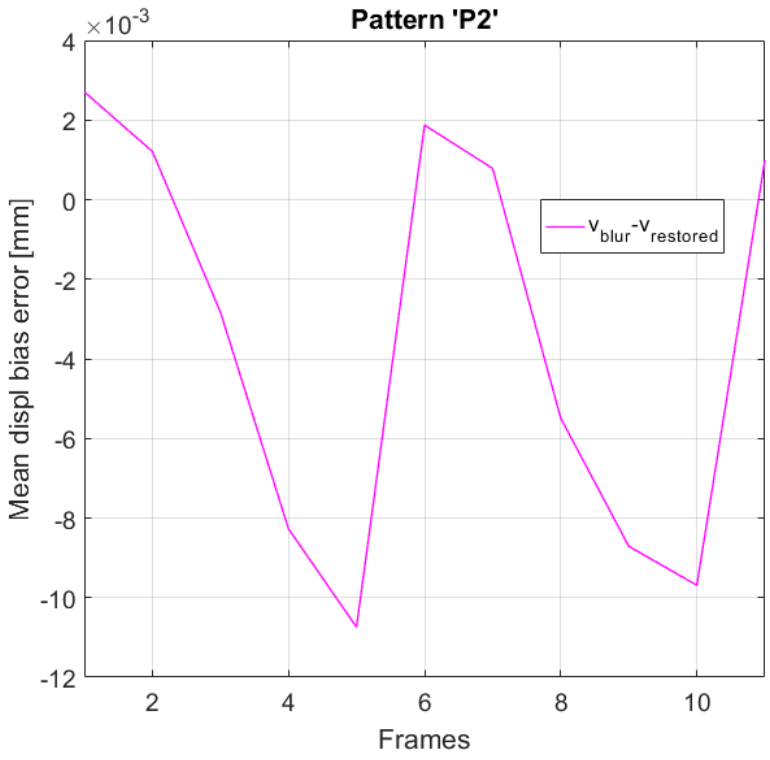

(a)

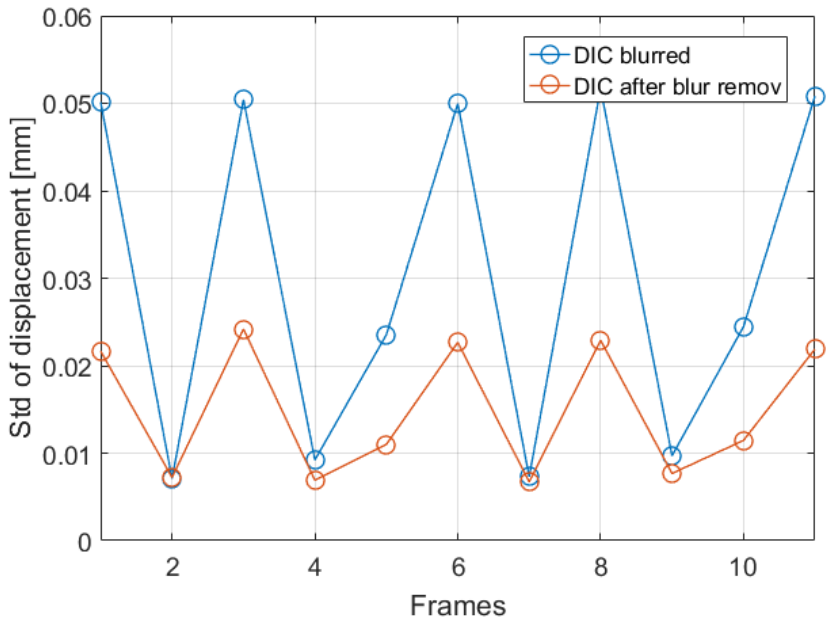

(b)

Figure 67 Mean (a) and standard deviation (b) of displacement calculated by DIC for pattern 'P2'

By observing the trend of the previous graphs, some interesting features appear for both pattern types:

- The graph of standard deviation assumes a sort of periodic behaviour, where the presence of peaks is associated to the frames acquired when the target was passing to the neutral position, i.e. the ones with the highest level of motion blur.
- DIC estimation of mean displacement remains almost completely unchanged after blur compensation. This agrees to what has been found in [95].
- At the same time, DIC uncertainty strongly reduces after blur removal, especially in the frames where the peak levels appear. In this latter case the amount of reduction is close to 50%.
- An exception to what just said is represented by the frames 3 and 8 of pattern 'P1'. In fact, they are characterized by an increase of uncertainty after blur compensation. Such a behaviour is directly connected to the presence of some artefacts, produced during image restoration with Wiener filter, as explained in the previous section. However, the amount of increase is extremely low, and the level of uncertainty remains practically equal to the value obtained in static conditions. Therefore, the phenomenon can be considered negligible for the purposes of this work.

These considerations confirm that motion blur is a relevant source of uncertainty dealing with dynamic applications. For images acquired in a real experimental context, the technique proposed to compensate the motion blur can significantly improve the accuracy of DIC measurements for both pattern types, reducing the standard deviation of displacement without modifying significantly its mean value.

At this point, it becomes interesting to compare also the displacement measured by DIC to the one estimated through the cesptrum-based algorithm of section 6.5.1, obtained through the phase fitting of F_{diff} function. Figure 68 clearly highlights that the estimated motion (yellow curve) approaches the ones coming from the DIC process (red and blue curves), proving that the proposed technique is an accurate method for image shift calculation.

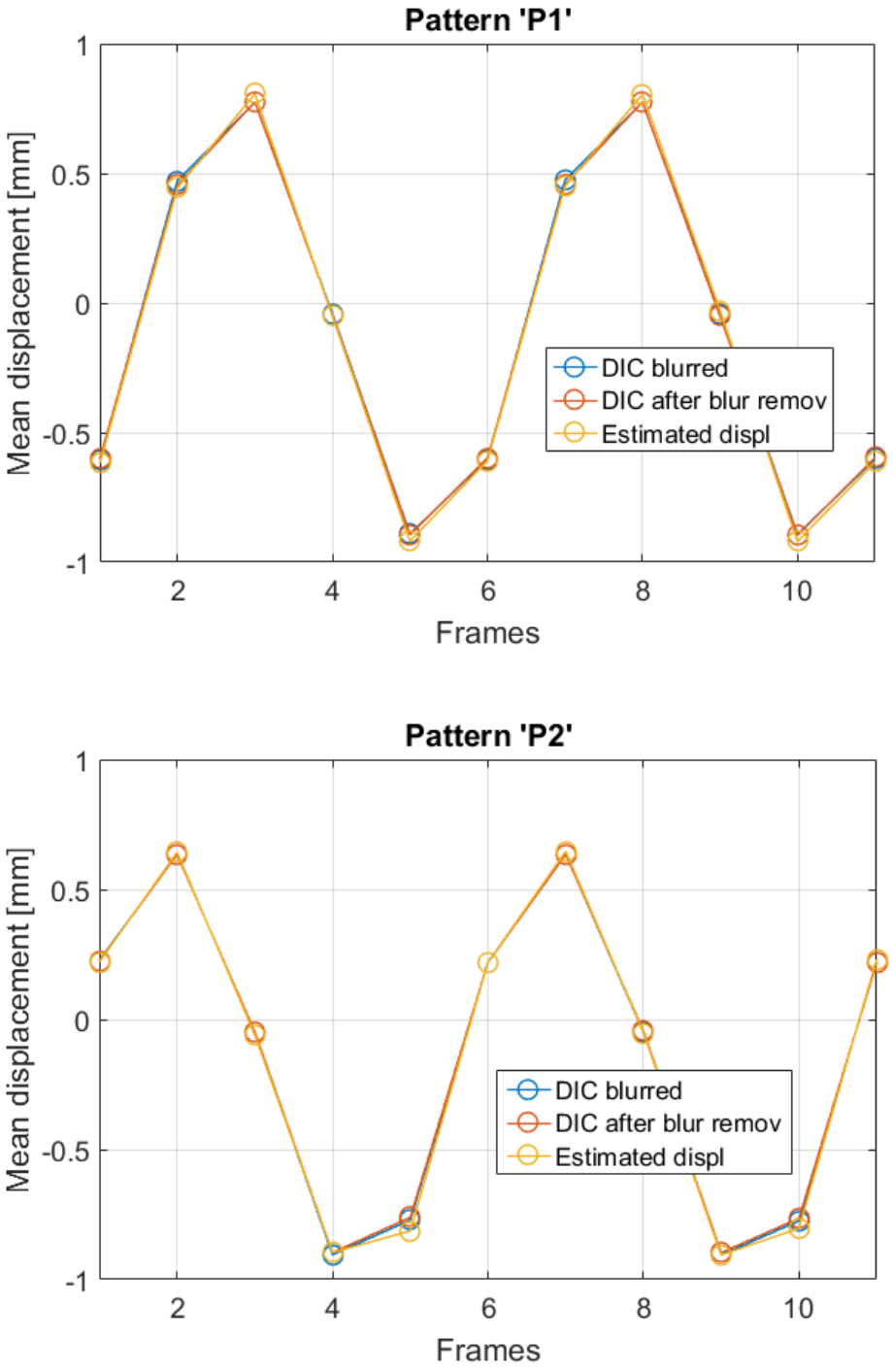

Figure 68 Comparison between DIC mean displacement and the one estimated with complex cepstrum

Remarks and conclusions

The aim of this thesis was to provide a novel approach aiming to compensate motion blur effect on Digital Image Correlation (DIC) measurements. The review of several researches identified motion blur as a phenomenon of major importance when vision systems were adopted in dynamic applications, since the quantification of the measurement uncertainty was strongly influenced by the blurring due to the relative motion between camera and target during the shutter time. Therefore, a good displacement estimation depended also on the dynamic camera parameters, such as the grabbing frequency or the exposure time. For these reasons, many researchers found a workable solution to prevent blur generation in boosting the lighting level and selecting very low exposure times, allowing to shoot the moving object in quasi-static conditions [104]. Unfortunately, it is not possible to respect these conditions in all the measurement tasks. We should think of the case of a camera mounting on a flying drone [103], where lighting conditions cannot be easily controlled, or the case of structure monitoring, where the application of vision systems often requires working with natural light [105]. Where the exposure time cannot be set arbitrarily, a further step is to compensate the undesired effect coming from motion blur through image deconvolution.

To remove motion blur, it is of primary importance to evaluate its intensity in a reliable way. A first original contribution of this work was the development of a technique, based on convolution and cepstral analysis, to estimate motion blur. In agreement with eq.(27), starting from the knowledge of both the reference image and its blurred version, the difference between their respective cepstra permitted to extract a function containing all the information about motion blur. Thus, considering such a difference and passing to a frequency domain analysis, the function representing motion blur assumed a “sinc-like” shape. Therefore, a fitting procedure allowed to extract motion blur parameters (i.e. the blur length ‘w’ and net displacement ‘a’) in an accurate way. Although it has been proven that sinc fitting accuracy reduced when blur intensity was less than 1 px, small values of motion blur were considered negligible for the purposes of this work, since they had an irrelevant impact on DIC uncertainty.

The estimation algorithm was tested on three types of synthetic DIC patterns. Blurring conditions up to 8 pixels were numerically generated in the images, using the motion effect simulation technique illustrated in section 1.4.2. Results showed that the error between the nominal and the estimated blur values was always lower than 0.1 px, justifying the robustness

of the estimation procedure. Then, two distinct levels of zero-mean Gaussian noise (having standard deviation equal to 2% and 8% of the full dynamic range, respectively) were added to each image. Even though noise contribution influenced the estimation process, motion blur remained the predominant source of error.
Finally, the influence of image pattern was investigated, detecting that the presence of sharp contrast helped to increase the reliability of the results, especially for slight blurring conditions.
Once motion blur was fully identified, the next step provided for its removal. The compensation of motion blur was pursued by means of two methods: one based on cepstral analysis and the other on the use of Wiener filter. Both were presented in chapter 4. The whole procedure was validated on the same types of DIC pattern used in the estimation process, where motion blur levels up to 8 px were simulated. To resemble realistic operating conditions, also the two Gaussian noise levels were added to the images.
Considering the cepstral method, motion blur was removed with a subtraction operation in cepstrum domain. In fact, the input function for cepstrum calculation which described motion blur was completely known (eq. (28)), since 'w' and 'a' were calculated by the estimation algorithm of chapter 3.
Wiener filter was introduced as a viable solution to remove motion blur, too. While the Optical Transfer Function (OTF) required from the filter implementation was fully defined by the motion blur value w, the achievement of a correct SNR definition was fundamental for good deconvolution results in a noisy context. In this work the SNR level was estimated by processing a sequence of static images of the target.
Results showed that, even if cepstrum-based deconvolution for blur removal was very effective in absence of noise, as the noise level increased, the compensated images contained significant artefacts. Wiener filter, on the contrary, generated artefact-free images even in the case of noisy images, provided that the SNR and the OTF were correctly estimated.
In chapter 5, the blurred images having the numerically imposed motion effect were submitted to the DIC analysis. From DIC data emerged that the standard deviation of the displacement field was the most meaningful quantity to be considered in the description of motion blur phenomena, since it grew as fast as w increased and it was at least one order of magnitude bigger than the corresponding bias error in mean displacement.
Then, images containing the two levels of additive noise were examined too. DIC outcomes testified that, although Gaussian noise affected both the bias and the random error, the blurring due to motion increased the uncertainty much more than the noise.

Once demonstrated that DIC measurements suffered motion blur presence, the compensation of this phenomenon was tested, using the deblurred images coming from the two deconvolution algorithms.

- Since deblurring using cepstrum was not robust on images containing uncorrelated noise, the noiseless image groups were involved. After the compensation of motion blur, the standard deviation of displacements was strongly reduced for all the pattern types, especially when blur became more intense (w > 3 px).
- Wiener filter, instead, was applied to the same types of blurred images used for the cepstrum-based deconvolution, with the addiction of Gaussian noise having zero mean and standard deviation equal to 2% of the dynamic range. After motion blur compensation, standard deviation was reduced, although in a less evident way than in the case of noiseless deconvolution. This was expected, since deconvolution compensated for the motion blur contribute, but fluctuations due to noise remained. In addition, it was found that the generic uncertainty rejection procedure was more effective on non-regular patterns, since they were able to better handle the exogenous effects, either they were noise or motion blur.

The last part of the works was focused on the experimental validation of the previously presented techniques, i.e. motion blur estimation and compensation. The basic idea was to simulate a realistic dynamic application in which DIC measurements could be involved. The subject of the analysis was an aluminium bar, clamped at one extremity and submitted to imposed sinusoidal vibrations. Two distinct types of speckle patterns were attached on the planar surface of the beam to be tested, while the target motion was recorded by a high-speed camera. All the relevant excitation and camera parameters were tuned in order to obtain, in correspondence of the free extremity of the beam, different blurring conditions during the harmonic motion.
First, cepstrum-based algorithm was applied on the acquired images to estimate the motion blur values. Then, Wiener filter was adopted for the blur compensation. Finally, DIC analysis was performed on both blurred and deblurred images aiming to compare the behaviour of the DIC displacement uncertainty. The following results were obtained:

- The maximum values of uncertainty were associated to the frames acquired when the target was passing to the neutral position, i.e. the ones characterized by the maximum velocity and therefore the highest level of motion blur.
- The estimation of mean displacement remained almost unchanged after blur compensation, while DIC uncertainty strongly reduced, especially in the frames where the maximum blur levels appeared. In this latter case the amount of reduction was close to 50%.

These considerations agreed with the outcomes of the simulation activity performed on synthetic images, confirming that motion blur was a relevant source of uncertainty for DIC to be taken into account when passing to dynamic conditions. Also for images acquired in a real experimental context, the techniques proposed either to estimate or to compensate the motion blur were validated, since they could significantly improve the accuracy of DIC measurements.

As a final remark and proposal of future work, the author's wish is to extend the procedures of motion blur estimation and compensation to the entire length of the clamped beam, aiming to reconstruct its full-field displacement, and then to evaluate the accuracy of DIC measurements before and after blur removal. Another attractive area for future researches may be a deeper understanding of the motion blur phenomenon in cepstrum domain, in order to extract the relevant blur parameters directly in such a domain, without passing from frequency analysis.

References

[1] B Pan, K Qian, H Xie, A Asundi. Two-dimensional digital image correlation for in-plane displacement and strain measurement: A review, Measurement Science and Technology. 20 (2009).

[2] PK Rastogi. Photomechanics, Topics in Applied Physics. (2000)

[3] MA Sutton, JJ Orteu, HW Schreier, Image Correlation for Shape, Motion and Deformation Measurements; Basic Concepts, Theory and Applications, Springer (2009).

[4] WH Peters, WF Ranson. Digital imaging techniques in experimental stress analysis. Optical Engineering. 21 (1982) 427-431.

[5] TC Chu, WF Ranson, MA Sutton. Applications of digital-image correlation techniques to experimental mechanics, Exp. Mech. 25 (1985) 232-244.

[6] M Sutton, C Mingqi, W Peters, Y Chao, S McNeill. Application of an optimized digital correlation method to planar deformation analysis, Image Vision Comput. 4 (1986) 143-150.

[7] WH Peters, WF Ranson, MA Sutton, TC Chu, J Anderson. Application of digital correlation methods to rigid body mechanics. Optical Engineering. 22 (1983) 738-742.

[8] MA Sutton, SR McNeill, JD Helm, YJ Chao. Advances in two-dimensional and three-dimensional computer vision, Photomechanics. 77 (2000) 323-372.

[9] HW Schreier. Investigation of two and three-dimensional image correlation techniques with application in experimental mechanics. PhD Thesis. (2003).

[10] D Zhang, X Zhang, G Cheng. Compression strain measurement by digital speckle correlation, Exp. Mech. 39 (1999) 62-65.

[11] P Zhou, KE Goodson. Subpixel displacement and deformation gradient measurement using digital image/speckle correlation (DISC), Optical Engineering. 40 (2001) 1613-1620.

[12] BK Bay. Texture correlation: A method for the measurement of detailed strain distributions within trabecular bone, Journal of Orthopaedic Research. 13 (1995) 258-267.

[13] DJ Chen, FP Chiang, YS Tan, HS Don. Digital speckle-displacement measurement using a complex spectrum method, Appl. Opt. 32 (1993) 1839-1849.

[14] GR Gaudette, J Todaro, IB Krukenkamp, F- Chiang. Computer aided speckle interferometry: A technique for measuring deformation of the surface of the heart, Ann. Biomed. Eng. 29 (2001) 775-780.

[15] M Sjödahl, LR Benckert. Electronic speckle photography: Analysis of an algorithm giving the displacement with subpixel accuracy, Appl. Opt. 32 (1993) 2278-2284.

[16] M Sjodahl, LR Benckert. Systematic and random errors in electronic speckle photography, Appl. Opt. 33 (1994) 7461-7471.

[17] M Sjodahl. Electronic speckle photography: increased accuracy by nonintegral pixel shifting, Appl. Opt. 33 (1994) 6667-6673.

[18] M Sjödahl. Accuracy in electronic speckle photography, Appl. Opt. 36 (1997) 2875-2885.

[19] D Zhang, M Luo, DD Arola. Displacement/strain measurements using an optical microscope and digital image correlation, Optical Engineering. 45 (2006).

[20] N Sabaté, D Vogel, A Gollhardt, J Keller, C Cané, I Gràcia, et al. Residual stress measurement on a MEMS structure with high-spatial resolution, J Microelectromech Syst. 16 (2007) 365-372.

[21] MA Sutton, N Li, D Garcia, N Cornille, JJ Orteu, SR McNeill, et al. Scanning electron microscopy for quantitative small and large deformation measurements Part II: Experimental validation for magnifications from 200 to 10,000, Exp. Mech. 47 (2007) 789-804.

[22] S Cho, JF Cárdenas-García, I Chasiotis. Measurement of nano displacements and elastic properties of MEMS via the microscopic hole method, Sens Actuators a Phys. 120 (2005) 163-171.

[23] B Pan. Reliability-guided digital image correlation for image deformation measurement, Appl. Opt. 48 (2009) 1535-1542.

[24] MA Sutton, JL Turner, HA Bruck, TA Chae. Full-field representation of discretely sampled surface deformation for displacement and strain analysis, Exp. Mech. 31 (1991) 168-177.

[25] G Vend Roux, WG Knauss. Submicron deformation field measurements: Part 2. Improved digital image correlation, Exp. Mech. 38 (1998) 86-92.

[26] HW Schreier, JR Braasch, MA Sutton. Systematic errors in digital image correlation caused by intensity interpolation, Optical Engineering. 39 (2000) 2915-2921.

[27] A Giachetti. Matching techniques to compute image motion, Image Vision Comput. 18 (2000) 247-260.

[28] B Pan, H Xie, Z Guo, T Hua. Full-field strain measurement using a two-dimensional Savitzky-Golay digital differentiator in digital image correlation, Optical Engineering. 46 (2007).

[29] F Boochs. Off-line compilation of photogrammetric stereo models using digital image correlation, Photogrammetria. 41 (1987) 183-199.

[30] UV Helava. Digital correlation in photogrammetric instruments, Photogrammetria. 34 (1978) 19-41.

[31] WG Knauss, I Chasiotis, Y Huang. Mechanical measurements at the micron and nanometer scales, Mech. Mater. 35 (2003) 217-231.

[32] Z- Zhang, Y- Kang, H- Wang, Q- Qin, Y Qiu, X- Li. A novel coarse-fine search scheme for digital image correlation method, Meas J Int Meas Confed. 39 (2006) 710-718.

[33] B Pan, H Xie, Y Xia, Q Wang. Large-deformation measurement based on reliable initial guess in digital image correlation method, Guangxue Xuebao/Acta Optica Sinica. 29 (2009) 400-406.

[34] HA Bruck, SR McNeill, MA Sutton, WH Peters III. Digital image correlation using Newton-Raphson method of partial differential correction, Exp.Mech. 29 (1989) 261-267.

[35] B Pan. Reliability-guided digital image correlation for image deformation measurement, Appl. Opt. 48 (2009) 1535-1542.

[36] M. Bornert, F. Brémand, P. Doumalin, J. Dupré, M. Fazzini, M. Grédiac, F. Hild, S. Mistou, J. Molimard and J. Orteu, "Assessment of digital image correlation measurement errors: methodology and results," Exp. Mech., vol. 49, pp. 353-370, 2009.

[37] Roux S, Hild F. Stress intensity factor measurements from digital image correlation: post-processing and integrated approaches. Int J Fract 2006; 40:141–57.

[38] Besnard G, Hild F, Roux S. Finite-element displacement fields analysis from digital images: application to Portevin–Le Châtelier bands. Exp Mech 2006; 46 (6): 789–803.

[39] Wang YQ, Sutton MA, Reu PL, Miller TJ. Image matching error assessment in digital image correlation. In: Proceedings of the SEM annual conference. Albuquerque New Mexico, USA; 2009.

[40] Wang YQ, Sutton MA, Bruck HA, Schreier HW. Quantitative error assessment in pattern matching: effects of intensity pattern noise, interpolation, strain and image contrast on motion measurements. Strain 2009; 45:160–78.

[41] Reu PL, Sutton MA, Wang Y, Miller TJ. Uncertainty quantification for digital image correlation. In: Proceedings of the SEM annual conference. Albuquerque New Mexico USA; 2009.

[42] Pan B, Qian K, Xie H, Asundi A. On errors of digital image correlation due to speckle patterns. In: Proceedings of the international conference on experimental mechanics; 2008. p. z1: z7.

[43] W. Wang, J. E. Mottershead, T. Siebert and A. Pipino, "Frequency response functions of shape features from full-field vibration measurements using digital image correlation," Mechanical Systems and Signal Processing, vol. 28, pp. 333-347, 2012.

[44] W. Wang, J. E. Mottershead and C. Mares, "Vibration mode shape recognition using image processing," J. Sound Vibrat., vol. 326, pp. 909-938, 2009.

[45] M. N. Helfrick, C. Niezrecki, P. Avitabile and T. Schmidt, "3D digital image correlation methods for full-field vibration measurement," Mechanical Systems and Signal Processing, vol. 25, pp. 917-927, 2011.

[46] T. Siebert and M. J. Crompton, "Application of high speed digital image correlation for vibration mode shape analysis," in Application of Imaging Techniques to Mechanics of Materials and Structures, Volume 4, Anonymous Springer, 2013, pp. 291-298.

[47] T. Schmidt, J. Tyson and K. Galanulis, "Full-field dynamic displacement and strain measurement using advanced 3d image correlation photogrammetry: part 1," Exp Tech, vol. 27, pp. 47-50, 2003.

[48] Kirugulige MS, Tippur HV, Denney TS. Measurement of transient deformations using digital image correlation method and high-speed photography: application to dynamic fracture. Appl Opt 2007; 46 (22):5083–96.

[49] Warren C, Niezrecki C, Avitabile P, Pingle P. Comparison of FRF measurements and mod eshapes determined using optically image based, laser, and accelerometer measurements. Mech Syst Sig Process 2011; 25:2191–202.

[50] Wang W, Mottershead JE, Ihle A, Siebert T, Reinhard Schubach H. Finite element model updating from full-field vibration measurement using digital image correlation. J Sound Vib 2011; 330:1599–620.

[51] T. Schmidt, J. Tyson, and K. Galanulis, “Full-field dynamic displacement and strain measurement using advanced 3D image correlation photogrammetry: Part I,” Experim. Techn., vol. 27, no. 3, pp. 47–50, 2003.

[52] K. Chang, A. Nazare, and P. Ifju, “Flapping wing deformation measurement in hover flight conditions,” in Proc. Annu. Conf. Experim. Appl. Mech., vol. 3. 2016, pp. 143–149.

[53] E. Zappa, P. Mazzoleni, and A. Matinmanesh, “Uncertainty assessment of digital image correlation method in dynamic applications,” Opt. Lasers Eng., vol. 56, pp. 140–151, May 2014.

[54] A. Lavatelli and E. Zappa, “Displacement uncertainty model for 2-D DIC measurement under motion blur condition”, in IEEE Transactions on Instrumentation and Measurement, vol.66, no. 3, pp. 451-459, Mar. 2017.

[55] Pan B, Lu Z, Xie H. Mean intensity gradient: an effective global parameter for quality assessment of the speckle patterns used in digital image correlation. Opt Lasers Eng 2010; 48:469–77.

[56] Reu PL. Experimental and numerical methods for exact subpixel shifting. Exp Mech 2011; 51:443–52.

[57] Gonzalez RC, Woods RE. Digital image processing. 2nd ed. New York: Prentice-Hall Inc;2002.

[58] Briggs WL, Henson VE. The DFT: an owner’s manual for the discrete Fourier transform, society for industrial and applied mathematics, Philadelphia, 1995.

[59] Reu PL. Experimental and numerical methods for exact subpixel shifting. Exp Mech 2011; 51:443–52.

[60] T. Chan, B. Amizic, R. Molina, S. D. Babacan, T. Bishop, and A. Katsaggelos, “Blind image deconvolution,” in Blind Image Deconvolution, pp. 1–41–, CRC Press, May 2007.

[61] J. Stockham, T.G., T. Cannon, and R. Ingebretsen, “Blind deconvolution through digital signal processing,” Proceedings of the IEEE, vol. 63, no. 4, pp. 678–692, 1975.

[62] Z. Zhang, “A flexible new technique for camera calibration,” vol. 22, no. 11, pp. 1330–1334, 2000.

[63] H. Fortunato and M. Oliveira, “Fast high-quality non-blind deconvolution using sparse adaptive priors,” vol. 30, no. 6-8, pp. 661–671, 2014.

[64] M. Bertero, P. Boccacci, G. Desidera, and G. Vicidomini, “Image deblurring with Poisson data: from cells to galaxies,” Inverse Problems, vol. 25, no. 12, pp. 123006–, 2009.

[65] M. A. Sutton, T. L. Chae, J. L. Turner, and H. A. Bruck, “Development of a computer vision methodology for the analysis of surface deformations in magnified images,” in ASTM Special Technical Publication, no. 1094, pp. 109–132, 1991.

[66] P. Luo, Y. Chao, M. Sutton, and W. Peters III, “Accurate measurement of threedimensional deformations in deformable and rigid bodies using computer vision,” vol. 33, no. 2, pp. 123–132, 1993.

[67] P. Lava, W. Van Paepegem, S. Coppieters, I. De Baere, Y. Wang, and D. Debruyne, “Impact of lens distortions on strain measurements obtained with 2d digital image correlation,” vol. 51, no. 5, pp. 576–584, 2013.

[68] M. Grediac, “The use of full-field measurement methods in composite material characterization: Interest and limitations,” vol. 35, no. 7-8, pp. 751–761, 2004.

[69] P. Boccacci, Introduction to Inverse Problems in Imaging. CRC Press, 1998.

[70] W. ge Chen, N. Nandhakumar, and W. N. Martin, “Image motion estimation from motion smear-a new computational model,” Pattern Analysis and Machine Intelligence, IEEE Transactions on, vol. 18, no. 4, pp. 412–425, 1996.

[71] S. Wang, B. Guan, G. Wang, and Q. Li, “Measurement of sinusoidal vibration from motion blurred images,” Pattern Recognit. Lett., vol. 28, no. 9, pp. 1029–1040, 2007.

[72] B.-Q. Guan and S.-G. Wang, “Amplitude measurement of high frequency vibration from motion blur using moments,” Shanghai Jiaotong Daxue Xuebao/Journal of Shanghai Jiaotong University, vol. 41, no. 3, pp. 447–451, 2007.

[73] Lokhande R, Arya K V, Gupta P, Identification of parameters and restoration of motion blurred images, in Proceedings of the 2006 ACM symposium on Applied computing, 2006: 301-305.

[74] Yitzhaky Y, Kopeika N S, Identification of blur parameters from motion blurred images, Graphical models and image processing, 59(5): 310-320, 1997.

[75] R. Panerai, G. Tomassetti, S. Mariotti, N. D'Amico, C. Bortolotti, G. Grueff, A. Orfei, S. Montebugnoli, and A. R. Ambrosini, "Spectrum analysis and correlation", in Principles and Applications in Engineering, pp. 23–1–23–24–, CRC Press, July 2003.

[76] P. Stoica, Randolph, and Moses, Spectral Analysis of Signals. Pearson Prentice Hall, 2005.

[77] R. Gonzalez, R. Woods, and S. Eddins, Digital Image Processing Using MATLAB. Tata McGraw Hill Education, 2010.

[78] N. Wiener, Extrapolation, Interpolation, and Smoothing of Stationary Time Series, with Engineering Applications. Martino Publishing, 2013.

[79] B. P. Bogert, M. J. Healy, and J. W. Tukey, "The quefrency analysis for echoes: Cepstrum, Pseudp-Auotocovariance, Cross-cepstrum and Saphe Cracking", in Proceedings of Symposium on Time Series Analysis by Rosenblatt, 1963, pp. 209-243.

[80] A. V. Oppenheim, R. W. Schafer, T. G. Stockham, "Nonlinear filtering of Multiplied and Convolved Signals", IEEE Trans. Audio & Electroacoustics, Vol- AU-16, No.3, Sept.1968.

[81] D. G. Childers, D.P. Skinner, R. C. Kemerait, "The Cepstrum: A Guide to Processing", IEEE Proc. Vol. 65, No.10, Oct.1977, pp.1428-1443.

[82] P. O. Fjell, "Use of the cepstrum method for arrival times extraction of overlapping signals due to multipath conditions in shallow water", J. Acoust. Soc. Amer., Vol.59, no. 1, pp. 209-211, Jan. 1976.

[83] T. J. Ulrych, "Application of Homomorphic Deconvolution to Seismology", Geophys., Vol.36, No.4, pp. 650-660. Aug. 1971.

[84] A. V. Oppenheim, "Speech Analysis-Synthesis System Based on Homomorphic Filtering", J.A.S.A. Vol.45, pp. 458-465, 1969.

[85] J. E. Luck, "Automatic Speaker Verification using Cepstral measurements". J.A.S.A. Vol.46, pp. 1026-1032, 1969.

[86] R. B. Randall, "Cepstrum Analysis and Gearbox Fault Diagnosis". B & K Application note, No. 233-80.

[87] William K. Pratt. Digital Image Processing. John Wiley & Sons, Inc., 1978.

[88] R. Fabian and D. Malah. Robust identification of motion and out-of-docus blur parameters from blurred and noisy images. CVGIP, 53(5):403-412, September 1991.

[89] David G. Lamb. Passive monocular range imaging with a multiple aperture camera. Master's thesis, Department of Electrical Engineering, McGill University, Montreal, August 1994.

[90] M. Cannon, "Blind Deconvolution of Spatially Invariant Image Blurs with Phase", IEEE Trans. 90Acoustics, Speech and Signal Processing, vol. 24, pp.58-63, 1976.

[91] Shamik Tiwari, V. P. Shulka, and A.K. Singh, "Review of Motion Blur Estimation Techniques", Journal of Image and Graphics, Vol. 1, No. 4, Dec. 2013.

[92] LI Ying-jie, DI Xiao-guang, “Image Mixed Blur Classification and Parameter Identification based on Cepstrum Peak Detection”, Proceedings of the 35th Chinese Control Conference, July 27-29,2.

[93] Shiqian Wu, Zhongkang Lu, Ee Ping Ong, Weisi Lin, “Blind Image Blur Identification in Cepstrum Domain”, ICCCN 2007: 1166-1171.

[94] Xiumei Kang, Qingjin Peng, Gabriel Thomas and Yu, “Blind Image Restoration Using the Cepstrum Method” IEEE CCECE/CCGEI, Ottawa, May 2006.

[95] E. Zappa, A. Matinmanesh, and P. Mazzoleni, “Evaluation and improvement of digital image correlation uncertainty in dynamic conditions,” vol. 59, pp. 82–92, 2014.

[96] S. of Experimental Mechanics, “Dic challenge” Website. http://sem.org/dic-challenge/.

[97] R. Balcaen, P. Reu, P. Lava, and D. Debruyne, “Stereo-dic uncertainty quantification based on simulated images,” Exp. Mech., vol. 57, pp. 939–951, Jul 2017.

[98] N. Wiener, Extrapolation, interpolation and smoothing of stationary time series. The MIT Press, 1st m.i.t. paperback ed. ed., 1964.

[99] J. Nakamura, Image Sensors and Signal Processing for Digital Still Cameras. CRC Press, 2005.

[100] M. Grediac and F. Sur, “50th anniversary article: Effect of sensor noise on the resolution and spatial resolution of displacement and strain maps estimated with the grid method,” Strain, vol. 50, no. 1, pp. 1–27, 2014.

[101] J. Blaber, B. Adair, and A. Antoniou, “Ncorr: Open source 2d digital image correlation matlab software”, Exp. Mech, vol.55, pp. 1105-1122, Jul 2015.

[102] L. Meirovitch, “Fundamentals of Vibrations”, McGraw-Hill, New York, 2001.

[103] D. Reagan, A. Sabato, and C. Niezrecki, “Feasibility of using digital image correlation for unmanned aerial vehicle structural health monitoring of bridges,” Structural Health Monitoring.

[104] T. Siebert, T. Becker, K. Spiltthof, I. Neumann, and R. Krupka, “Highspeed digital image correlation: Error estimations and applications,” Opt. Eng., vol. 46, no. 5, 2007.

[105] P. Olaszek, “Investigation of the dynamic characteristic of bridge structures using a computer vision method,” *Measurement*, vol. 25, no. 3, pp. 227–236, 1999.